In-flight Performance of the BLAST-TNG Balloon-borne Far-infrared Telescope and Development of a Reconfigurable Readout on the RFSoC Platform for Frequency Multiplexed Superconducting Detector Arrays

by

Adrian Sinclair

A Dissertation Presented in Partial Fulfillment
of the Requirement for the Degree
Doctor of Philosophy

Approved October 2021 by the
Graduate Supervisory Committee:

Philip Mauskopf, Chair
Sanchayeeta Borthakur
Christopher Groppi
Daniel Jacobs
Johannes Hubmayr

ARIZONA STATE UNIVERSITY

December 2021

ABSTRACT

The Balloon-borne Large Aperture Submillimeter Telescope - The Next Generation (BLAST-TNG) was designed to map the polarized emission from dust in star forming regions of our galaxy. The dust is thought to trace magnetic fields and thus inform us of the role that it plays in star formation. BLAST-TNG improves upon the previous generation of balloon-borne sub-mm polarimeters by increasing the number of detectors by over an order of magnitude. A novel detector technology which is naturally multiplexed, Kinetic Inductance Detectors have been developed as an elegant solution to the challenge of packing cryogenic focal plane arrays with detectors. To readout the multiplexed arrays, custom firmware and control software was developed for the ROACH2 FPGA based system. On January 6th 2020 the telescope was launched on a high-altitude balloon from Antarctica and flew for approximately 15 hours in the mid-stratosphere. During this time various calibration tasks occurred such as atmospheric skydips, the mapping of a sub-mm source, and the flashing of an internal calibration lamp. A mechanical failure shortened the flight so that only calibration scans were performed. In this dissertation I will present my analysis of the in-flight calibration data leading to measures of the overall telescope sensitivity and detector performance. The results of which prove kinetic inductance detectors as a viable candidate for future space based sub-mm telescopes.

In parallel the fields of digital communications and radar signal processing have spawned the development of the Radio Frequency System On a Chip (RFSoC). This product by Xilinx incorporates a fabric of reconfigurable logic, ARM microprocessors, and high speed digitizers all into one chip. The system specs provide an improvement in every category of size, weight, power, and bandwidth. This is naturally the desired platform for the next generation of far-infrared telescopes which are pushing the limits of detector counts. I present the development of one of the first frequency multiplexed

detector readouts on the RFSoC platform. Alternative firmware designs implemented on the RFSoC are also discussed. The firmware work presented will be used in part or in full for multiple current and upcoming far-infrared telescopes.

TABLE OF CONTENTS

Page

LIST OF TABLES vi

LIST OF FIGURES vii

CHAPTER

1 FAR-INFRARED POLARIMETRY 1

1.1 Why Is Star Formation So Inefficient? 1

1.2 How to Measure Magnetic Fields in Molecular Clouds? 1

1.2.1 Radiative Alignment Torques 3

1.3 Polarimetry 3

1.4 Observing the Sub-MM Sky 5

1.5 Instruments 5

1.5.1 BLAST-TNG 8

2 IN-FLIGHT PERFORMANCE OF BLAST-TNG 13

2.1 Flight Operation 13

2.2 Calibrators 14

2.3 Kinetic Inductance Detector Frequency Response 16

2.4 Frequency and Dissipation Quadrature 17

2.5 Temperature Sensitivity 18

2.6 Cal-Lamp 20

2.7 Thermal Source Responsivity 21

2.7.1 Power Radiated by a Thermal Source 21

2.7.2 Difference in Power 23

2.7.3 Uncertainty in Responsivity 23

2.8 Stratospheric Skydip 24

2.8.1 Atmospheric Model 25

CHAPTER Page

2.8.2 Skydip Responsivity Comparison 28
2.8.3 Ice Clouds 30
2.8.4 Wildfire Smoke 32
2.9 RCW92 34
2.9.1 NEFD from RCW92 37
2.9.2 Polarization of RCW92 38
2.10 Frequency Noise Stack-Up 39
2.11 Noise Equivalent Power 42
3 RECONFIGURABLE READOUT ON THE RFSOC PLATFORM 48
3.1 Current Design 53
3.1.1 Frequency Comb 53
3.1.2 Software and PYNQ 59
3.1.3 DSP Module Verification 59
3.2 Readout Noise Measurements 61
3.2.1 Loopback Noise 66
3.2.2 Measuring D/A Noise 67
3.3 Path Forward 69
3.4 CORDIC MFSK Implementation 70
3.4.1 FSK Modem 71
3.4.2 CORDIC Based Implementation 71
3.4.3 FSK Homodyne 75
4 READOUT LINK BUDGET 79
4.1 Noise Temperature 79
4.2 Quantization Noise 80

CHAPTER Page

4.2.1 Quantization Noise Simulation 83
4.3 Cascaded Noise 84
4.4 Coaxial Cable Attenuation 88
4.5 Cryogenic Link Budget 91
4.6 Noise Stack 94
REFERENCES 95
APPENDIX
A TIMING AND SYNCHRONIZATION FOR BLAST-TNG 101
B DIGITAL BALANCING OF AN ANALOG IQ MIXER 103
B.1 Phase Imbalance 103
B.2 Amplitude Imbalance 105
B.3 Corrective Waveform Generation 106

LIST OF TABLES

Table Page

2.1 Mean Responsivities and Associated Values for Each Array 22

2.2 Noise Equivalent Flux Density 38

2.3 Frequency Noise for the Three Arrays from In-Flight Detector Timestreams 43

3.1 SWAPC&B Comparison between the CASPER ROACH2 System and RFSoC ZCU111 Development Board. 51

3.2 BLAST-TNG Firmware FPGA Resource Utilization Compared to the Available Resources on the RFSoC FPGA 52

LIST OF FIGURES

Figure		Page
1.1	Stokes Parameters	4
1.2	Pillars of Creation with Inferred Magnetic Field Lines Superimposed	6
1.3	Atmospheric Transmission	7
1.4	Large Millimeter Telescope	8
1.5	The Stratospheric Observatory for Infrared Astronomy	9
1.6	Balloon-borne Large Aperture Submillimeter Telescope - The Next Generation	10
1.7	BLAST-TNG Gondola and Cold Optics	10
2.1	Launch of BLAST-TNG from LDB on January 6th 2020.	14
2.2	Sweep of 350 μm Array at Three Different Loading Conditions	15
2.3	Block Diagram of the BLAST-TNG Telescope	16
2.4	Equivalent circuit for a shunt impedance device Z along a transmission line of characteristic impedance Z_0. 2-port scattering parameters are referenced to port 1 and port 2 in the diagram.	17
2.5	Percent Fractional Frequency Shift per Millikelvin as a Function of Temperature	19
2.6	Median Δf of the Cal-Lamp Response under Three Different Background Loading Conditions	20
2.7	The Difference in Power for Two Different Temperature Thermal Sources Relative to the RJ Limit	24
2.8	Median Detector Timestream from the 350um Array for the Skydip Performed at Float	26
2.9	Histogram of Frequency Shifts for the Skydip for Each Array	26

Figure Page

2.10 H_2O Measured by the MLS Instrument for Various Altitudes at Locations Nearly above McMurdo on January 6th 2020. 27
2.11 Simulated Skydip with the AM Software 28
2.12 The Ratio of the Skydip Responsivity to the Thermal Source Responsivity for Each Array 29
2.13 Star Camera Snapshots during the Skydip 30
2.14 AIM-CIPS PMC Albedo Measurement of the Southern Hemisphere for Jan 6th 2020 31
2.15 Simulated Skydip with AM Software with PMCs 32
2.16 Simulated Skydip with AM Software with Cirrus Clouds 33
2.17 Herschel SPIRE Instrument 350um Map of Home and RCW92 35
2.18 Cross Section of Herschel Maps across RCW92 Overlayed with BLAST-TNG Single Detector Timestreams 36
2.19 Signal to Noise Histograms on RCW92 37
2.20 RCW92 Scans from Orthogonal Polarizations after Flat Fielding 39
2.21 Noise Power Spectrum in the Frequency Quadrature $\sqrt{S_{xx}}$ and Dissipation Quadrature $\sqrt{S_{yy}}$ 44
2.22 Histogram of Noise Quadrature Difference for the 250um-V Array 45
2.23 Optical NEP of BLAST-TNG 46
2.24 Detector NEP of BLAST-TNG 47
3.1 The ROACH2 Motel and Xilinx RFSoC ZCU111 Development Board . . 50
3.2 Block Diagram of the BLAST-TNG to RFSoC Design 53
3.3 The Vivado 2018.3 Block Design of the BLAST Equivalent System. 54

Figure Page

3.4 Graphic to Show the sinx/x D/A Response and Nyquist Zones and Aliased Waveforms . . . 57
3.5 D/A Transfer Function Measurement . . . 58
3.6 BLAST DSP Module in Simulink . . . 58
3.7 Jupyter Notebook Initialization of Firmware and Clocks . . . 59
3.8 Jupyter Notebook Displaying Data Capture and Plotting . . . 60
3.9 Snapshot of Data Captured within the Firmware after the ADCs . . . 62
3.10 Loop Back Measurements Directly from the ADC with a 1000 Tone Comb . . . 63
3.11 Polyphase Filterbank Spectra Capture for a Single Tone in Loopback . . 64
3.12 Magnitude of the Downconverted and Accumulated Values for a 1000 Tone Comb . . . 64
3.13 Phase Noise for a Single Channel as a Function of the Number of Tones 67
3.14 Phase Noise with the RFSoC for 1000 Channels . . . 68
3.15 Microwave Interferometer Setup for Measuring the D/A Quantization Noise Floor . . . 69
3.16 An Example MFSK Modem Design . . . 72
3.17 CORDIC MFSK Block Design . . . 75
3.18 FSK Waveform Capture with Jupyter Notebook . . . 76
3.19 FSK Homodyne Setup Showing the Path from the D/A to the A/D . . . 77
3.20 Oscilloscope and Spectrum Analyzer Measurements of the FSK Homodyne System . . . 78
4.1 Equivalent Noise Temperature Model of an Amplifier . . . 80
4.2 Quantization Error $e(t)$ as a Function of Time for a Voltage Step $q(\Delta V)$ 81

Figure Page

4.3 A Discrete Sine Wave $x(n)$ of Amplitude 3 Along with a 3 Bit Quantized Version $x_q(n)$ in Units Normalized to the Quantization Step ΔV(or q) 84
4.4 The Quantization Error 85
4.5 Simulated Quantization Noise Power Spectral Density 86
4.6 Equivalent Model for the Noise Factor of a Component 86
4.7 Example Cascaded Noise Chain of Three Components 87
4.8 Example Cascaded Noise Temperature of Three Components 88
4.9 Cross Section of a Coaxial Cable 89
4.10 Stainless Steel Resistivity and the Lorenz Ratio 90
4.11 Coaxial Cable Loss per Meter as a Function of Frequency and Temperature 91
4.12 BLAST-TNG Cryogenic RF Chain Model at a Center Frequency of 800MHz 93
4.13 Noise Power and Phase Noise vs Drive Attenuation 94
A.1 Timing Distribution Diagram for BLAST-TNG Readout Electronics and Flight Computers 102

Chapter 1

FAR-INFRARED POLARIMETRY

1.1 Why Is Star Formation So Inefficient?

Stars form from cold gas and dust which collapses gravitationally when the different outward pressures are exceeded. The pressures can be thermal, turbulent and magnetic. Each outward pressure can contribute to slowing the in fall and increasing the required initial cloud mass to form stars. This reduces the likelihood of star formation and thus reduces the star formation efficiency. Observations of molecular clouds with active star formation have shown a value around 0.01 SFR per free fall time, Krumholz and Tan (2007). When star formation is simulated and only gravity is included the rates are orders of magnitude higher. It has been suggested that other processes such as turbulence, magnetic fields, and feedback/shocks are necessary to lower the rate. Simulations including these effects have confirmed that the SFR comes closer to matching observations, Krumholz and Tan (2007). More recent simulations of magnetically supercritical molecular clouds suggest that they actually play a minor role in directly setting the SFR but instead may be important in directing feedback flows and supernovae to reduce the SFR, Krumholz and Federrath (2019). Confirming this finding with observation requires mapping the magnetic field morphology at multiple scales and an accounting of the feedback processes present.

1.2 How to Measure Magnetic Fields in Molecular Clouds?

Molecular clouds are extremely cold collections of dust and gas. The emission of which peaks in the far-infrared and is thus extremely difficult to observe at other

wavelengths. An example of this is that these regions are typically characterized by a reduction in optical light which is parameterized by an extinction coefficient. Thus to measure the properties of the cloud itself we must observe in the far-infrared. There are three main ways to measure the properties of the magnetic fields from this radiation, Zeeman splitting, Faraday rotation, and polarization.

The Zeeman effect is the hyperfine transition level splitting in the presence of a magnetic field. This can be predicted with quantum theory and compared with the observed spectral shifts to extract the external magnetic field strength. This was used to infer that sunspots are related to magnetic fields on the surface of the sun by the astronomer George E. Hale as early as 1908. Observations of Zeeman splitting continue today with coherent receivers on radio telescopes such as the VLA and ALMA which observe the emission from the molecular species, HI, OH, CN, CH_3OH, and H_2O, Crutcher and Kemball (2019). This provides the most direct method of measurement of magnetic field strength.

Faraday rotation is another method of determining the magnetic field strength. First discovered by Michael Faraday in 1845 the angle of polarization of light may be rotated when traveling through a medium in the presence of a magnetic field. Specifically the polarization angle can be related to the magnetic field strength as,

$$\Delta\theta \propto NB\lambda^2 \tag{1.1}$$

Where $\Delta\theta$ is the change in polarization angle in radians, N is the electron density in m^{-3}, B is the magnetic field strength in T, and λ is the wavelength of observation. Thus a multi-band polarimeter could potentially detect the rotation of polarization angle. The method breaks down when the effect is strong enough to cause a full 180 degree angle rotation.

If the dust or smoke particles are not spherically symmetric then the light they

emit may be polarized. When the dust grains are randomly oriented the emission from a dust cloud may have no polarization. This may change when in the presence of a magnetic field whereby the grains align with its long axis perpendicular to the orientation of the magnetic field. If we observe the polarized emission from cold dust in molecular clouds we can infer the orientation of the magnetic field. This has been thought to come from paramagnetic grains until recently another theory, radiative alignment torques, has produced better matches to observations. This is the main method for mapping magnetic fields for which BLAST-TNG was designed.

1.2.1 Radiative Alignment Torques

A leading theory on the orientation of dust grains in magnetic fields was first proposed by Dolginov and Mitrofanov (1976), and more recently by Lazarian and Hoang (2019). The idea is that photon pressure and the radiative torques they produce help to align grains in the presence of magnetic fields. If a grains' shape is irregular then there may be a differential extinction cross section for different polarized light. For instance right and left circularly polarized light would apply different pressures and thus a net toque would occur. If this grain is in a magnetic field and is paramagnetic then it can precess around the magnetic field direction and become spun up by the radiation. This has been checked against simulations by Draine and Weingartner (1997), in which they have shown this as viable method for grain alignment. Recent observational tests in the FIR by Santos *et al.* (2019) have also given credence to the theory.

1.3 Polarimetry

To learn about the the magnetic field and dust properties we need to be able to measure the polarization state of the radiation field. A convenient set of values called

the Stokes parameters are used for this. These are I the total intensity, two linearly polarized intensity values Q and its 45 degree version U, and a circularly polarized intensity V. These can be related to the electric field as,

$$\begin{aligned} I &= \langle E_i^2 \rangle + \langle E_j^2 \rangle \\ Q &= \langle E_x^2 \rangle - \langle E_y^2 \rangle \\ U &= \langle E_a^2 \rangle - \langle E_b^2 \rangle \\ V &= \langle E_r^2 \rangle - \langle E_l^2 \rangle \end{aligned} \tag{1.2}$$

where the subscripts give the direction of the electric field vectors, where a and b are 45 degrees from x and y respectively, r and l refer to right-handed or left-handed polarization in polar coordinates. For reference see Figure 1.1 to visualize the Stokes parameters.

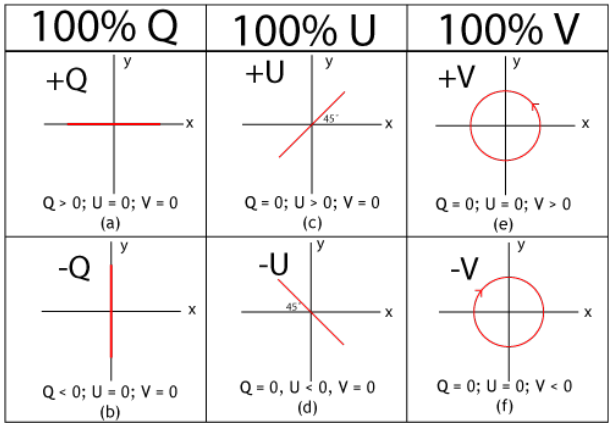

Figure 1.1: Stokes parameters, figure from Wikipedia

To relate the measured Stokes parameters to predictions it is useful to calculate the polarization fraction defined as,

$$p = \sqrt{Q^2 + U^2}/I. \tag{1.3}$$

Another useful metric is to find the polarization angle given by the following equation,

$$\psi = \frac{1}{2}\arctan(U/Q). \tag{1.4}$$

Given the variation of the polarization angle we can also estimate the magnetic field strength. For example the Chandrasekhar-Fermi method, relates the line of sight velocity dispersion and perpendicular polarization dispersion to magnetic field strength,

$$B_{\perp} = \sqrt{4\pi\rho}\frac{\Delta V}{\Delta\psi}, \tag{1.5}$$

Where ρ is the volumetric density, ΔV is the line of sight velocity dispersion, and $\Delta\psi$ is the polarization angle dispersion.

These equations were used to find the orientation and degree of polarization in the pillars of creation shown in Figure 1.2. This has allowed the authors to conclude that the pillar structure is mainly held up by magnetic support and suggest rapid star formation due to shocks with frozen in magnetic fields.

1.4 Observing the Sub-MM Sky

The atmosphere near the surface of the Earth contains a significant amount of water vapor. The triatomic molecule for water has rotational energy states which emit in the millimeter and submillimeter. These rotational lines are easily excited thermally and are primarily responsible for the opacity of the atmosphere in these bands. There are other contributors to the total opacity but water vapor is by far the greatest.

1.5 Instruments

The atmosphere has caused scientists to seek out the highest and driest places on Earth for sub-mm telescopes. Dormant volcanoes are a favorite choice, the James

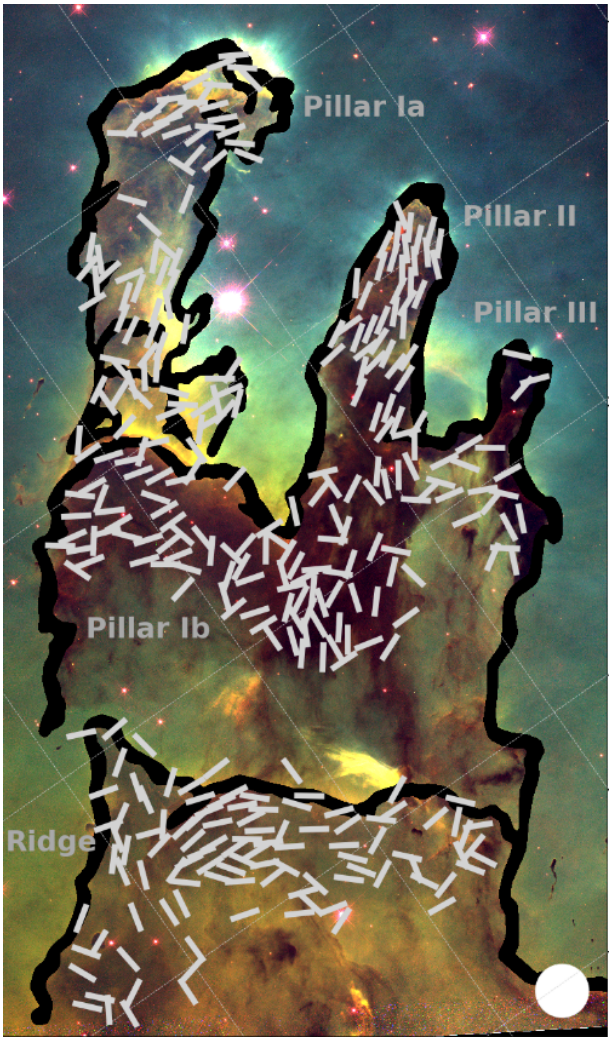

Figure 1.2: Pillars of creation with inferred magnetic field lines superimposed as grey rectangles, figure from Pattle *et al.* (2018)

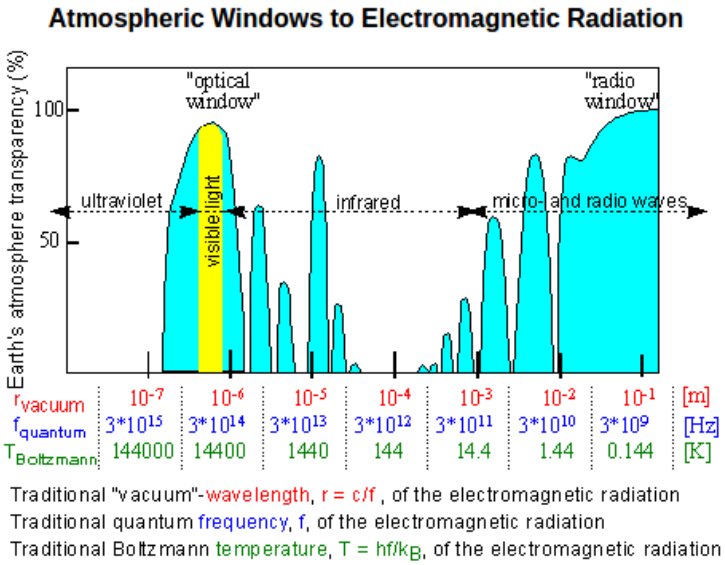

Figure 1.3: Atmospheric transmission at different wavelengths/frequencies

Clerk Maxwell Telescope on Mauna Kea in Hawaii, and the Large Millimeter Telescope on the Sierra Negra mountain (Tliltpetl Figure 1.4). These ground based telescopes still take a hefty penalty from atmospheric absorption so some groups take to the skies. The Stratospheric Observatory for Infrared Astronomy (SOFIA Figure 1.5) is an airborne observatory capable of flights in either hemisphere while cruising at an altitude of 41,000 feet. This allows for observations above most of the atmospheres water vapor but for some science cases this is still too much atmospheric loading and absorption. High altitude ballooning is the next cheapest option where you can lift a 5000 pound telescope into the stratosphere to altitudes around 120,000 feet. This is above 99% of the Earths atmosphere. The Balloon-borne Large Aperture Submillimeter Telescope shown in Figure 1.6 is an example of this type of telescope and is discussed further in the following subsection.

Figure 1.4: Large Millimeter Telescope (LMT) a top the sierra negra mountain (Tliltpetl)

1.5.1 BLAST-TNG

The Balloon-borne Large Aperture Submillimeter Telescope (BLAST) which flew three times, was initially designed to make confusion limited maps of distant galaxies in three bands: 250, 350, and 500 μm. Analysis of the flight data provided evidence that over half of the far-infrared background light comes from galaxies at redshifts greater than 1.2, Devlin *et al.* (2009). Although the BLAST gondola was destroyed after the second flight, the receiver was recovered and upgraded for polarization sensitivity. This became BLASTPol, with added polarization the investigations of magnetic fields in star forming region became a main focus. BLASTPol flew twice and produced multi-band polarization maps of the Vela C giant molecular cloud allowing for empirical investigations of the relations between the polarization fraction and

Figure 1.5: The Stratospheric Observatory for Infrared Astronomy (SOFIA) - image wikipedia

column density, Fissel *et al.* (2016).

Following the successful flights and scientific return of the previous experiments the BLAST collaboration devised the ambitious next generation balloon-borne polarimeter (BLAST-TNG). Relying heavily on the legacy work the system was scaled up in multiple ways, physically by increasing the primary mirror from 2 to 2.5 meters, in polarized pixel count from 270 to 1593, and increasing the cryogenic hold time to greater than 30 days. The telescope is a Cassegrain design with cold optics setup in an Offner-relay configuration. Shown on the right of Figure 1.7 is the cold optics with each component labeled. The left side of the figure shows some of the main components and pointing subsystems.

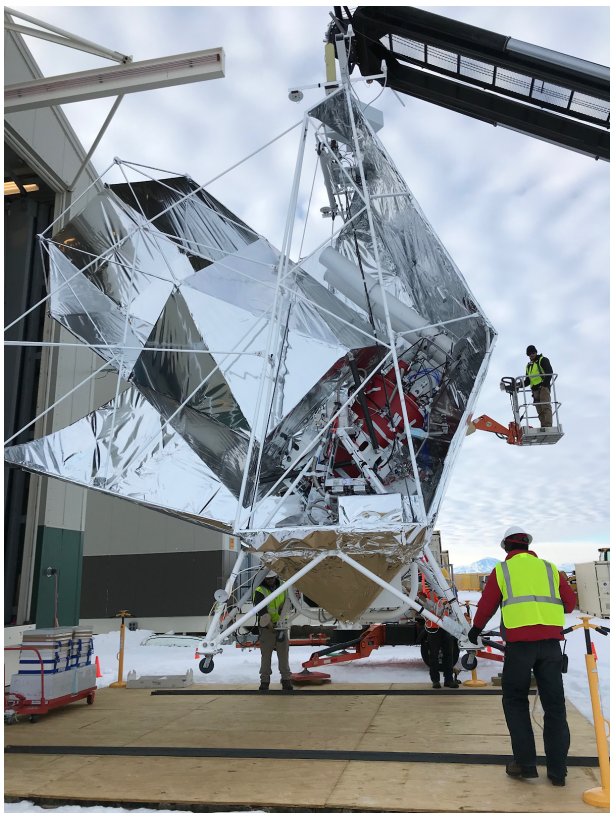

Figure 1.6: Balloon-borne Large Aperture Submillimeter Telescope - The Next Generation (BLAST-TNG)

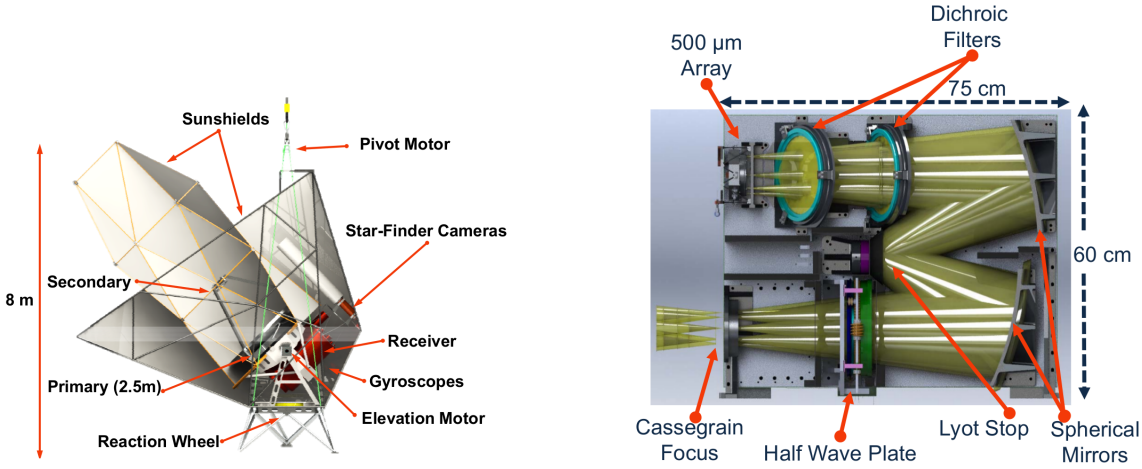

Figure 1.7: On the left is the BLAST-TNG gondola with some of the major components labeled. The right shows the cold optics design within the cryostat.

The detector technology has also been upgraded from the Silicon-Nitride cooled bolometers to superconducting kinetic inductance detectors (KIDs). Building on the work beginning at JPL/Caltech, Day *et al.* (2003), researchers at Cardiff developed a lumped element design, Doyle *et al.* (2007). Polarization sensitivity was then developed in a lumped element design, Hubmayr *et al.* (2014). The BLAST-TNG detectors were developed by the quantum sensors group at NIST Boulder and leveraged the prior work and brought custom developments such as high coupling efficiency and photon noise limited performance for a custom Tri-layer of TiN/Ti/TiN, Hubmayr *et al.* (2015).

This detector technology required the development of a custom FPGA based readout system and RF electronics. Starting from an open-source design provided by UCSB, McHugh *et al.* (2012), the system was upgraded to the next generation FPGA based platform and modified for linear mode detection as opposed to pulse detection. The system is well described in the paper, Gordon *et al.* (2016), and thesis, Gordon (2019). The firmware and software developed in various forms were developed open-source and were provided to multiple projects, OLIMPO, Superspec, TolTEC, MUSCAT, and others.

When first proposed BLAST-TNG was going to be the first balloon-borne demonstration of the KIDs technology, the experiment OLIMPO flew them first in the summer of 2018, Paiella *et al.* (2020), beating BLAST-TNG by a year, but flying the readout electronics and firmware developed for BLAST-TNG. During the summer of 2018 the BLAST-TNG team was in Palestine, Texas at the Columbia Scientific Ballooning Facility (CSBF) performing integration and flight compatibility. The experiment was designed for an Antarctic flight launching from the Long Duration Balloon (LDB) on the Ross ice shelf near McMurdo station. The first Antarctic campaign of 2018-2019 saw no flight due to unfit weather and high winds. The second season 2019-2020, we

successfully launched on January 6th 2020. The flight suffered a mechanical failure after $\sim$15 hours and was terminated roughly 200 miles from McMurdo. The instrument was recovered piece by piece after many trips via airplane and helicopter. The calibration tasks performed during the shortened flight were saved to hard drives and the in-flight performance of BLAST-TNG was extracted from this data and is the topic of chapter 2.

Chapter 2

IN-FLIGHT PERFORMANCE OF BLAST-TNG

2.1 Flight Operation

The BLAST-TNG payload was launched from the long duration balloon facility on the Ross Ice Shelf at approximately 6pm NZDT on January 6th 2020. The system was controlled from various radio links provided by CSBF. On ascent through the tropopause the readout systems were kept powered and periodically tuned to keep on resonance. Once the gondola was stabilized and verified to be pointing anti-sun the shutter was dropped. This changed the load on the detectors drastically enough that a new frequency comb was required. It was observed in the initial sweeps that most resonances had shifted to higher frequencies which is indicative of the reduced loading. The dark detectors however showed a decrease in resonant frequency which implied that the array temperatures were slightly higher at float. Once it was deemed safe to release the inner frame of the gondola freeing the elevation drive another set of sweeps were taken. We then began the calibration tasks, the first of which was to perform a 10 degree skydip with multiple nods lasting approximately 7 minutes. In order to focus the secondary mirror and find the offset of the sub-mm beam from the star cameras we planned to map a bright point source at RA $15^h13^m46^s$ and Dec. $-56°24'54"$ in J2000. A bright source was found to achieve focus but was instead $\sim 1/4°$ away from our object of choice. A raster scan was performed on this object post-focusing from which we estimate the point source sensitivity. Following this we slewed to a new location and performed a raster scan on a patch thought to contain Mars. During the long scan we suffered a mechanical failure which prevented pointing

Figure 2.1: Launch of BLAST-TNG from LDB on January 6th 2020.

control. After this the team decided to terminate the flight and the telescope landed just over the Royal society ranges roughly 200 miles from McMurdo.

2.2 Calibrators

To reduce uncertainty multiple calibrators were used to estimate the response, efficiency, and sensitivity. The calibrators employed are ground based thermal loads, atmospheric models, electrothermal detector models, and Herschel space telescope maps. In addition to these calibrators an inverse bolometer, which when calibrated

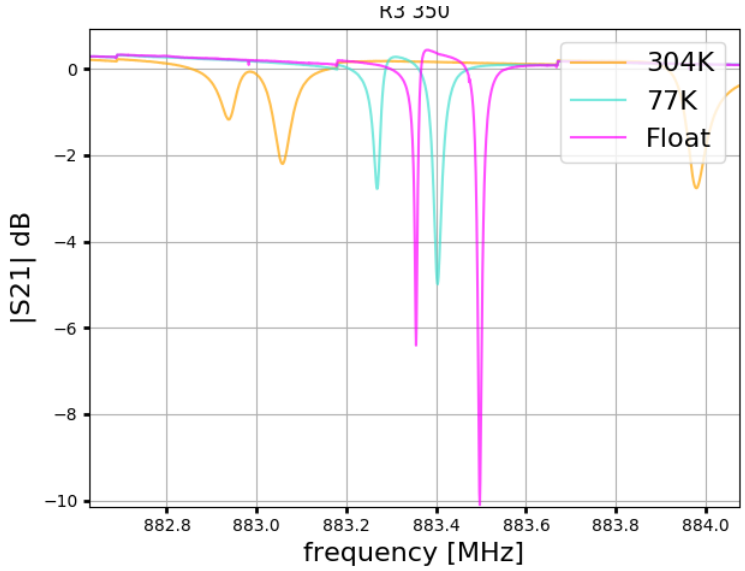

Figure 2.2: Section of sweep of 350 μm array at three different loading conditions, 304K, 77K, and float.

using another reference may be used to separate the various contributions from the elements in the optical chain.

A stack of optical elements sits in between the detectors and the astronomical source to be observed. This stack consists of the primary mirror, secondary mirror, cold optical components such as infrared blockers and dichroic filters, and an aluminum horn block. Each elements physical temperature and transmission/reflectivity contribute to the optical loading and telescope responsivity. To investigate the individual contributions we model the stack of elements as a multi-port cascaded microwave network (figure 2.3).

First we discuss how to calculate the shift in frequency from the detector timestreams and sweeps. We then discuss the temperature sensitivity of the arrays and compare them to predictions. The cal-lamp and three primary calibrators are then discussed.

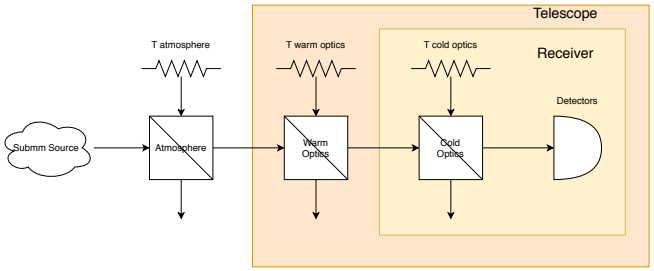

Figure 2.3: Simplified block diagram of the BLAST-TNG telescope and main components for evaluating responsivity and sensitivity. These sections are the cold optics, warm optics, and atmosphere. Each section can be modeled as a four port network with loss and an equivalent thermal noise added.

2.3 Kinetic Inductance Detector Frequency Response

For a series resonator consisting of a resistor, an inductor, and capacitor total impedance can be written as,

$$Z = R + j\omega L - j\frac{1}{\omega C}. \tag{2.1}$$

Using the reactance equations for a capacitor and inductor respectively,

$$X_C = \frac{1}{j\omega C}, \quad X_L = j\omega L. \tag{2.2}$$

If we assume small frequency deviations from the resonant frequency we can then simplify the total impedance to,

$$Z \approx R + j\sqrt{\frac{L}{C}}\delta x, \tag{2.3}$$

where $\delta x \approx (\omega - \omega_0)/\omega_0$ and $\omega_0 = 1/\sqrt{LC}$. We can then calculate the transfer function using the derived impedance Z assuming the microwave readout circuit is of the type presented in figure 2.4,

$$S_{21} = \frac{V_2^-}{V_1^+} = \frac{Z}{Z + Z_0} \tag{2.4}$$

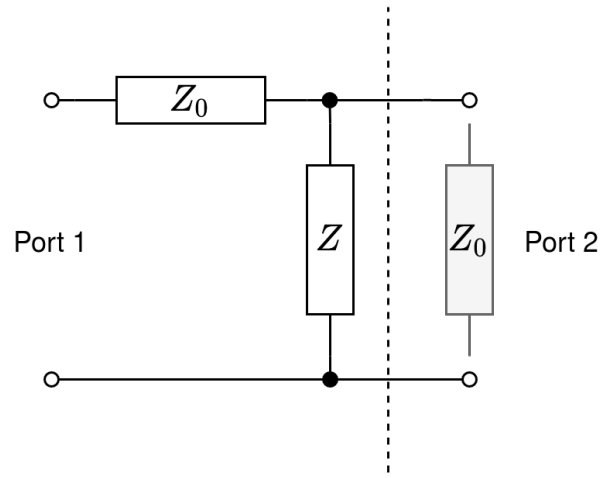

Figure 2.4: Equivalent circuit for a shunt impedance device Z along a transmission line of characteristic impedance Z_0. 2-port scattering parameters are referenced to port 1 and port 2 in the diagram.

$$S_{21} = \frac{R + j\sqrt{\frac{L}{C}}\delta x}{R + j\sqrt{\frac{L}{C}}\delta x + Z_0} \tag{2.5}$$

The above equation is usually simplified by using the following quality factor relations, the coupling $Q_c = 2\omega_0 L/Z_0$, the internal $Q_i = \omega_0 L/R$, and total $Q_r = Q_i Q_c/(Q_i+Q_c)$. Leaving the following more familiar form,

$$S_{21}(\omega) = 1 - \frac{Q_r}{Q_c}\Big(1 + j2Q_r\delta x\Big)^{-1}. \tag{2.6}$$

2.4 Frequency and Dissipation Quadrature

In typical operation we want to determine the frequency shift of a detector from some nominal frequency. To determine this shift we use the time series of the in-phase (I) and quadrature (Q) components of each probe tone along with the complex transmission curve of each resonator. The following two equations provide the frequency

shift in the frequency direction Δf_x and dissipation direction Δf_y,

$$\Delta f_x = \frac{I(t)\left(\frac{d}{df}\Re(S_{21}(f))|_{f_0}\right) + Q(t)\left(\frac{d}{df}\Im(S_{21}(f))|_{f_0}\right)}{\left(\frac{d}{df}\Re(S_{21}(f))|_{f_0}\right)^2 + \left(\frac{d}{df}\Im(S_{21}(f))|_{f_0}\right)^2}, \tag{2.7}$$

Where $S_{21}(f)$ is the complex two port transmission, f_0 is the resonant frequency

$$\Delta f_y = \frac{Q(t)\left(\frac{d}{df}\Re(S_{21}(f))|_{f_0}\right) - I(t)\left(\frac{d}{df}\Im(S_{21}(f))|_{f_0}\right)}{\left(\frac{d}{df}\Re(S_{21}(f))|_{f_0}\right)^2 + \left(\frac{d}{df}\Im(S_{21}(f))|_{f_0}\right)^2} \tag{2.8}$$

This method or a similar approach has been used by NIKA, Catalano *et al.* (2014), and has been described in Barry (2014) and Gordon (2019). The Δf_x should be the quadrature modulated by the sky signal and thus is used in each of the calibrator measurements. The dissipation direction quadrature is used to help discriminate the different kinds of noise and is described in section 2.10.

2.5 Temperature Sensitivity

The temperature sensitivity of a superconducting resonator can be modeled from Mattis-Bardeen theory following Mauskopf (2018),

$$\frac{df_0}{dT} = \frac{\alpha f_0 e^{-\Delta_0/kT}}{T}\sqrt{\frac{2\pi kT}{\Delta_0}}\left(\frac{1}{2} + \frac{\Delta_0}{kT}\right)\left(1 + \sqrt{\frac{2\Delta_0}{\pi kT}}e^{-\xi}I_0(\xi)\right), \tag{2.9}$$

Where α is the kinetic inductance fraction, $\xi = hf_0/kT$, and Δ_0 is the superconducting bandgap under the approximation that $T << T_c$,

$$\Delta_0 = 1.76kT_c. \tag{2.10}$$

Naively applying equation 2.9 underestimates the frequency shift due to a change in temperature for TiN films. There have been many studies of this effect for TiN and others films which are considered to be disordered superconductors, see Gao *et al.* (2012) and Bueno *et al.* (2014). The effect of which is to broaden the band gap and spread the density of states such that it can be approximated with equation

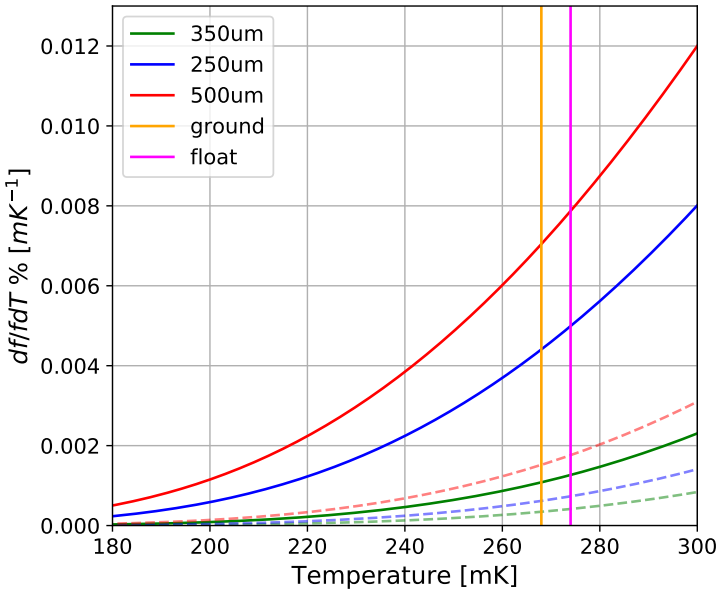

Figure 2.5: Percent fractional frequency shift per millikelvin as a function of temperature plotted for the three different bands 500, 350, and 250 μm in red, green, and blue. The dashed curves represent an application of MB theory with measured T_c values. The solid curves are using a lower T_c for each array that matches the observed frequency shift in the dark detectors for a 6mK temperature change. Orange and magenta vertical lines represent the array temperatures on the ground and at float altitude.

2.9 for a lower than measured critical temperature. Cryogenic temperature sensors mounted on the focal plane arrays measured a temperature increase from the ground at 268mK to float 274mK. The dark detectors from each focal plane had shifted down in frequency confirming the slightly higher temperature at float and providing an estimate of $\Delta f/\Delta T$. The dark fractional frequency shifts were found to be $0.027\%, 0.007\%, 0.046\%$ for the 250, 350, and 500 μm respectively. Fitting a Tc that is approximately 80% of the measured produces the observed shifts.

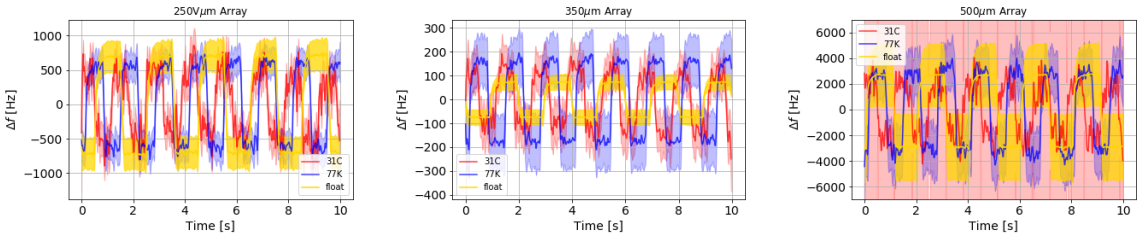

(a) 250um array V (b) 350um array (c) 500um array

Figure 2.6: Median Δf of the cal-lamp response under three different background loading conditions, 300K and 77K beam filling sources and the background at float. The standard deviation of the response for each detector is presented as semi-transparent bounds around the median channel response. This shows that detector responsivity did not change appreciably between measurements on the ground and at float for the three arrays. The 500um array standard deviation bounds for the 300K background suffered from large outliers.

2.6 Cal-Lamp

An inverse bolometer situated at the center of the Lyot stop inside the cryostat is used as a calibration lamp (cal-lamp). The power emitted from the cal-lamp however must be calibrated relative to some external source and thus is not an independent calibrator. It can provide a measure of the change in responsivity under different loading conditions. This is shown in figure 2.6 for the three arrays in which the response to the cal-lamp under three different background loads are overlaid.

2.7 Thermal Source Responsivity

The LEKID detectors used for BLAST-TNG have a linear frequency responsivity we define as,

$$R = \frac{\Delta f}{\Delta P}. \tag{2.11}$$

Meaning that the shift in frequency is proportional to the change in power absorbed. The receiver is defined as the stack of optical elements from the detectors to the cryostat window excluding the primary and secondary mirrors. The receiver was placed on the ground outside of the gondola within the high bay for various detector tests. The first of which placed a beam filling hot plate of microwave absorbing tiles in front of the window. This source was estimated to be at a physical temperature of 304K. The second thermal source was a liquid Nitrogen dewar with a window approximately matched in size to the receiver window. This dewar had a large uncertainty in the known temperature but has been bounded by the temperature of the LN_2 of 77K and by the first cold infrared blocking filter temperature of $\sim$ 143K. We first derive the power emitted by a thermal source and discuss some important points. Then we calculate the uncertainty in emitted power of the source and thus responsivity and summarize the results in table 2.1.

2.7.1 Power Radiated by a Thermal Source

The spectral radiance of a thermal source follows the Planck law,

$$B(\nu, T) = \frac{2h\nu^3}{c^2} \frac{1}{e^{\frac{h\nu}{kT}} - 1}. \tag{2.12}$$

To calculate the power emitted within each optical band for a beam filling source we integrate the Planck law over frequency after multiplying by the diffraction limited beam size and optical frequency response.

$$dP = B(\nu, T) F(\nu) d\nu dA d\Omega \tag{2.13}$$

-	500um	250um-V	350um	250um-U	250um-W
Δf [kHz]	3462	951	387	928	795
P_H [pW]	720	1371	1007	1371	1371
P_C [pW]	235	408	317	408	408
ΔP [pW]	484	963	690	963	963
R [Hz/pW]	7149	989	560	964	826
R_{NIST} [Hz/pW]	86400	14076	4420	14076	14076
σ_R [Hz/pW]	1178	265	152	222	232

Table 2.1: Mean responsivities and associated values for each array. The temperature of the cold load was taken to be 108.5K with an uncertainty of 31.5K and the hot load 304K with an uncertainty of 2K.

$$P = \int_\nu \int_A \int_\Omega B(\nu, T) F(\nu) d\nu dA d\Omega. \tag{2.14}$$

Where A is the effective area of the primary, Ω is the beam solid angle, and $F(\nu)$ is the optical transmission function. For a single mode isotropic radiator the antenna theorem gives,

$$A\Omega = \lambda^2. \tag{2.15}$$

This gives the power emitted in a single spatial and polarization mode,

$$P = \int_\nu d\nu \frac{h\nu}{e^{\frac{h\nu}{kT}} - 1} F(\nu). \tag{2.16}$$

This equation can be evaluated directly or within the two limits: Wien and Rayleigh-Jeans. Starting with the Rayleigh-Jeans limit where $h\nu << kT$ we end up getting the following equation,

$$P = kT \int_\nu d\nu F(\nu) = kT\Delta\nu. \tag{2.17}$$

Where $\Delta\nu$ is assuming a rectangular bandwidth with perfect transmission, $F(\nu) = 1$. In the other limit where $h\nu >> kT$ we get the Wien approximation,

$$P = \int_{\nu} d\nu h\nu e^{-\frac{h\nu}{kT}} F(\nu). \tag{2.18}$$

2.7.2 Difference in Power

To find the responsivity of the detectors we find the difference in power between two different temperature sources. This method is convenient when working within the Rayleigh-Jeans limit and is often used to find the equivalent noise temperature of amplifiers via the Y-factor method. Figure 2.7 plots the difference in power for two different temperature sources normalized to the RJ limit,

$$\frac{\Delta P}{\Delta P_{RJ}} = \frac{P_H - P_C}{k\Delta\nu(T_H - T_C)}, \tag{2.19}$$

where $P_H - P_C$ in the numerator is calculated in the Wein limit, the Rayleigh-Jeans limit, and with the full Planck function. This ratio of power relative to RJ is plotted vs the factor $kT/h\nu$ which shows that in the high temperature or low frequency limit the RJ approx can be used when calculating the power difference. The full Planck function should be used when $kT/h\nu$ is anywhere near unity.

2.7.3 Uncertainty in Responsivity

Starting from equation 2.11 we know that we need to find the uncertainty in the power and frequency estimates. The uncertainty in the power is thought to be dominated by the uncertainty in the absolute temperature of the blackbody calibration sources. The error in the power is estimated as,

$$\sigma_P = \frac{\partial P}{\partial T}\sigma_T = \sigma_T \int d\nu \frac{e^{\frac{h\nu}{kT}}}{k}\Big(\frac{h\nu\eta_{occ}}{T}\Big)^2, \tag{2.20}$$

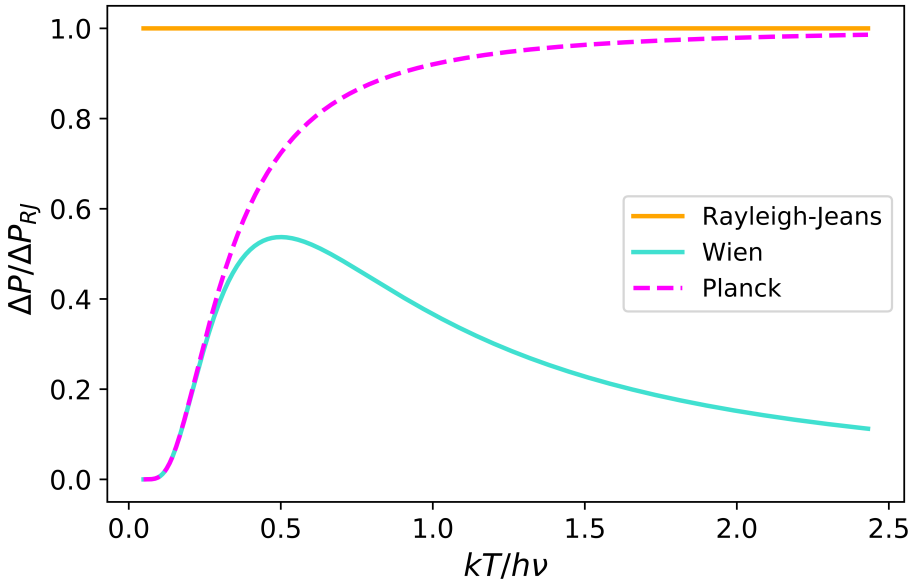

Figure 2.7: The difference in power for two different temperature thermal sources relative to the RJ limit of the difference in power vs the factor $kT/h\nu$. This shows that when this factor is near unity the Planck function must be used and not the RJ approximation.

where η_{occ} is the Bose-Einstein statistics energy state occupation number for photons. The total responsivity uncertainty is then,

$$\sigma_R = \sqrt{\left(\frac{\sigma_f}{\Delta P}\right)^2 + \left(\frac{\Delta f}{\Delta P^2}\right)^2 (\sigma^2_{P_H} + \sigma^2_{P_C})}. \tag{2.21}$$

2.8 Stratospheric Skydip

Atmospheric water vapor and to a lesser extent ozone have thermally excited rotational energy states which are the main contributors to the opacity of sky at sub-mm wavelengths. As early as the 1940s microwave radiometers were used to study the atmospheric water vapor through what are colloquially called skydips (Dicke *et al.* (1946)). The idea is that the integrated column density of water vapor depends

on the angle from zenith. Thus observing straight up a zenith angle of zero, will be looking through the least amount of atmosphere and observing parallel to the ground, a zenith of 90 degrees, would be looking through the greatest. Having well established models of the atmosphere informed by recent measurements of water vapor and ozone profiles could thus allow for the prediction of the angular dependent opacity. This would allow for the calibration of sub-mm telescopes via a simple skydip method in which the telescope nods through multiple angles from zenith and the response is compared to the atmospheric model.

A 10 degree skydip centered at 45 degrees from zenith was performed at an altitude of 36 km above the McMurdo Sound at 12:05 pm Jan 6th UTC. The nods up and down by five degrees lasted approximately 7 minutes. At this point in the flight the wind had blown the telescope over Ross Island and was above the McMurdo Sound at latitude -77.4 and longitude 165.3 with an absolute bearing (azimuth angle from true north to telescope pointing direction) of 84.9 degrees. This is approximately 20 degrees from the direction of Mt Erebus, which is Ross Islands largest active volcano.

Each detector timestream was converted to a frequency shift from it's value at 45 degrees. The skydip was seen with high signal to noise in each array, the median channel for each array is plotted in figure 2.9 along with a lower opacity trace that corresponds to the standard deviation of the entire array. It was discovered that there is more deviation in the trough of the triangular skydip pattern than the peak. This trough corresponds to the lower elevation angles (90-zenith) and therefore greater atmospheric path length.

2.8.1 Atmospheric Model

The software am, Paine (2019), is used to generate the atmospheric model. It splits the atmosphere into different layers based on pressure defined at the bottom of

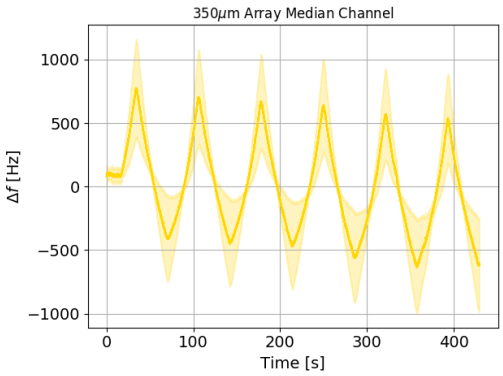

Figure 2.8: Median detector timestream from the 350um array for the skydip performed at float. The telescope was moved up and down by 5 degrees from a center elevation angle of 45 degrees.

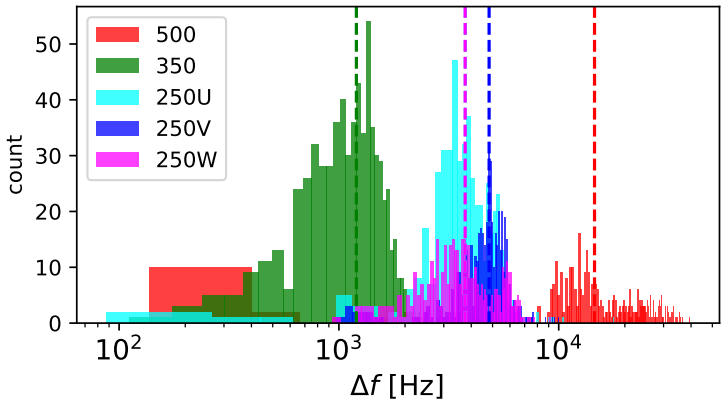

Figure 2.9: Histogram of frequency shifts for the skydip for each array, vertical dashed lines correspond to the median values.

the layer. Each layer is defined as a particular column type, at 35km and above, each column is of type dry air which contains typical ratios of molecular species. Water vapor (H_2O) and Ozone (O_3) are the main contributors to atmospheric opacity in the mm/sub-mm and are added explicitly by specifying a volume mixing ratio at each layer. The values for water vapor and Ozone are based on the NASA MERRA2

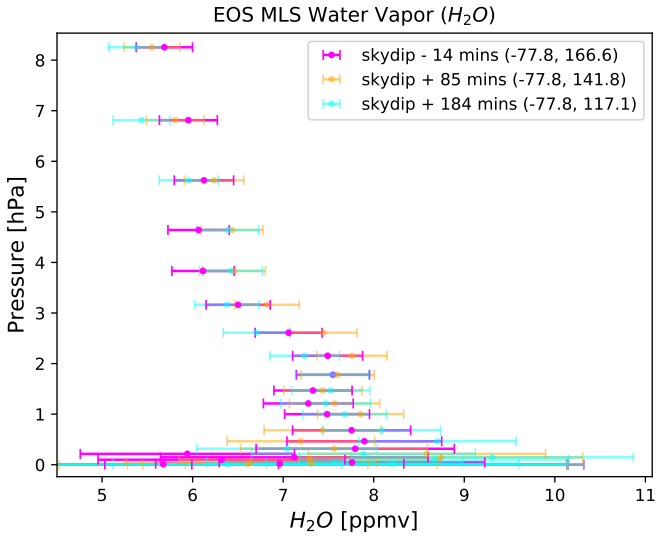

Figure 2.10: H_2O measured by the MLS instrument for various altitudes at locations nearly above McMurdo on January 6th 2020.

data set from 2016. While this data is a bit dated it is close to the measured values from the AURA satellites Microwave Limb Sounder (AURA-MLS) for the day of the skydip, Waters *et al.* (2006), Lambert *et al.* (2015). The MLS values for the water vapor around the this time and nearly above McMurdo are shown in figure 2.10. The values are extremely close to the default values found in the am configuration file for a balloon launched from McMurdo. The simulated skydip uses a secant of the angle from zenith to account for the differing path lengths. The simulated skydip is shown in Figure 2.11. For our skydip of 40-50 degrees the difference in power is computed as,

$$\Delta P_{RJ} = k(T_{40^\circ} - T_{50^\circ})\Delta\nu. \tag{2.22}$$

Using the simulation data from figure 2.11 we get powers of 1.4, 0.55, and 0.34 pW for the 250, 350, and 500um arrays.

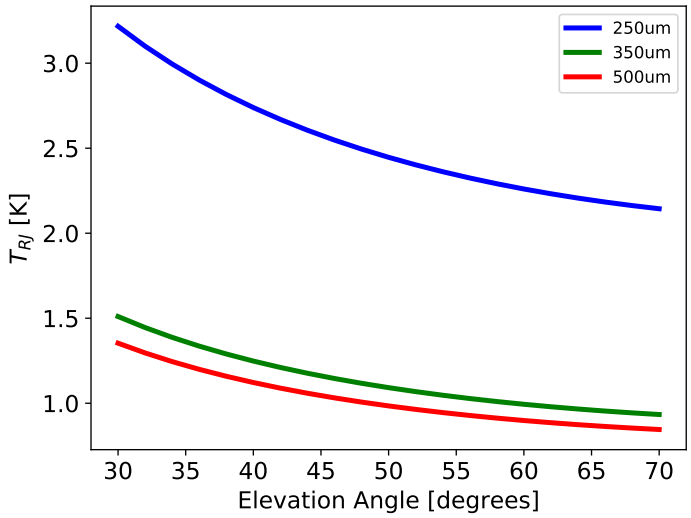

Figure 2.11: Simulated skydip with the am software for the 250, 350, and 500um arrays and a 30% bandwidth at an altitude of 35 km. The Rayleigh-Jeans brightness temperature for a single mode vs elevation angle (90 - zenith angle).

2.8.2 Skydip Responsivity Comparison

We can now calculate the responsivity of the telescope to the skydip as,

$$R_{skydip} = \frac{\Delta f}{\Delta P_{RJ}}, \tag{2.23}$$

Using the median frequency shifts for each array from figure 2.9. This responsivity can be compared to the measured responsivity to thermal sources to determine how well the calibrators agree. The ratio of the two shown in figure 2.12 gives roughly a factor of three for each array. The ratio of the two responsivities is,

$$\frac{R_{skydip}}{R_{thermal}} = \frac{\Delta f_{skydip}}{\Delta P_{skydip}} \frac{\Delta P_{thermal}}{\Delta f_{thermal}} \tag{2.24}$$

The error bars are calculated from the conservative (large error) thermal responsivity and the standard deviation in the skydip Δf. What could be causing this discrepancy?

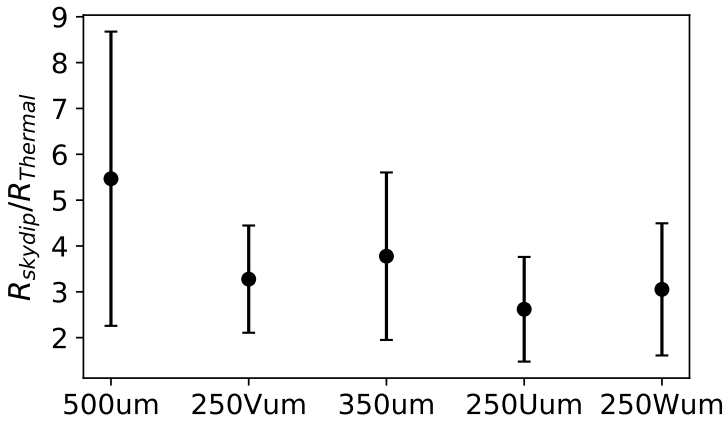

Figure 2.12: The ratio of the skydip responsivity to the thermal source responsivity for each array.

The first thing to question is if the responsivity of the detector arrays increased by a factor of three from ground to float. By checking the cal-lamp response from ground to float we see no appreciable increase in response as seen in figure 2.6, thus the detectors themselves are not responsible.

The next possibility is that the difference in power emitted by the thermal sources at the front of the receiver was a factor of three smaller. This would imply that the temperature difference between the hot and cold load was three times smaller, requiring the LN2 load to have a temperature above 220K which is unlikely. When placing a curved metallic plate over the window to reflect the emission of the receiver back on itself the resonant frequencies were higher than when looking at the LN2 load, meaning the loading with the plate is higher. Knowing the physical temperature of the first infrared blocking filter to be $\sim$ 140K the LN2 load must be lower than this. If the cold load is exactly 140K this only can explain a factor of 1.4.

Eliminating the detectors and thermal sources as candidates we can then turn to investigating the atmospheric model in more detail.

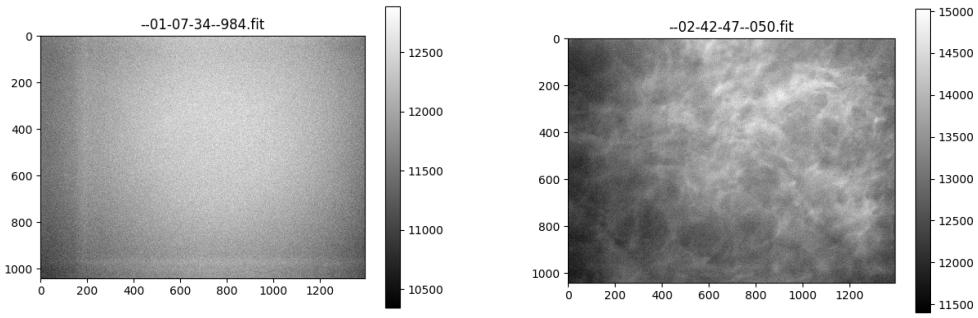

Figure 2.13: Star camera snapshots during the skydip at 1:07 UTC and approximately an hour later at 2:42 UTC. The image on the right shows structure similar to what is expected from PMCs.

2.8.3 Ice Clouds

Early in the flight we had trouble getting pointing solutions from the star cameras. This can be seen in some of the captures shown in figure 2.13 where the background stars are barely discernible if at all. Captures from later in the flight showed structures which are similar to polar mesospheric clouds (PMCs) which are extremely high altitude ice clouds. PMCs form around the polar summers and incidentally coincide with optimal launch conditions for the Antarctica Long Duration Balloon program. The balloon borne experiment EBEX captured PMCs with their star cameras and motivated a follow up experiment PMC Turbo specifically designed to image PMCs from the stratosphere. We have good reason to believe that the structures we see from captures later in the flight at least in some part come from PMCs. This is further confirmed with data from the day of the launch (Jan 6th) from the AIM-CIPS PMC satellite, figure 2.14,

What effect would ice clouds have on the skydip? Ice particles would increase the opacity of the atmosphere and thus could potentially provide this factor of three.

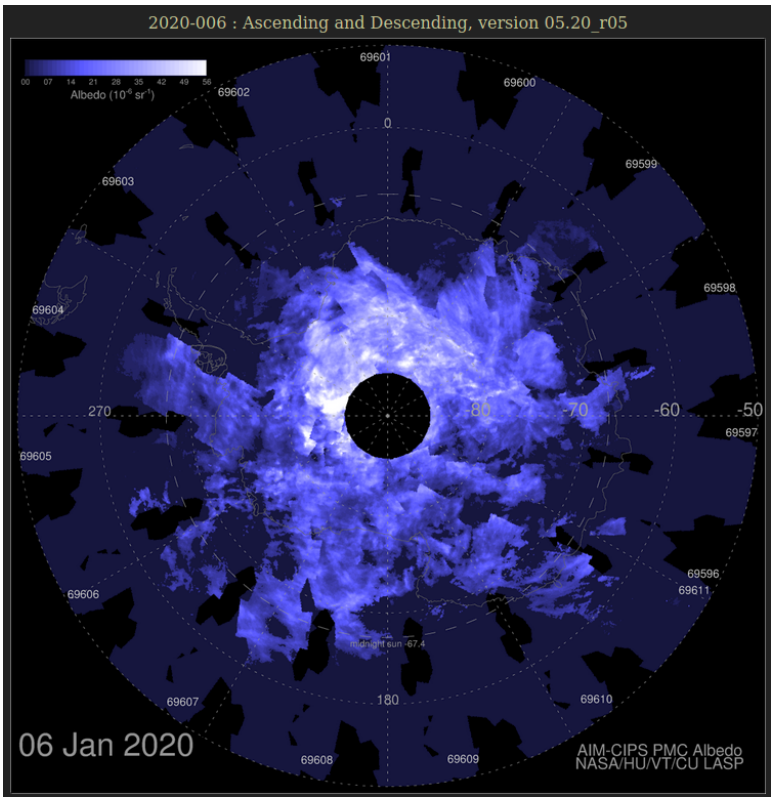

Figure 2.14: AIM-CIPS PMC albedo measurement of the southern hemisphere for Jan 6th 2020. The PMCs are nearly covering the entire Antarctic continent.

The am software allows for the inclusion of ice and liquid water clouds when given a characteristic ice water path (IWP g/m^2) or ice water content (IWC g/m^3). The CIPS instrument also provides a measurement of the ice water path of the PMCs, for Jan 6th the higher end of the measurements were around 200 g/km^2. If we use this IWP at the highest layer in the am simulation we end up with the curves in figure 2.15. The simulation with a PMC gives almost no change to the angular dependent brightness temperature. This leads to the question, exactly how high of an ice water path is required? or more generally what excess opacity?

It was found that adding an ice cloud with an ice water path of approximately 12 g/m^2 provides the correct opacity, figure 2.16. This value is far greater than

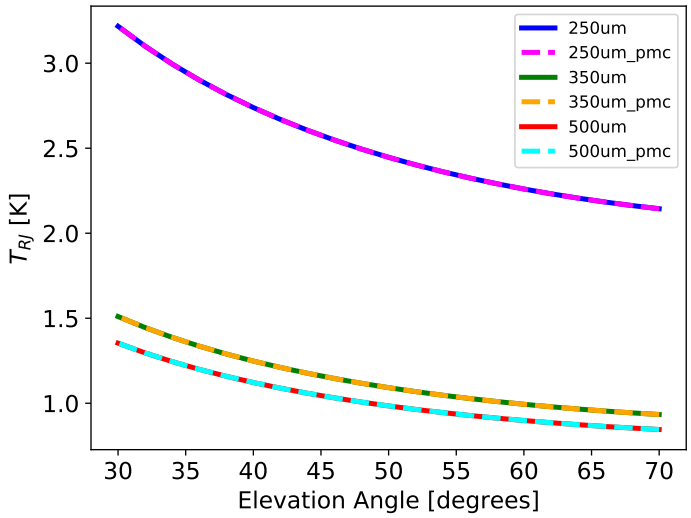

Figure 2.15: Simulated skydip with am software for the 250, 350, and 500um arrays with a 30% bandwidth at an altitude of 35 km. The Rayleigh-Jeans brightness temperature for a single mode vs elevation angle (90-zenith angle) for the cloudless atmospheric model in solid lines and dashed lines for the same model with a PMC IWP $\approx 2 \times 10^{-4}$ g/m^2. Typical values for a PMC create almost no change to the predicted angular dependence of brightness temperature.

what has been measured for PMCs and actually corresponds to typical IWPs for cirrus clouds measured by airborne submillimeter radiometers, Evans *et al.* (1998). Although the typical altitudes for cirrus clouds are from 5-15 km, far lower than the float altitude of the telescope.

2.8.4 Wildfire Smoke

In late 2019 and early 2020 Australia suffered one of the worst wildfire seasons to date. The fires released record amounts of burn products into the atmosphere and was measured by numerous Earth observing satellites. The smoke was carried across New Zealand and sat in the Pacific for some time, some early plumes headed south

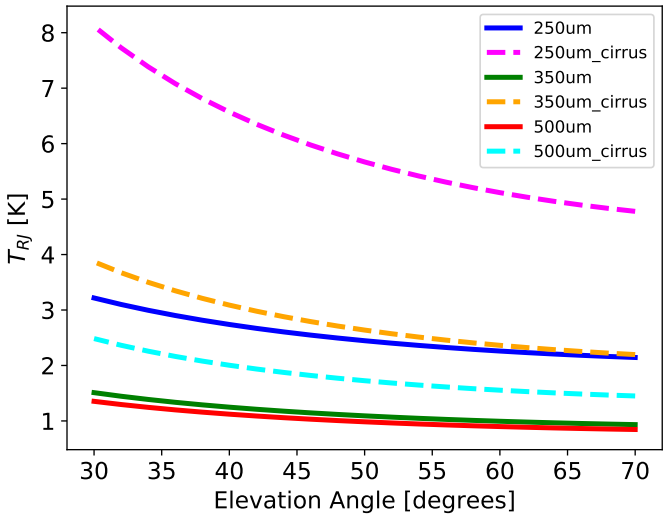

Figure 2.16: Simulated skydip with am software for the 250, 350, and 500um arrays with a 30% bandwidth at an altitude of 35 km. The Rayleigh-Jeans brightness temperature for a single mode vs elevation angle (90-zenith angle) for the cloudless atmospheric model in solid lines and dashed lines for the same model with an IWP $\approx 12 \;\; g/m^2$.

towards the polar vortex. The biomass burn products were measured reaching record altitudes by the AURA-MLS, Schwartz *et al.* (2020), some making it into the middle stratosphere. The high absorption of sunlight by the carbon products is thought to be the main mechanism transporting the smoke from the troposphere into the stratosphere. If even a small amount of this smoke made it to the stratosphere near McMurdo then this could increase the opacity of the sky and thus may explain our factor of three.

To set a bound on the required column density we can use the difference in opacity between the no ice cloud and cirrus equivalent cloud models, $\Delta\tau = 1.04\times10^{-2}$, 7.13×10^{-3}, 3.3×10^{-3} for 250, 350, and 500μm respectively. If we make the assumption that the smoke particles are small compared to our observation wavelength then we

can use the Rayleigh approximation. In this case we can estimate the optical depth due to the smoke as,

$$\tau = 18\pi NV\frac{\nu}{c}\frac{\epsilon"}{|\epsilon' + 2|^2}, \tag{2.25}$$

Where N is the column density, V is the volume of the smoke particle assuming spherical particles in this case, ν is the optical frequency, $\epsilon"$ and ϵ' are the real and imaginary permittivity of the particles. If we assume that the majority of the smoke particles are mainly composed of Carbon then, $\epsilon" \approx 2$ and $\epsilon' \approx 5$, Hotta *et al.* (2011). If we assume the particles are spherical and have radius $10\mu m$, then we get column densities of $N = 2.7\times10^8,\ \ 2.6\times10^8,\ \ 1.7\times10^8\ \ particles/m^2$. If we assume the smoke is only in the first atmospheric model layer which is 1680 meters thick and knowing that carbon has an approximate density of 2 g/cm^3 we can calculate the approximate smoke density at 35 km of 1.3, 1.2, and 0.8 mg/m^3. These values are about one to two orders of magnitude larger than what has been estimated by Peterson *et al.* (2021) for some of the dense stratospheric plumes.

2.9 RCW92

After performing the skydip we then turned to the next calibration task of focusing the secondary mirror. We had chosen to scan a well characterized point source from the previous flight of the BLAST experiment Fissel *et al.* (2010). The source was nicknamed Home and is located at RA $15^h13^m46^s$ and Dec. $-56°24'54"$ in J2000. All that was needed was to slew to those coordinates and scan back and forth while tuning the actuators on the secondary to maximize the signal amplitude. An unavoidable pointing error prevents this from being quite as easy. There is a small but unknown offset between the main pointing sensors and the sub-mm beam. Large raster scans were initially performed to account for this unknown offset, after a short amount of time we found a source within the scan to focus on. Following this we decided to

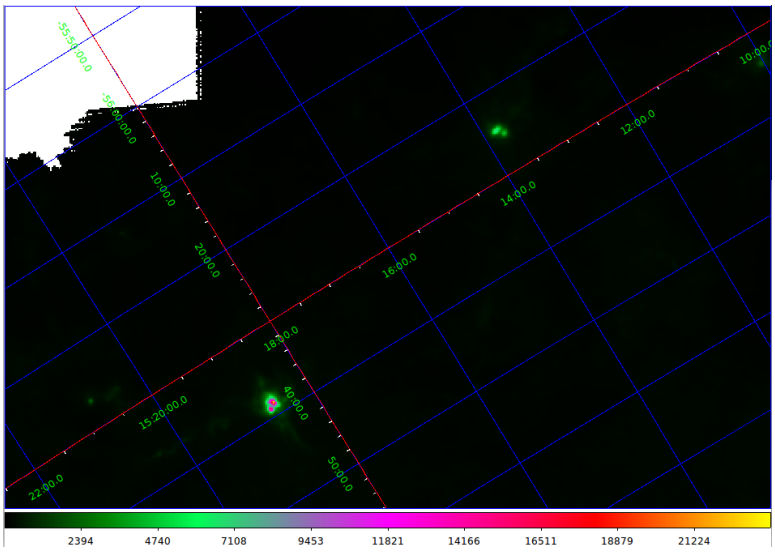

Figure 2.17: Herschel SPIRE instrument 350um map for patch of sky with both sources, Home in the top right and RCW92 in the bottom left. Colorbar is in units of MJy/Sr.

perform another fine raster over the source.

Post-flight analysis of the pointing solutions and comparisons to the Herschel maps of the same patch of sky helped us to conclude that we were looking at RCW92, Rodgers *et al.* (1960). Figure 2.17 show the two sources Home and RCW92 from the Herschel space telescopes 350um band. The offset between the two is $\sim 1/4°$.

Scans across the source revealed it's double peaked nature and verified some of our earlier suspicions about the 350 and 250um beams. Figure 2.18 shows a single detector timestream from the 350 and 500um arrays overlayed with a cross section of the source as measured by Herschel. The nearly matching time ordered data (TOD) for the 500um array suggests that we were close to the diffraction limit. The 350um TOD on the other hand shows a wide pedestal feature near the base of the source which is not present in the Herschel trace. We believe this was caused by a slight bowing in the cold dichroic filter. A small amount of bowing with a radius of curvature

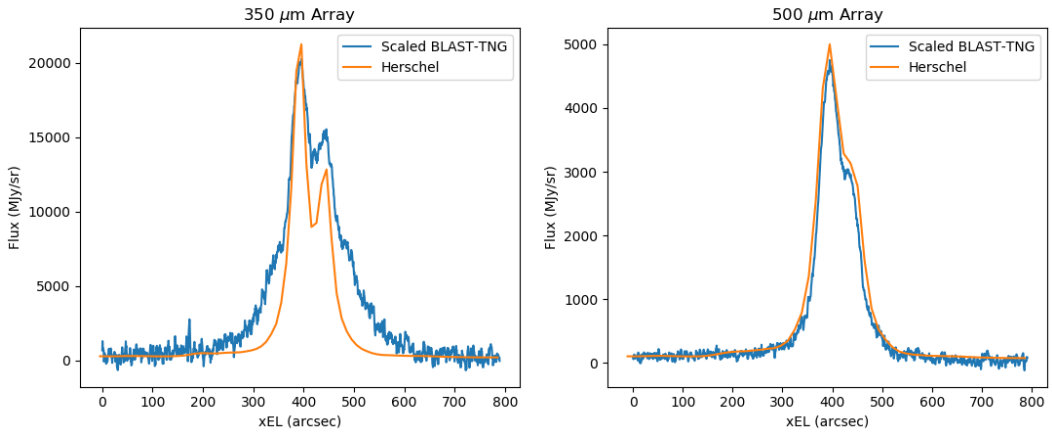

Figure 2.18: Cross section of Herschel maps across RCW92 overlayed with BLAST-TNG single detector timestreams from the 350 and 500um arrays.

around 2 meters was measured by the TolTEC team in pre-deployment tests. Their dichroic used the same process as the ones supplied to BLAST. The effect of a slight bow was simulated for TolTEC in the optics software ZEMAX giving a pedestal to the beams and a reduced point source sensitivity. The 500um array is not affected by this being only transmission through the dichroics, the 350 and 250 however both require a reflection.

The focal plane arrays were designed with a $2F/\lambda$ spacing meaning that each detector beam is separated by an entire beam on the sky. While this maximizes the coupling efficiency and limits optical cross talk it may complicate the scanning strategy. A point source may slip through undetected if it passes through these in between beams for which the sky is not sampled with high antenna gain. Typically multiple raster scans or a Lissajous pattern is preferred to account for this undersampling of the sky. We performed only one focused raster scan and thus only a fraction of the detectors half power beam passed directly over the source. This is evident in the histograms of the measured signal to noise shown in figure 2.19. The point source

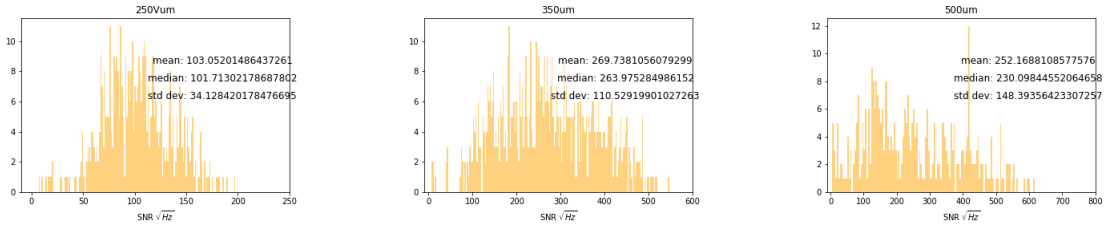

(a) 250um array V (b) 350um array (c) 500um array

Figure 2.19: Measured signal to noise histograms on RCW92 for the three bands.

sensitivity would be highly skewed by the detector channels that did not pass directly over the source. To account for this we use the top 10 highest signal to noise channels to estimate point source sensitivity.

2.9.1 NEFD from RCW92

We used the Herschel maps of RCW92 and our measured signal to noise to get the noise equivalent flux density (NEFD) and also point source NEP. Specifically the Herschel maps used in this analysis are,

`hspireplw_30pxmp_1500_m5859_1456923477424.fits`

`hspirepmw_30pxmp_1500_m5854_1456923485675.fits`

`hspirepsw_30pxmp_1500_m5856_1456923501575.fits`.

These maps were then smoothed with a normalized to the peak 2D Gaussian of standard deviation corresponding to the ideal theoretical full width at half maximum for the three bands. Peak values from the smoothed maps are 29048, 13657, and 3422 MJy/Sr for the 250, 350, and 500um respectively. These can be converted into Janskys measured by our telescope under the ideal diffraction limited beam.

$$S_{source} = I_{source}\Omega_{beam} \times 10^6 \quad [Jy], \tag{2.26}$$

Array	500um	250Vum	350um	250Uum	250Wum
NEFD $[Jy/\sqrt{Hz}]$	0.57 ± 0.02	3.83 ± 0.16	1.27 ± 0.03	4.55 ± 0.56	4.49 ± 0.12

Table 2.2: Noise Equivalent Flux Density (NEFD) mean and standard deviation for the top 10 highest signal to noise channels from each array.

Where I_s is the specific intensity of the source in MJy/Sr, Ω_{beam} is the solid angle of the beam. Knowing the ideal full width at half maximum values θ_{fwhm} in arcseconds we can calculate the beam solid angle using,

$$\Omega_{beam} = 1.13 \times \theta^2_{fwhm} \times 400\pi^2. \tag{2.27}$$

Now we can calculate the noise equivalent flux density of the telescope for the measured given signal to noise on the source,

$$NEFD = \frac{1}{2}\frac{S_{source}}{SNR} = \frac{1}{2}S_{source}\frac{e_f}{\Delta f} \quad [Jy/\sqrt{Hz}] \tag{2.28}$$

The factor of 1/2 is due to using single polarization sensitive detectors limiting the measurable source flux. The signal to noise is explicitly written as the ratio of the measured frequency noise e_f and frequency shift Δf. NEFD can be related to the noise equivalent power by the relation,

$$NEFD = \frac{NEP}{A_{primary}\Delta\nu}, \tag{2.29}$$

Where $A_{primary}$ is the geometric area of the primary, $\Delta\nu$ is the optical bandwidth.

Using the top 10 highest signal to noise detectors from each array we get the following NEFDs listed in 2.2.

2.9.2 Polarization of RCW92

RCW92 is an HII region of active star formation with young stellar objects embedded in a bubble of gas and dust, Moisés *et al.* (2011). To check if the region

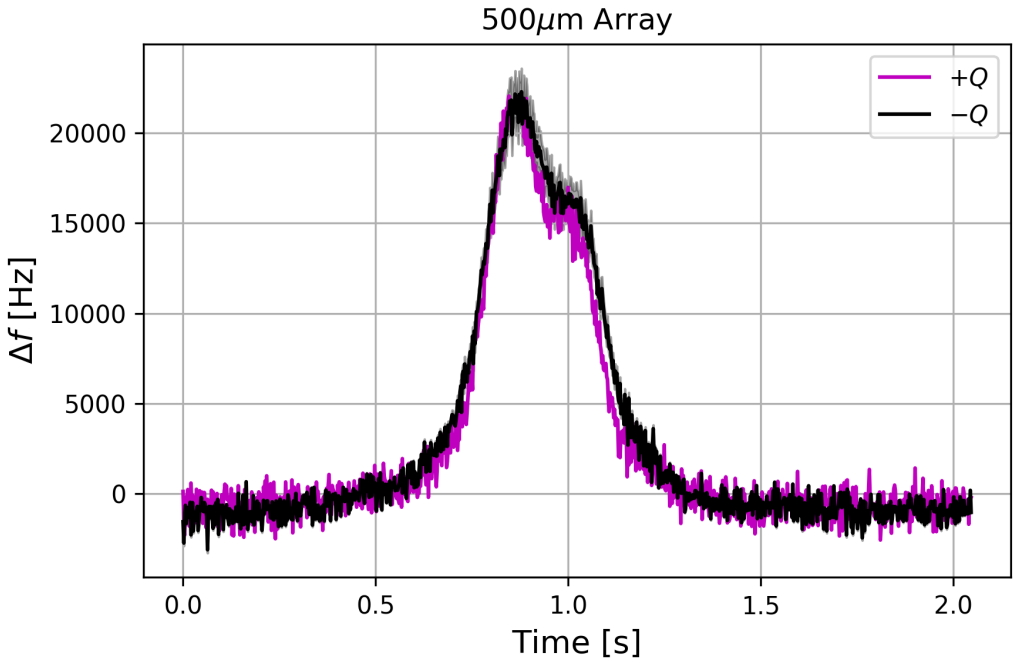

Figure 2.20: RCW92 scans from orthogonal polarizations after flat fielding.

has any significant sub-mm polarization we look at scans across the source from the same pixel. Each pixel contains two detectors of orthogonal polarization and thus we can get a quick estimate of the polarization just by looking at the +Q/-Q (or +U/-U) pairs. Figure 2.20 shows the two detector timestreams from the same pixel, each timestream has been scaled by the response to the cal-lamp accomplishing a non-polarized flat fielding. From the uncertainty in the cal-lamp flat fielding and noise we can conclude that the polarization fraction is less than 5% at 500um.

2.10 Frequency Noise Stack-Up

A quadrature readout provides the orthogonal components of the complex transmission which can be used to disentangle the different contributing noise sources. The main noise contributors for our system are thought to be photons, phonons, the low noise amplifier, and D/A quantization noise. Assuming that each noise source

is uncorrelated we can write the sum of squares for the two frequency quadrature directions as,

$$S_{xx} = e^2_{photons} + e^2_{phonons} + e^2_{amp} + e^2_{quant} \tag{2.30}$$

$$S_{yy} = e^2_{amp} + e^2_{quant} \tag{2.31}$$

where S_{xx} is the frequency direction noise, S_{yy} is the dissipation direction noise both in units of Hz. The photon and phonon contributions are significantly reduced in the dissipation direction because it has been divided down by a factor $\beta^2 > 200$, which is the ratio of frequency to dissipation response. This allows the difference of the two $\Delta S = S_{xx} - S_{yy}$ to provide and estimate of the photon and phonon contributions. Figure 2.22 shows the difference for one of the 250um arrays as a histogram for the light detectors and vertical lines for the dark detectors in units of $Hz/\sqrt{Hz}$.

In the dark detectors this difference will be dominated by the phonons. Using the fits to equation 2.9 and the measured difference for the darks of each array we can calculate an equivalent phonon fluctuation temperature δT as,

$$\delta T = \frac{dT}{df} e^{-1}_{phonons}. \tag{2.32}$$

Which gives 27, 50, and 130 $nK/\sqrt{Hz}$ for the 250, 350 and 500um arrays respectively.

The contribution due to photons can be isolated if we assume that the thermal fluctuations measured by the dark detectors is also present in each of the light detectors. The frequency noise due to photon absorption follows,

$$e_{photons} = \frac{df}{dP}\sqrt{2h\nu P_{abs} + 2\Delta_0 P_{abs}/\eta_{pb}}, \tag{2.33}$$

where the first term under the square root is the photon shot noise and the second term is the noise due to recombination of quasiparticles, df/dP is the detector responsivity, and η_{pb} is the pair breaking/recombination efficiency.

The primary dissipation direction noise contributors are the low noise amplifier and the D/A. These can be converted to a frequency noise using the derivative of the complex transmission of the resonator with respect to frequency,

$$\delta e_f = \frac{\delta e_v}{V_{in}} \frac{df}{dS_{21}} = \frac{\delta e_v}{V_{in}} \frac{Q_c f_0}{2Q_r^2} \tag{2.34}$$

Where Q_r and Q_c are the total and coupling quality factors. V_{in} is the voltage at the input of the detector. The noise power spectral density for the low noise amplifier is given by Johnson-Nyquist as $P/B = kT$, where T is the equivalent noise temperature referenced to its input. Along with equation 2.34 we can write the frequency noise due to the amplifier as,

$$e_{amp} = \sqrt{\frac{kT}{P_{in}}} \frac{Q_c f_0}{2Q_r^2}. \tag{2.35}$$

The digital to analog converter used for frequency comb generation also produces a noise floor which is significantly above the room temperature thermal floor. Without sufficient attenuation this can contribute to the total noise. The quantization noise variance is given by $q^2/12$, Bennett (1948), where the quantizer voltage step $q = V_{FS}/2^{N_{bits}}$ with a full scale voltage V_{FS} and number of bits N_{bits}. The quantization noise power spectral density is then given by,

$$\delta P_{quant} = \frac{1}{6Z_0} \frac{V_{FS}^2}{2^{2N_{bits}}} \frac{1}{f_s}, \tag{2.36}$$

Where Z_0 is the impedance and f_s is the sampling frequency of the D/A. The quantization noise is solely dependent on the digitizer parameters but there are other non-linear effects that produce spurious tones that are typically captured by an equivalent number of bits (ENOB). Thus if we know the ENOB and full scale voltage we can estimate the frequency noise due to the D/A as,

$$e_{quant} = \sqrt{\frac{\delta P_{quant} L}{P_{in}}} \frac{Q_c f_0}{2Q_r^2}. \tag{2.37}$$

Where again we have P_{in} as the power at the input to the detectors, L is the total loss from the D/A to the detectors. It is interesting to note that $P_{in} = P_{tone}L$, where P_{tone} is the power per tone measured directly at the output of the D/A, which simplifies the radical to the phase noise $\mathscr{L}(f) = 10log_{10}(\delta P/P)$ which can be directly measured**?**.

The in-flight detector timestreams were used to find the frequency noise in both quadratures S_{xx} and S_{yy} for the three bands. Splitting the noise in into the four main components described above the in-flight results are presented in table 2.3. For the 250 and 350 micron arrays the photon noise is comparable to the sum of squares of the other contributors. These arrays also have an amplifier noise which is higher than the quantization noise which means that we could have driven the arrays with more tone power without increasing the readout contribution. We still had yet to optimize the tone power in flight before the mechanical failure. The 500um array seems to have had a large readout noise which implies either that there was more loss to the arrays than expected or some other type of dissipation noise is at play such as an anomalously high LNA noise.

2.11 Noise Equivalent Power

The noise equivalent power (NEP) is a common sensitivity metric used to compare detectors and in some cases entire telescopes. The NEP is defined as the noise power of the system when the signal to noise ratio is equal to one. Typically the NEP is reported in units of W/$\sqrt{Hz}$ and can be calculated by measuring the noise and resposivity as,

$$NEP = \frac{\sqrt{S_{xx}}}{R} \tag{2.38}$$

where R is the responsivity in Hz/W and S_{xx} is the noise spectral density in Hz^2/Hz. This can be rewritten in terms of a measured signal to noise and difference in power

Array	S_{xx}	S_{yy}	$S_{xx} - S_{yy}$	$e^2_{photons}$	$e^2_{phonons}$	e^2_{amp}	e^2_{quant}
250	23.14	10.69	12.45	10.91	1.54	8.12	2.59
350	2.34	1.02	1.32	1.03	0.29	0.56	0.46
500	576.48	478.3	98.18	72.68	25.5	129.05	349.32

Table 2.3: Frequency noise for the three arrays from in-flight detector timestreams each in units of Hz. The first three columns give the measured median frequency noise for the frequency direction S_{xx}, the dissipation direction S_{yy}, and the difference. The noise is attributed to four main sources, photons, phonons, the amplifier, and the D/A quantization floor. The measured difference in the frequency quadratures contains noise due to photons and phonons, the dissipation noise contains only amplifier and D/A. The frequency direction noise contains all noise sources.

of the source,

$$NEP = \frac{\Delta P}{SNR}, \tag{2.39}$$

Where SNR is the measured signal to noise in units of $\sqrt{Hz}$ and ΔP is the optical power in Watts. The Δf timestreams are used to estimate the signal to noise for each source. The signal in the SNR is taken to be the peak to peak amplitude of the Δf response. The noise is estimated by taking the power spectrum of the Δf timestream. The NEP can also be related to the noise equivalent flux density (NEFD) as shown previously in equation 2.29.

Another relatively common metric within radio astronomy and experimental cosmology is the noise equivalent temperature (NET) measured in $K/\sqrt{Hz}$. To get the NET in the Rayleigh-Jeans limit we divide by Boltzmanns constant k and the optical bandwidth $\Delta\nu$,

$$NET_{RJ} = \frac{NEP}{k\Delta\nu}. \tag{2.40}$$

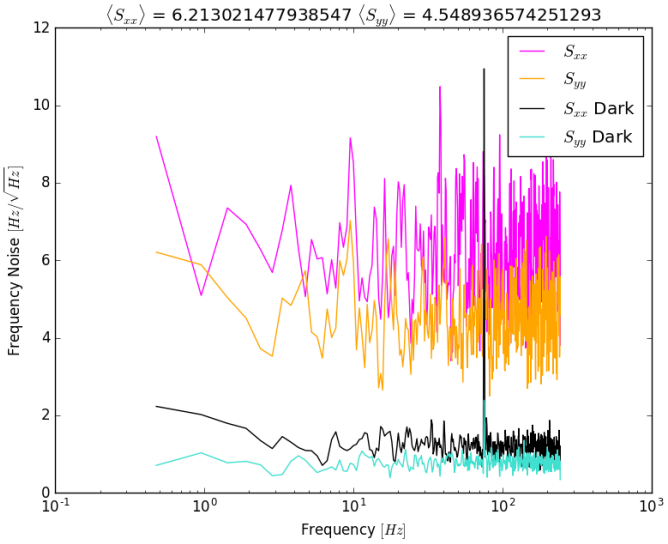

Figure 2.21: Noise power spectrum in the frequency quadrature $\sqrt{S_{xx}}$ and dissipation quadrature $\sqrt{S_{yy}}$. A separation between the two quadratures is seen with frequency noise being the greater of the two. This is a signature of detector noise domination if all other quadrature asymmetric noise sources have been ruled out.

There are two useful NEPs to report, the telescope optical NEP and the detector NEP. The optical NEP shown in Figure 2.23 is a measure of the total system sensitivity. The detector NEP shown in Figure 2.24 is corrected for the optical efficiency of the optical stack. The efficiency was determined from the ratio of the measured thermal source responsivity to the NIST responsivity. The main calibrators were the thermal load measurements, skydip, and RCW92. The calibration lamp depends on an external calibrator thus is not an independent calibration source. The light grey points for RCW92 are the mean and standard deviation of the total distributions. The colored points correspond to the top 10 highest signal to noise channels.

The thermal source and skydip calibrators are beam filling and thus relatively insensitive to beam imperfections. The NEPs from RCW92 are thought to be higher

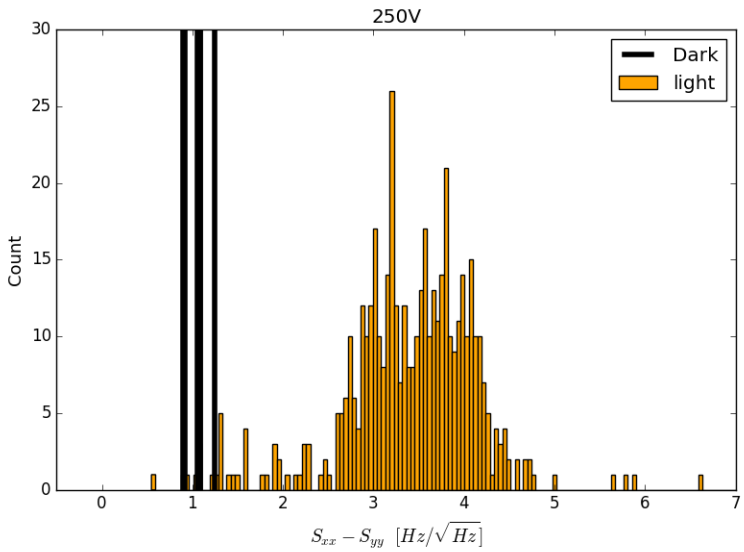

Figure 2.22: Histogram of the square root of the noise quadrature power difference for the 250um-V array. The black vertical bars are the frequency noise of the dark detector channels.

in the 350 and 250s due to the dichroic bowing issue. The reflection from the dichroic is equidistant for the 350 and 250 which implies that the beam divergence would be greater for the 250. This effect is seen in both the optical and detector NEPs.

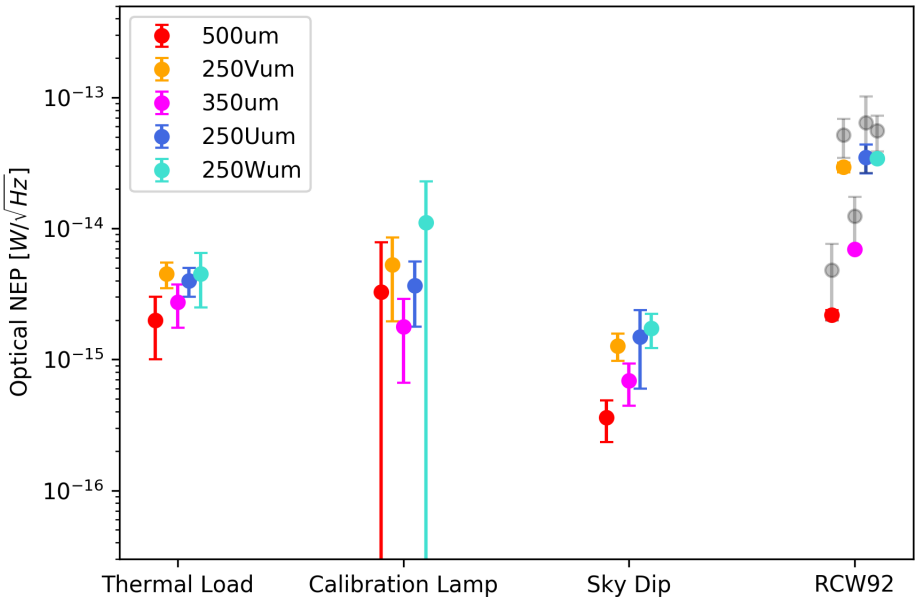

Figure 2.23: Optical NEP of BLAST-TNG for each array. The thermal load, skydip, and RCW92 values are the main calibrators. Colored points represent the top 10 highest signal to noise channels for RCW92 and the grey is the mean and standard deviation of the entire array.

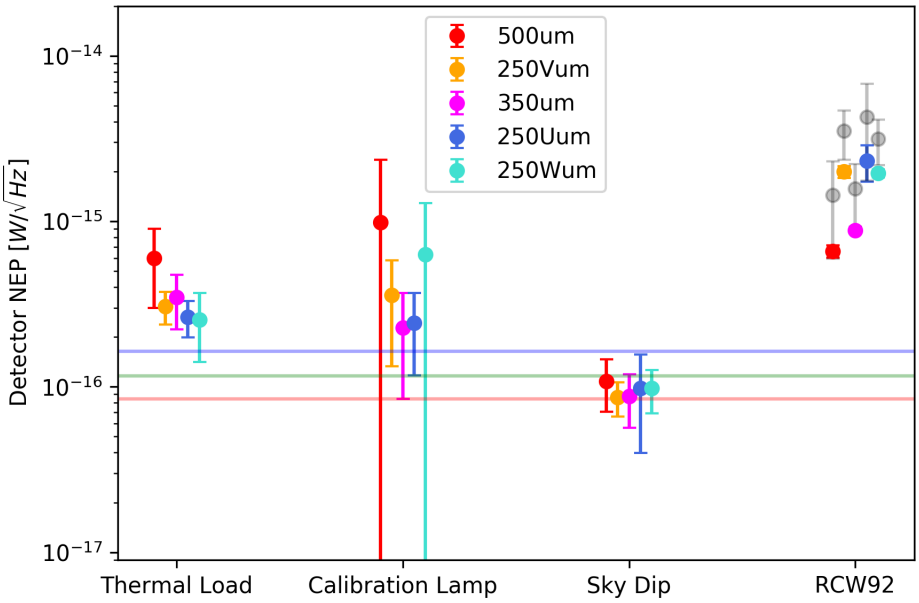

Figure 2.24: Detector NEP of BLAST-TNG for each array. Each is the optical NEP (2.23) divided by the measured optical efficiency. The blue, green, and red horizontal lines are the proposal detector NEPs for the 250, 350, and 500um respectively. Colored points represent the top 10 highest signal to noise channels for RCW92 and the grey is the mean and standard deviation of the entire array.

Chapter 3

RECONFIGURABLE READOUT ON THE RFSOC PLATFORM

For decades far-infrared telescopes have utilized superconducting detectors to map the sky. Years of development have lowered the intrinsic noise so substantially that the statistical fluctuations of the output signal are dominated by the absorbed photons. Individual detector performance for imaging instruments have been limited by this photon noise coming from the atmosphere and/or warm optics. Reducing the atmospheric contribution motivates the use and thorough investigation of various high-altitude and dry sites around the globe. The optics loading can be reduced by precision machining and cooling or even submersion in liquid cryogens. Even then with the best sites available and the lowest achievable primary emissivity, groups have reported photon noise dominated performance. The only available way to reduce this any further is by increasing the number of detectors.

Larger arrays increase system complexity and push on cryogenic constraints due to the required biasing and readout circuitry. Borrowing from the field of digital communications, methods of multiplexing have been and are currently being explored to ease this issue. Some of the methods used for Transition Edge Sensors (TESs) have been: time division (TDM), code division (CDM), and frequency division (FDM). TDM reads a single detector at a time switching between all detectors giving a frame rate. While this reduces readout complexity it comes at the cost of lower frame rates. CDM utilizes the orthogonality of different waveforms or codes to mux the response of the detectors. Kinetic Inductance Detectors (KIDs) however are intrinsically frequency multiplexed and thus have mainly employed FDM.

There has been significant progress in developing custom room temperature read-

out for KIDs, Mazin *et al.* (2013); Gordon *et al.* (2016); Paiella *et al.* (2019); den Hartog *et al.* (2011); Maloney *et al.* (2010); Akerib *et al.* (2012); Bourrion *et al.* (2016); Henderson *et al.* (2018) and TESs, Henderson *et al.* (2018); Kernasovskiy *et al.* (2018); Henderson *et al.* (2016); Jackson *et al.* (2011); Bender *et al.* (2014). While SNSPDs, Allmaras *et al.* (2020); Doerner *et al.* (2017); Sinclair *et al.* (2019) and QCDs, Echternach *et al.* (2018), which are novel devices still forming multiplexing schemes and readouts. Recent work in FDM capable readout has involved the development of generalized software and firmware modules targeting new hardware platforms using either field programmable gate arrays (FPGA) or graphical processing units (GPU) for laboratory measurements Minutolo *et al.* (2019). By far the most widely adopted readout platform for frequency multiplexed arrays has been an open source FPGA board developed by the *Collaboration for Astronomy Signal Processing and Electronics Research* (CASPER) known as the Reconfigurable Open Architecture Readout Hardware Version 2 (ROACH2). The ROACH system garnered a broad appeal and become the favored platform for readout systems with help from trend setters like MUSIC(Maloney *et al.* (2010)) and ARCONS(Mazin *et al.* (2013)). The ROACH2 has also been reinforced by CASPER's open source community which developed many firmware modules and control software to use with the ROACH2 for designers.

Since the release of the ROACH2, commercial hardware platforms used for digital communication systems have improved substantially with new ultra wide-bandwidth capabilities pushing into the many gigahertz. The Xilinx Radio Frequency System on a Chip (RFSoC) is one such system which integrates high speed digitizers (>4 GSPS), a programmable logic (FPGA) fabric, and a Linux-capable ARM processor; all on a single chip, rfs (2020). This system is a significant increase in the total bandwidth capabilities and a simultaneous reduction in system size, weight, and power

(a) The *ROACH2 MOTEL*, a stack of five ROACH2s which readout the five LEKID arrays for BLAST-TNG.

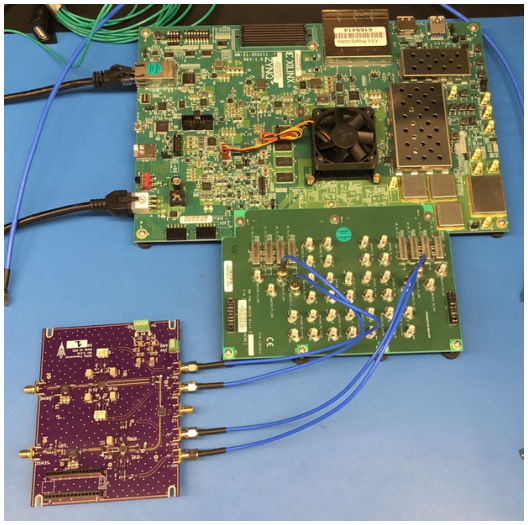

(b) Xilinx RFSoC ZCU111 development board with SMA breakout connected to a prototype TolTEC IF board.

Figure 3.1

in comparison to the ROACH2 system. A comparison of the SWAPC&B is given in table 3.1. From resource utilization reports (table 3.2) the RFSoC should be able to accommodate at least 8 BLAST-TNG equivalent systems. Thus the entire ROACH Motel could be replaced with one RFSoC in future instruments. This will allow the focal planes to grow for increased field of view and thus an increase in mapping speed providing higher science returns. The system on a chip architectures like the RFSoC provide such broad applicability that readout of future astronomical instruments may only differ in the firmware and software implementations.

The following sections describe the implementation and testing of a BLAST-TNG equivalent design on the RFSoC and the investigations of a couple of alternative firmware designs with suggestions for future research.

Platform	FPGA	Processor	Size	Power [W]	Digitizer Sampling Rate	Number of Digitizers	Memory	Cost [USD]
ROACH2+MUSIC	Virtex-6 (XC6VSX475T)	440EPx	1U	60	550 MSPS	2	QDR II+	7095
RFSoC ZCU111	Zynq Ultrascale+ ZCU29DR	ARM Cortex A54+R5	1U	26	4096 GSPS	8	DDR4	8995

Table 3.1: SWAPC&B comparison between the CASPER ROACH2 system and RFSoC ZCU111 development board.

Resource	BLAST-TNG Firmware Utilization	XCZU28DR (RFSoC Gen 1)
Logic slices	9599	930300
DSPs	370	4272
BRAM (Kb)	176	38000

Table 3.2: BLAST-TNG firmware FPGA resource utilization compared to the available resources on the RFSoC FPGA.

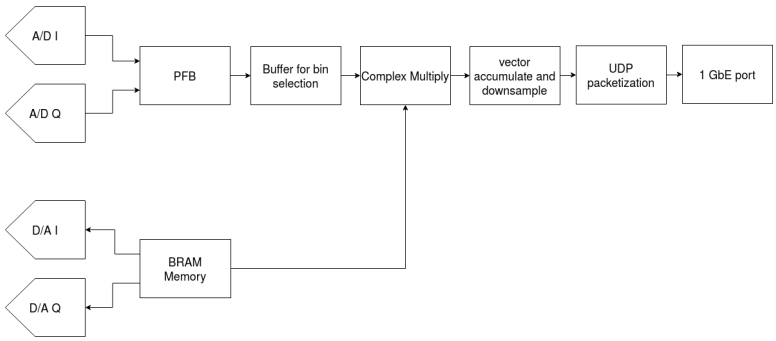

Figure 3.2: Block diagram of the BLAST-TNG to RFSoC design. The same fundamental modules are present as in the BLAST design. The main difference is that the waveform look up table is implemented in BRAM instead of the QDR memory as in the ROACH2.

3.1 Current Design

The current working design implements a BLAST-TNG equivalent system which can readout over 1000 channels with complex signaling over a 512 MHz bandwidth. The accumulated and downsampled data is packetized and transmitted as UDP packets over a 1 gigabit ethernet link. The conceptual block diagram is shown in figure 3.2. The Vivado block design however, shown in figure 3.3, is less illuminating but what is compiled. In the following sections I describe the digital design and its operating principles starting with the frequency comb generation and finishing with measurements of the system noise.

3.1.1 Frequency Comb

A frequency comb is required to drive the resonators, borrowing from the field of communications each can be thought of as a carrier in which the state of the resonator is encoded. This comb of carriers need to have a frequency resolution which is approximately a factor of 10 less than the full width at half maximum of the

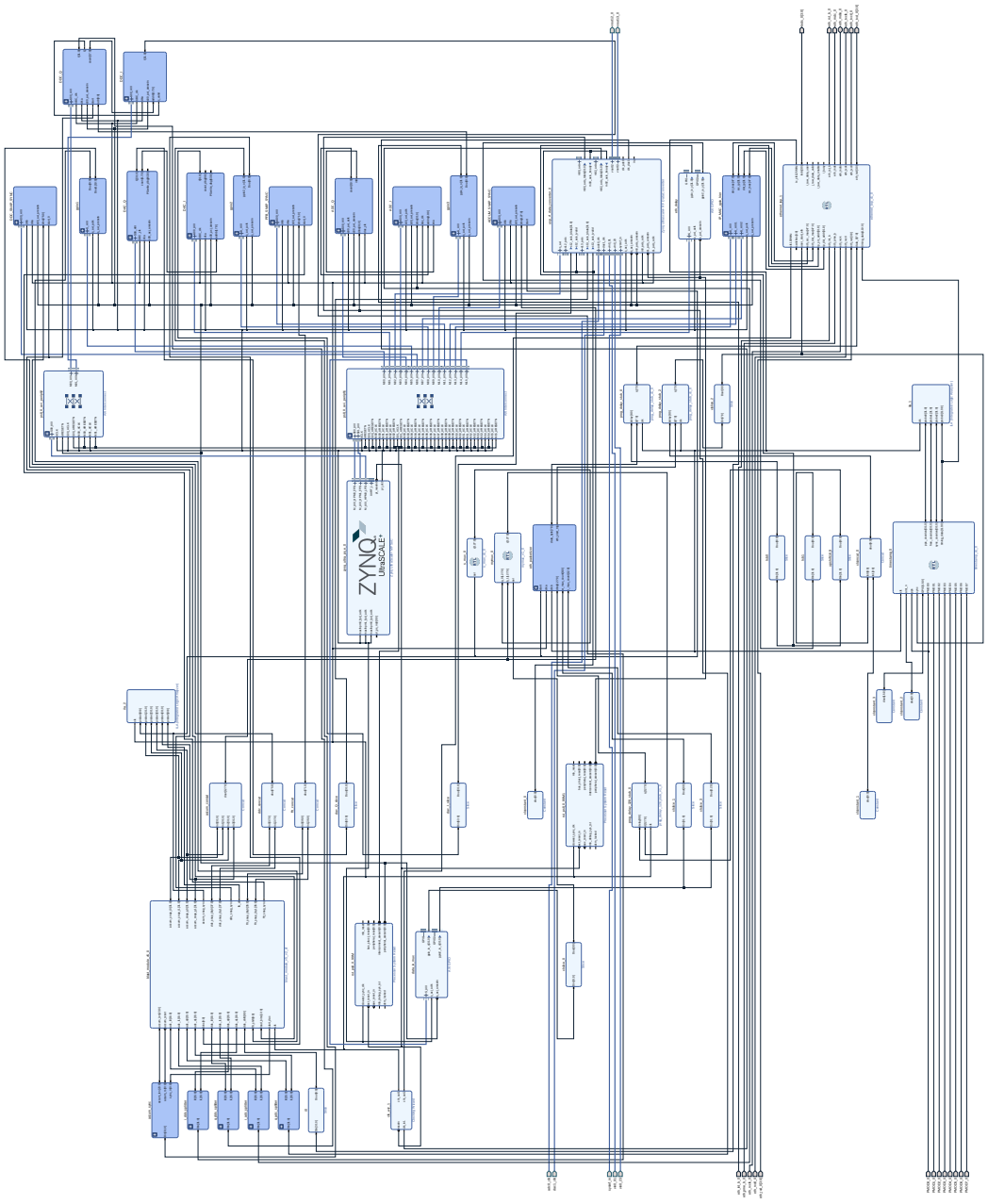

Figure 3.3: The Vivado 2018.3 block design of the BLAST equivalent system.

resonators. This ensures operation in the linear regime of the resonators. It also needs to be re-writable at some rate dependent on the loading and detector responsivity. For instance a balloon borne telescope will have less drastic loading changes than a ground based telescope and thus would require less frequent re-writing. Our current method utilizes look-up tables (LUTs) to store the arbitrary waveform. An inverse Fourier transform is computed on the list of resonant frequencies, this creates the time domain arbitrary waveform which is stored in the LUT. The length of the LUT and sampling rate of the digital to analog (D/A) converter determines the frequency resolution, $\Delta f_{min} = f_{samp}/L_{LUT}$. We follow this length requirement to assure phase continuity at the ends of the waveform, discontinuities will generate spurious signals. For BLAST we have $f_{samp} = 512 \;\; MHz$ and $L_{LUT} = 2^{21}$, giving approximately 244 Hz frequency resolution. The current design uses the Block RAM (BRAM) to store the LUT and is set to a length of $L_{LUT} = 2^{19}$ giving 977 Hz resolution.

Frequency Comb Derivation

A derivation of the inverse Fourier transform method of frequency comb generation. First we create a spectrum with unmodified amplitudes A_k and phases θ_k,

$$X(\omega) = \sum_{k=0}^{N} A_k e^{j\theta_k} \delta(\omega_k). \tag{3.1}$$

The amplitudes A_k can represent a total amplitude correction such as for transfer functions, The phases θ_k are typically randomized or algorithmically generated phases to minimize the resultant crest factor of the waveform. Using the following equation for discrete inverse Fourier transforms,

$$f(t) = \sum_{p=0}^{N} F(\omega_p) e^{-j\omega_p t} \tag{3.2}$$

Where $F(\omega_p)$ is the spectrum over which to transform into the time domain. Now we get the complex timestream,

$$x(t) = \sum_{p=0}^{N} \sum_{k=0}^{N} A_k e^{j\theta_k} \delta(\omega_k) e^{-j\omega_p t} \tag{3.3}$$

Keeping only the terms where $\delta(\omega_k = \omega_p)$ leaving,

$$x(t) = \sum_{k=0}^{N} A_k e^{j(\theta_k - \omega_k t)}, \tag{3.4}$$

Which is a sum of complex sinusoids with frequencies matched to the resonators. This is then written to the LUT as,

$$I(t) + jQ(t) = Re\{x(t)\} + jIm\{x(t)\}. \tag{3.5}$$

D/A Response

The digital to analog converter used to generate the frequency comb modifies the output with it's own transfer function. The discrete sampling nature of the digitizer gives it a $sinx/x$ frequency response where $x = \pi f / f_s$. This causes multiple aliases of the waveform to appear reflected across every $f_s/2$ boundary, see figure 3.4. Every $f_s/2$ region is called a Nyquist zone, from $0 - f_s/2$ is the first, $f_s/2 - f_s$ is the second and so on. Typically these higher Nyquist zones are filtered off by a low pass filter with a cutoff equal to the top of the first Nyquist. Higher Nyquist zones can be used with band pass filters if the application can afford it. The D/A transfer function falls off at higher frequencies and thus attenuates any waveform reducing the signal power. Figure 3.5 shows the output of the D/A when generating a frequency comb with 1000 tones measured with a spectrum analyzer.

Coarse and Fine Channelization

From the onset the plan had been to use the CASPER PFB for the first stage of channelization. As the work progressed it seemed reasonable to package as much of

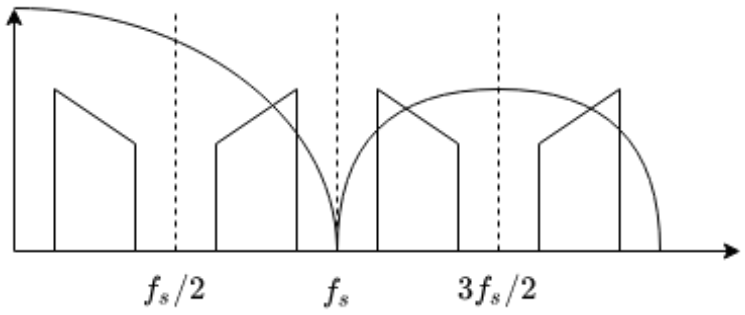

Figure 3.4: Graphic to show the sinx/x D/A response and Nyquist zones and aliased waveforms. The curved line roughly represents the sinx/x response and the trapezoidal feature is some arbitrary waveform. The dashed vertical lines represent the Nyquist zone boundaries for which the waveform is mirrored.

the DSP as possible into one module. The BLAST-TNG design was developed on MATLAB's Simulink with Xilinx ISE system generator on versions which are almost 10 years older than the current version of Xilinx's Vivado software. With considerable work the design which depended on various modules from the CASPER library was imported into a version of MATLAB's Simulink compatible with the desired version of Vivado 2018.3. The BLAST-TNG DSP module which contained the PFB, complex multiplier, and vector accumulator was compiled into a single module using system generator's HDL module compilation option. The compiled Simulink design is shown in figure 3.6.

The accumulated and downsampled data from the DSP module must get transferred from the FPGA fabric to some data storage. This is accomplished most easily at the data rates required by ethernet. The $\sim$ 32 Mb/s rate could be lowered by allocating less bits to each channel at the cost of dynamic range safety. If we knew the input power range more exactly the fixed point precision required would be less. We decided to use a four port 1 GbE FMC card, **?**, this allowed us to physically

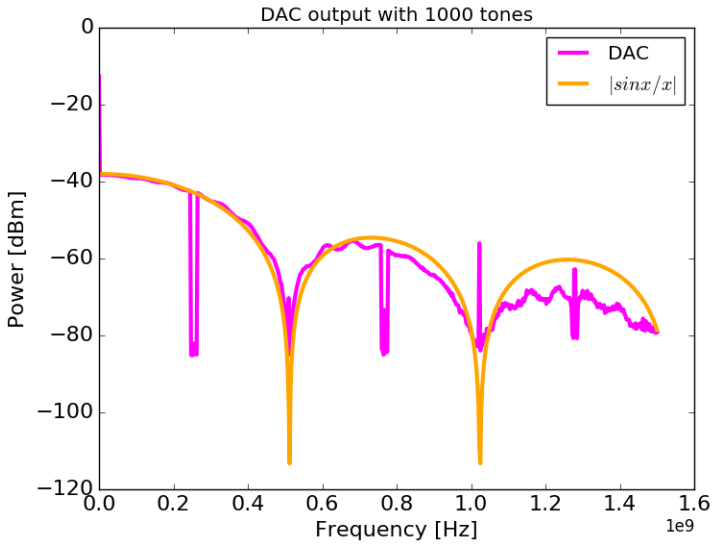

Figure 3.5: Directly sampling the output of the I component of the DAC without anti-alising filters using a spectrum analyzer. The transfer function is fit to a $|sinx/x|$ with $x = \pi f/f_s$ where $f_s = 512 \;\; MHz$. We can see after the end of the frequency comb at 255 MHz the 2nd Nyquist zone aliased tones appear. This is expected without anti-aliasing filters.

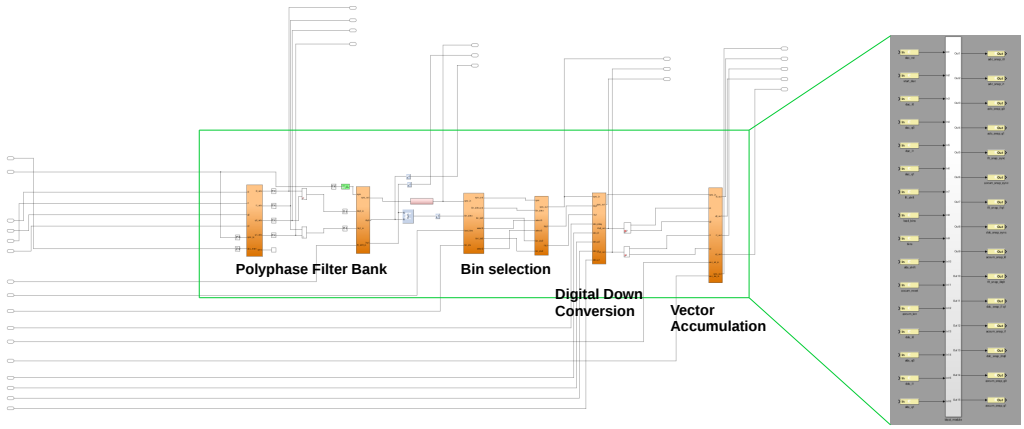

Figure 3.6: BLAST DSP module in Simulink.

```
In [1]: import os
        from pynq import Overlay
        from pynq import Xlnk
        import xrfclk
        import xrfdc
        import struct
        from time import sleep
        from matplotlib import pyplot as plt
        import numpy as np
        import ipywidgets as ipw
        from ipywidgets import interact, interactive, fixed, interact_manual
        from scipy import signal

In [2]: # FIRMWARE UPLOAD
        firmware = Overlay('bram_lutwave2p1.bit')
        # INITIALIZING LMK04208 CLOCK
        clksrc = 409.6 # MHz
        xrfclk.set_all_ref_clks(clksrc)
```

Figure 3.7: Jupyter Notebook initialization of firmware and clocks.

separate up to four parallel readouts on the same RFSoC fabric.

3.1.2 Software and PYNQ

PYNQ has offered a quick way to test designs via the combination of Python wrapped firmware drivers and Jupyter-notebooks. Custom notebooks accomplish many of the generic tasks of readout operation and are re-used without the need to recompile the microprocessor software. These generic functions include uploading the firmware and configuring clocks, Figure 3.7 shows the few lines required within the notebook for this. We further use the notebooks to perform the necessary arbitrary waveform calculations and LUT loading. We also use the notebooks for quick analysis with Matplotlib and Scipy shown in the next section.

3.1.3 DSP Module Verification

The majority of the digital signal processing (DSP) occurs within the BLAST-TNG module. Each stage contains output ports to provide operational status and diagnostics. There are four main stages after which to check the signals: directly after the ADCs, the polyphase filterbank, the digital down-conversion, and the vector accumulator. Each signal is captured into a dual port BRAM with control logic.

Figure 3.8: Jupyter Notebook showing it's use for grabbing data from the *snap* blocks and plotting. This screen grab displays the I and Q timestreams from the ADC and the spectrum computed by Python.

Adopting the heritage term from CASPER we call these snap blocks, implying that it's taking a snap shot of the data.

The ADC is the staring point for verifying the DSP. Because the system has been designed with the intent of interfacing with analog IQ mixers we use two ADCs in

the RFSoC, one dedicated to I the other to Q. To check that we are correctly using complex signals we can take the ADC snap data and perform a complex FFT. This should match the pre-IFFT spectrum of the frequency comb with some expected attenuation and noise due to being in physical loopback. An example of this is shown in figures 3.9 and 3.10 where a single and 1000 tone frequency comb was generated and the spectrum computed from the ADC data. Another important point is that the ADC data spectrum should have some asymmetry which is another quick check of complex signaling that can be done most easily with a single tone.

Second the PFB is used as the first stage of channelization. Again this is easiest to prove with a single tone loopback. Figure 3.11 shows the tone in one of 1024 bins. The PFB is overlapped and oversampled which accomplishes an even frequency response across a bin at the cost of overlap with the neighboring bins.

The digital downconversion and vector accumulator are typically checked by capturing multiple samples of the entire output spectrum. If the signal has not been correctly downconverted the signal will oscillate and lose signal to noise when accumulating. When the conversion is performed properly the signals have been converted to DC and thus do not oscillate. Any fluctuations after this are actual modulations of the carrier which are the signals to be measured. A correctly downconverted accumulated and downsampled output is shown in figure 3.12.

3.2 Readout Noise Measurements

The readout systems described here use quadrature signaling to generate unique upper and lower sidebands. The terminology is followed through the digital signal processing and thus we also consider the detector timestreams as having the quadrature signals I and Q. These represent a complex number with an in-phase component

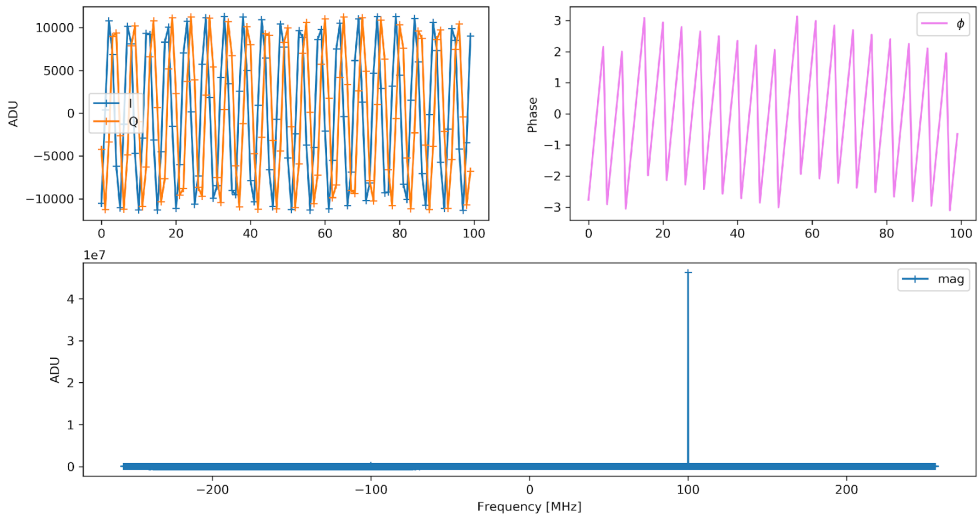

Figure 3.9: This figure shows a snapshot of data captured within the firmware after the ADCs. Two ADCs are employed in the design for interfacing with IQ demodulators. The phase is given on the right as arctan(Q/I). The spectrum of the complex ADC timestream is given in the bottom plot. This shows that the waveform output from the DAC is indeed complex as it can be seen that the spectrum is not symmetric.

and quadrature component,

$$Z(t) = I(t) + jQ(t) = I_0 + \delta I(t) + j(Q_0 + \delta Q(t)), \tag{3.6}$$

where both I and Q have some time dependent noise term δ which we would like to measure. A typical measure of noise that will provide an accurate description under certain assumptions is the variance. The variance will provide an estimate of the noise power over the sampling bandwidth. When comparing different setups or specific frequencies it's sometimes useful to discuss the noise spectral density (NSD). This is the noise per unit bandwidth in Hz. While the noise estimated by the variance is integrated across the entire bandwidth we would have to assume that it's evenly

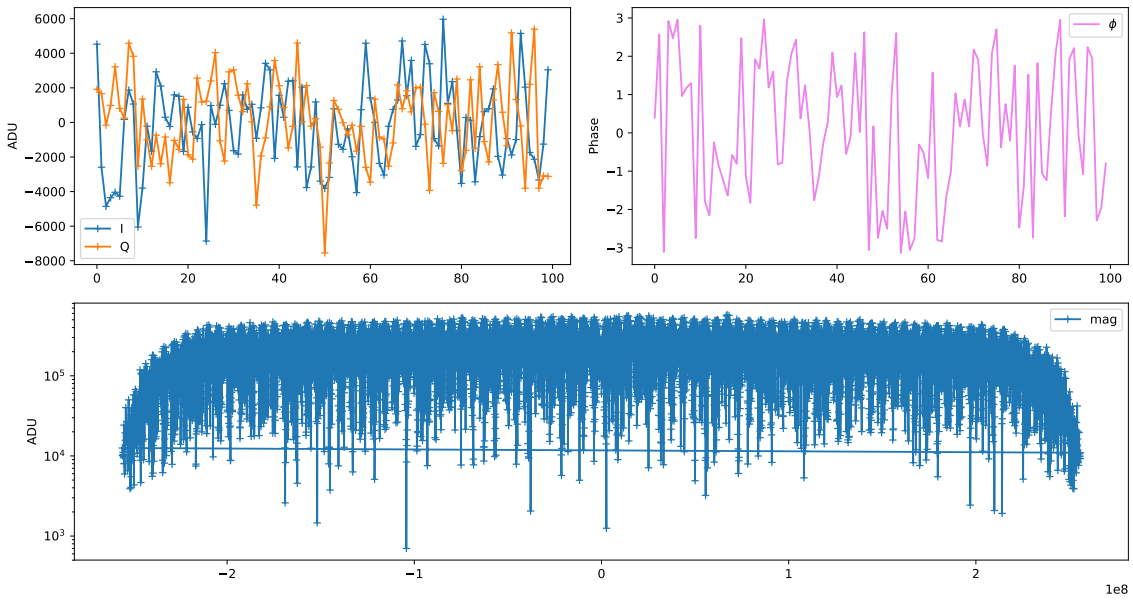

Figure 3.10: Loop back measurements directly from the ADC with a 1000 tone comb. The phase is calcuated as arctan(Q/I) and is shown in pink on the right. The magnitude of the Python computed spectra of the complex ADC timestream is given in the bottom plot. There are anti-aliasing low pass filters on the digitizers with a roll off that begins around 250 MHz and is visible in the band edges in the magnitude spectra.

spread out to calculate the spectral density. In the case of 1/f noise or spurious signals we would therefore want to use other methods to calculate the NSD. The variance can be directly calculated by integrating the power spectrum over all frequencies.

To calculate the power spectrum we use the Welch method, Welch (1967). This allows for the determination of the power spectrum with reduced noise at the cost of frequency resolution. This method first splits the time series into overlapping chunks and then applies a window function each. These are then discrete Fourier transformed and the spectra from chunks of the same length are averaged together after calculating the squared magnitude. This method provides a power spectrum

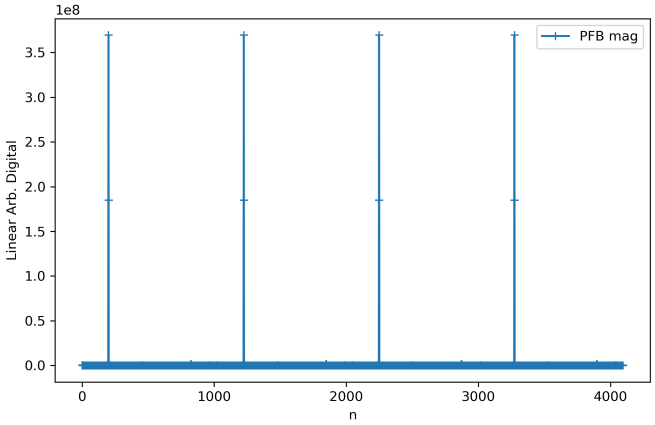

Figure 3.11: Polyphase filterbank (PFB) spectra capture for a single tone in loopback. The x-axis is the bin output order of the PFB. The 1024 point PFB outputs 512 positive frequency bins and 512 negative thus every 1024 is a new spectra.

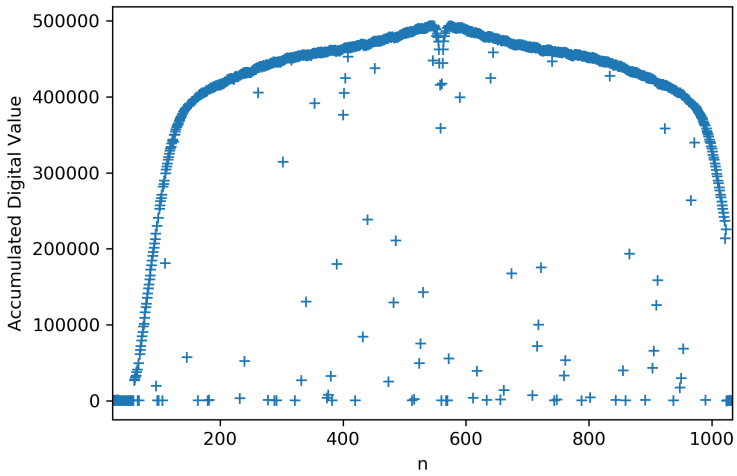

Figure 3.12: The magnitude of the downconverted and accumulated values for a 1000 tone comb. The frequency response of the system in loopback is clearly visible in the magnitude roll off near the edges of the channels.

with L/2 bins spanning half the sampling bandwidth. Luckily this method is provided by SciPy's signal processing library signal as welch. From here on out in computing

power spectrums the Welch method is used and can be assumed.

What does the power spectrum of I or Q tell us? The digital signal processing chain contains a fast Fourier transform, a complex multiply, and accumulator. Each of these operations only scale the raw values originally sampled by the A/D. This means that we can interpret the values as being proportional to Volts. Using the term PSD as short for power spectral density as calculated by the Welch method,

$$S_I(f) = PSD\{I(t)\} \;\; and \;\; S_Q(f) = PSD\{Q(t)\}. \tag{3.7}$$

Because I and Q are proportional to Volts the power spectrum gives a result proportional to power. These values can be calibrated when all of the following do not change, the tone frequencies, FFT shift, LO frequency, and accumulation length. Generally this is not calibrated due to the constant modification of the tone frequencies and LO. Even so a result which is proportional to power gives us the ability to verify the noise stack.

Phase noise is another way of characterizing the noise of the system. It provides a better estimate of the dynamic range or signal to noise. In this case the static tone power relative to the fluctuating noise. The phase is typically calculated as,

$$\phi(t) = tan^{-1}(Q(t)/I(t)). \tag{3.8}$$

The power spectrum is then taken of this phase timestream, $S_\phi = PSD\{\phi(t)\}$. The scaling factors within the firmware or any that are common to both I and Q are canceled in that the argument is a ratio of the two. This way of calculating the phase may provide an underestimate of the total phase noise. To show this we may assume that each value has a static term and fluctuation term then the argument of the arctan becomes,

$$\frac{Q_0 + \delta Q(t)}{I_0 + \delta I(t)} \approx \frac{1}{1 + \delta I/Q_0} \approx 1 - \delta I/Q_0, \tag{3.9}$$

under the assumptions that $\delta X << X$ and $Q_0 \approx I_0$. The argument is nearly one and then expanding arctanx around x=1 we get,

$$\phi(t) \approx tan^{-1}(1 - \delta I/Q_0) \approx \frac{\pi}{4} - \frac{\delta I(t)}{2Q_0}. \tag{3.10}$$

Thus the power spectrum is providing at most half the phase noise when calculated with arctan.

Another method of calculating the phase noise is to calculate the intrinsic noise of I and Q first then divide by the mean power of each,

$$S_\phi = \frac{1}{2}\frac{S_I + S_Q}{\langle I\rangle^2 + \langle Q\rangle^2}, \tag{3.11}$$

This is the single side band phase noise and can be related to the commonly used notation $\mathscr{L}(f) = 10log_{10}(S_\phi)$ in dBc/Hz.

3.2.1 Loopback Noise

The main way to measure the performance or dynamic range of the readout is by placing it in what is known as *loopback*. This is connecting the DACs to the ADCs with RF cables. Typically anti-aliasing filters are also used in series with the loopback cables. This configuration measures the highest possible signal to noise for the readout for a given sampling rate, number of tones, and accumulation length. Both the D/A and A/D add quantization noise to the signal to being generated and measured. This can be calculated from equation 4.11 as,

$$NSD(N_{tones}) = -6.02N_{bits} - 1.76 - 10log_{10}(f_s/2) + 10log_{10}(N_{tones}) + Loss \tag{3.12}$$

Measured in dBc/Hz, Where N_{bits} is the equivalent number of bits (ENOB), f_s is the sampling rate, N_{tones} is the number of tones, and Loss is either some loss from the loop and/or crest factor reduction of the frequency comb. Figure 3.13 shows the

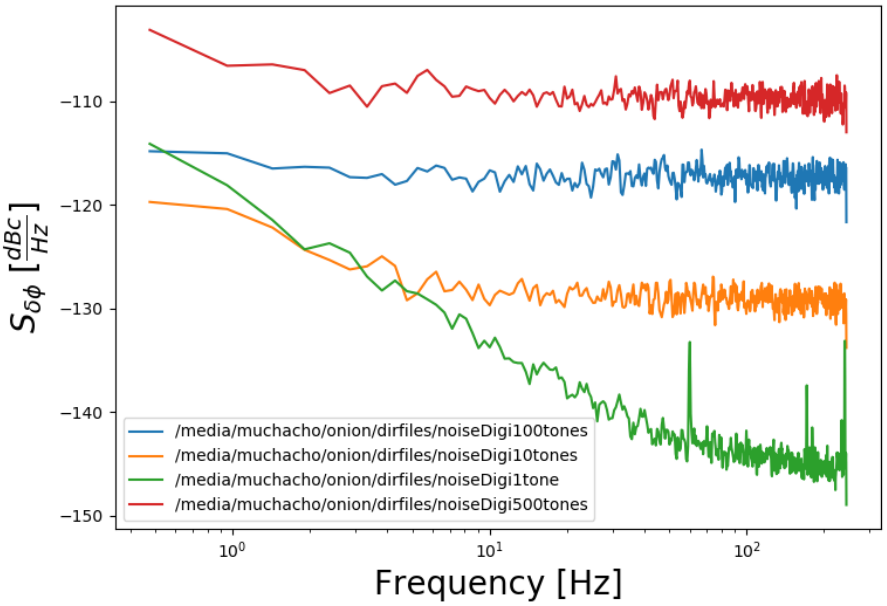

Figure 3.13: Loopback phase noise for a single channel as a function of the number of tones in the frequency comb.

effect of holding all else constant but the number of tones in the frequency comb and measuring the phase noise for a channel. Figure 3.14 shows the phase noise for 1000 channels on the RFSoC with the BLAST equivalent system. The equivalent number of bits are typically lower for ADCs and thus they dominate the loopback phase noise.

3.2.2 Measuring D/A Noise

The D/A which generates the frequency comb to bias the resonators also generates a noise floor. This floor is considered quantization noise and is related to the number of bits and full scale voltage of the digitizer. This noise is spread over the Nyquist bandwidth. Quantization noise is described in more detail in section 4.2.

A method to measure the D/A quantization noise floor and other spurious effects is to employ a microwave interferometer setup as shown in figure 3.15. This uses

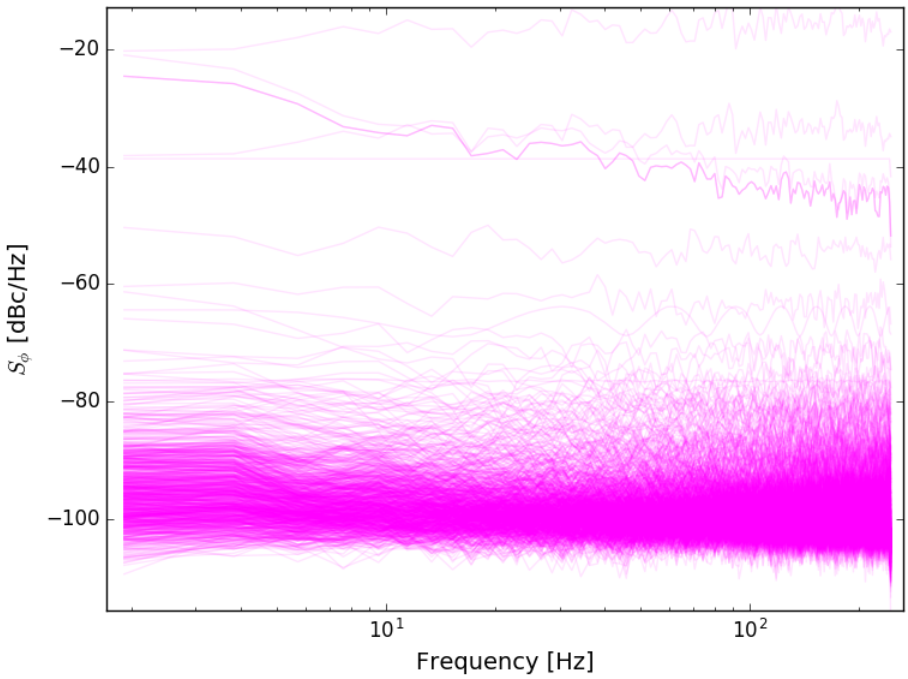

Figure 3.14: Loopback phase noise with the RFSoC for 1000 channels.

two power power splitters, two different length coaxial cables, an amplifier, and a spectrum analyzer or oscilloscope. A signal is generated by the D/A under test which is exactly matched in frequency such that the phase delay between the two different length cables is exactly 180 degrees. When the signal is recombined exactly out of phase the main tone is attenuated greatly in which the surrounding noise floor may be safely amplified without compression. The output of the amplifier from setup is measured by the spectrum analyzer and shown on the right in figure 3.15. The null in the spectrum corresponds to the tone that was attenuated and the signals outside of this are interpreted as D/A noise with an equivalent number of bits of 10 or less.

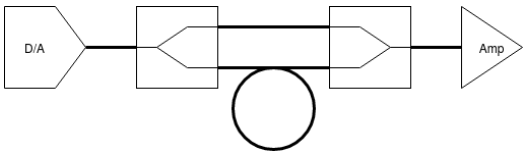

(a)

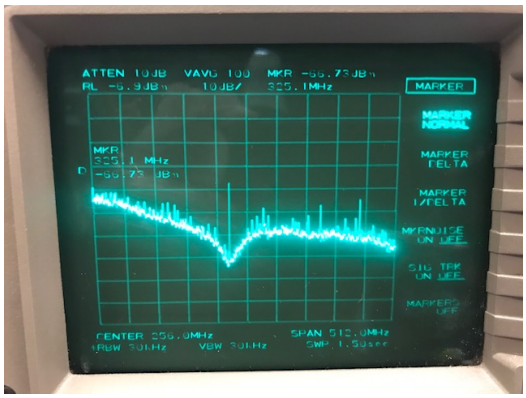

(b)

Figure 3.15: a) Microwave interferometer setup for measuring the D/A quantization noise floor. Consisting of a power splitter, two different length coaxial cables, a power combiner, and an amplifier. b) Spectrum analyzer measurement of the D/A noise at the output amplifier from the interferometer setup.

3.3 Path Forward

I have presented a first implementation of a frequency multiplexed detector readout on the RFSoC platform in the previous sections. As shown earlier in the chapter, the blast firmware under utilizes the available fabric resources, and thus has room to grow. There are different paths forward to increasing the resonator readout count each with their own advantages and disadvantages. These can be roughly split into two, many smaller bands or a few large bands. First I'll describe the path towards a design with multiple small bands.

Assuming IQ signaling, which gives access to both sidebands, the number of designs operating in parallel is limited to 4. To move past this, single sideband signaling can be used or the combination of oversampling and a digital mix. The packaged blast firmware can be copied and implemented in parallel up to 8 times each with 500 MHz of instantaneous bandwidth and up to 1024 channels. Thus per ZCU111 we could

have up to 8192 channels without any modification to the blast-dsp module. Another required task to realize parallel designs is to use the DDR4 memory for the frequency comb look up table. This will free up the logic resources for additional blast-dsp modules. A benefit to the many small bands design is that it maintains more dynamic range for the D/A. The downside is that more cryogenic RF chains are required which increases the heat load from coax and cryo amplifiers.

The number of detectors per octave of bandwidth is thought to stay roughly the same as what has been achieved by NIST for BLAST-TNG and TolTEC, this means that the number of channels per instantaneous bandwidth will have an acceptable maximum before the yield suffers from resonator collisions. This leads to the result that increasing the detector count requires and increase of instantaneous bandwidth of the digitizers. This also increases the number of parallel lines in the DSP modules affecting resource utilization. The path to large instantaneous bandwidth which truly realizes the capabilities of the RFSoC digitizers requires DSP development and a careful resource utilization study.

3.4 CORDIC MFSK Implementation

In this section I explore an alternative design in which the frequency multiplexed arrays are readout in a time multiplexed way. This was inspired originally by frequency shift keyed (FSK) digital modems. An incredible reduction in digital complexity is achieved with such a design. The dynamic range requirements of the digitizers and amplifiers would also become significantly relaxed as well. This is a time division multiplexed scheme and thus must be carefully analyzed in that under most circumstances they suffer a multiplexing noise penalty. I will start by giving an overview of an FSK modem and then go into the specific implementation. Initial measurements showing the tone switching and the successful demodulation are also presented. Lim-

itations of the design are discussed and another design is presented as a potential solution.

3.4.1 FSK Modem

An FSK modem uses multiple frequencies where each is a symbol which represents some bits. A two tone FSK system would have one frequency represent 0 and the other 1. The task is then to convert some information stream of bits into one of the two tones and transmit it long enough that it can be reliably received but short enough to give the highest data rate possible. Due to the finite switching time between frequencies the frequency domain representation of the symbols is a sinx/x with width equal to the symbol rate. In higher symbol count systems than two the bit rate B is related to the symbol rate R as $B = Rlog_2M$, where M is the number of symbols. The tone spacing is typically chosen such that when a correlation receiver is used the adjacent symbols are orthogonal when intergrated over a symbol period, meaning the adjacent symbols correlator output will be zero. An example of an FSK modem design is shown in figure 3.16.

3.4.2 CORDIC Based Implementation

Linear mode frequency multiplexed detectors typically only require readout bandwidths in the hundreds of Hz. Modern digitizers have significantly higher readout bandwidths by over four orders of magnitude, thus we can potentially get away with a time multiplexed readout. The main catch to this is the noise bandwidth discussed in a later section.

As an example if we have 1000 frequency multiplexed detectors that need a bandwidth of 100 Hz each then the switching rate required would be,

$$R = M \times S, \tag{3.13}$$

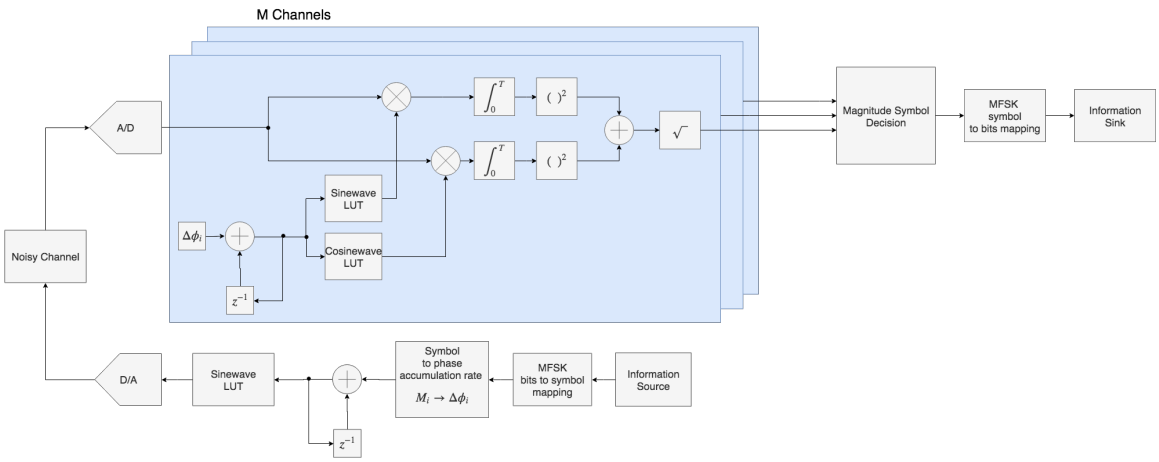

Figure 3.16: An example MFSK modem design showing the path from information source to information sink. A bitstream is mapped to symbols which correspond to a particular tone being generated for some period of time. The tones traverse a noisy channel on their way to the receiver. An array of correlators are used to determine which tone was received. A correlator consists of a multiplication of the tone and integration over a symbol period for which the tones are considered to be orthogonal. A comparator determines which symbol channel has the highest correlation and then uses a table to convert the symbol recieved to its corresponding bits.

Where R is the symbol rate in Hz, M is the number of symbols, and S is the science rate in Hz. This implies that we need to have an instantaneous sampling bandwidth of at least 100 kHz. Which can be accomplished with a digitizer sampling at 200 kHz and an anti-aliasing filter with a cutoff matched to 100 kHz. Any further sampling would be oversampling and could be averaged down to the bandwidth required.

Each detectors resonant frequency would be determined ahead of time then saved into a look up table to be used as the list of symbol frequencies. Each would be generated for the symbol period (1/R) in some order then repeated at the science rate. This method implies that only one tone is being generated by the D/A at any

given time. Thus the tone will have the maximum possible signal to noise available from the D/A. For multi-tone waveforms the signal to noise per tone is reduced due to the splitting of the available power between the tones. A single tone transmitted through the cryostat will also ease the dynamic range requirement on the cryogenic low noise amplifier. At the time of writing this the saturation power and non-linearity characterized by the P1dB and IP3 of cryogenic low noise amplifiers are nearing their limits given the power requirements of kilo-detector arrays. On the receive side the A/D must have at least a Nyquist bandwidth of R. The main operational difference between a typical FSK demodulator design and this readout is that we will know ahead of time the symbol entering the receiver. This means we only need one demodulator instead of M. The sky signal will modulate the resonant frequency of the detector and this would show up as a change in the downconverted symbols complex value.

Figure 3.17 shows the block diagram of an MFSK style detector readout. The design employs the use of the CORDIC algorithm for modulation and demodulation. CORDIC stands for COordinate Rotation DIgital Computer and was devised to calculate trigonometric functions efficiently, Volder (1959). The CORDIC algorithm can be used to generate complex sinusoids and even perform complex multiplication. Typically the CORDIC modules top level have three ports on the input and three on the output. These are the complex scaling factors X and Y and the phase Z. To generate a full scale complex sinusoid you can set the input scaling factors to static values, for example X=0 and Y=1, then provide a phase value to Z. After a linear delay the solutions $X = cosZ$, and $Y = sinZ$ are presented at the output. Thus to generate an oscillating signal in time the phase must be stepped by some increment ΔZ. A phase accumulator at the input to the Z port of the CORDIC supplies these phase steps and thus the angular frequency is determined by the clock rate and

phase increment, $\omega = \Delta Z/T_{clk}$. Each resonator i has a unique frequency which will correspond to some phase increment ΔZ_i. These are stored in a BRAM and stepped through at the science rate. An example of what this waveform would look like is shown on the top in figure 3.18.

On the receive side the incoming complex signal is demodulated with another CORDIC. Now however the incoming complex signals are sent to the complex scaling ports X and Y and the phase port is connected to the transmitter phase input but inverted by 180°. This performs a complex downconversion of the incoming signal to DC. To account for the linear delay between the input to the modulator CORDIC and the input to the demodulator CORDIC a tunable digital delay is used for the phase signal. This complex output can then be accumulated coherently and stored for later analysis.

Implementation and Measurements

The CORDIC design was compiled for the RFSoC ZCU111 board using a combination of custom VHDL and packaged system generator modules in Vivado 2018.3. The Xilinx CORDIC IP module was used for both the modulator and demodulator. A custom VHDL module which accomplishes the symbol switching was developed in GHDL and was interfaced with the phase accumulators and BRAM. A dual port BRAM is used to load the list of frequencies on the processor's 100 MHz AXI interface and to connect to the the symbol counter running at 256MHz on the other port.

Initial measurements of the symbol switching proved promising and looked almost exactly like what you would expect for an FSK modem, see figures 3.18. To confirm that the downconversion to DC is happening properly we used SNAP blocks in the firmware which can be read via PYNQ from the Jupyter-Notebook.

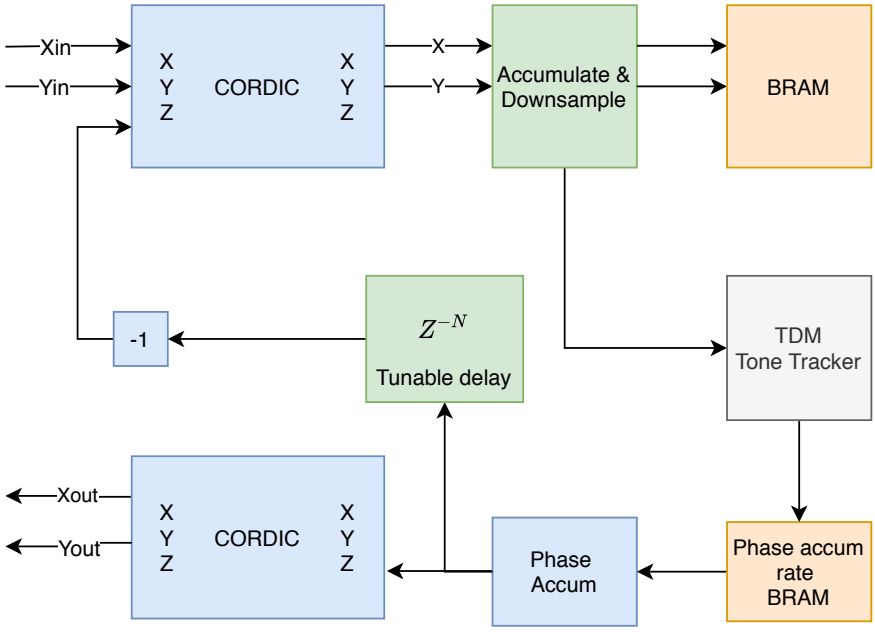

Figure 3.17: CORDIC MFSK block design.

3.4.3 FSK Homodyne

We have begun to explore an alternative readout architecture which retains the CORDIC frequency hopping but demodulates to DC outside of the FPGA. This design was inspired by the work of Sipola *et al.* (2019) in which a frequency shift keyed readout of over 100 frequency multiplexed detectors was presented. With the RFSoC's high speed digitizers it is feasible to generate the direct RF tones necessary to bias the resonators without the need for an additional external modulator. We can use this to our advantage to greatly simplify the digital demodulation. Instead of performing a digital downconversion to DC we can utilize an analog mixer to

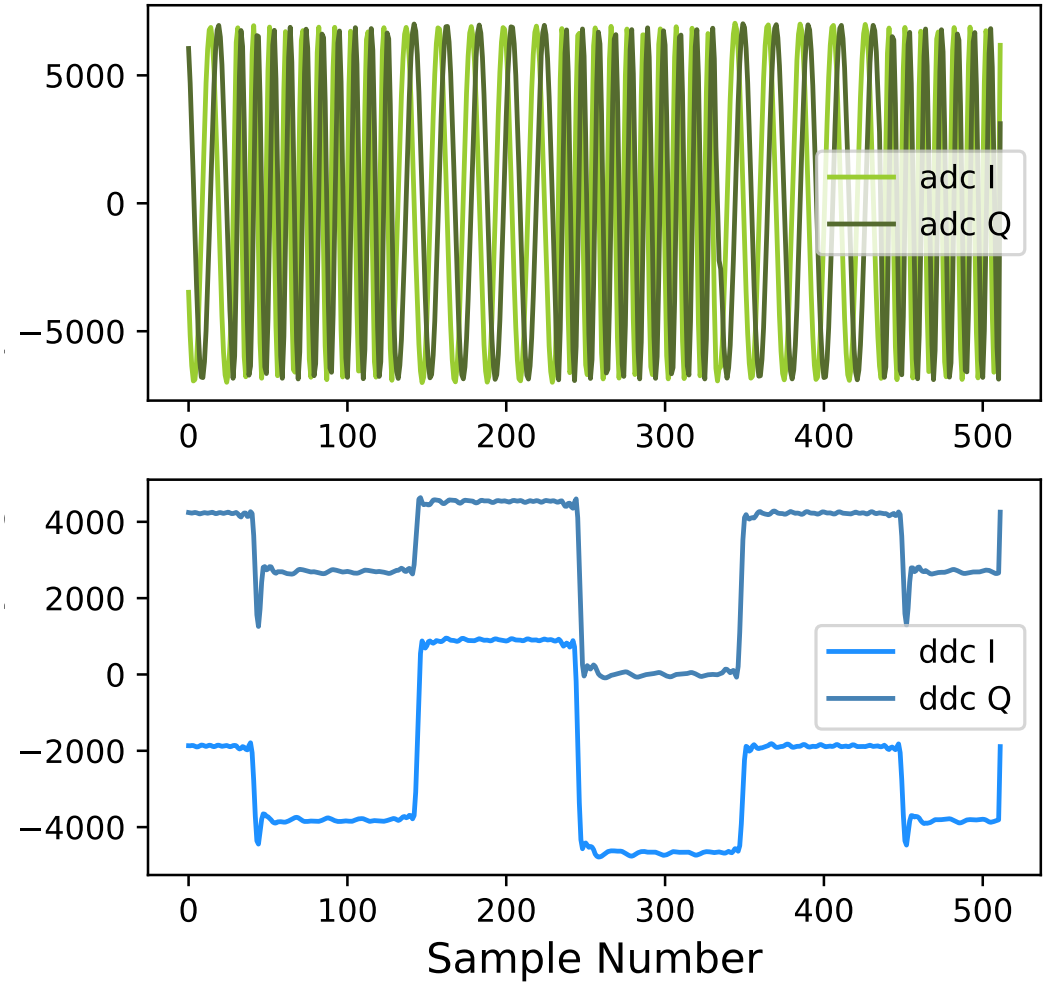

Figure 3.18: The top plot shows the in-phase (I) and quadrature (Q) timestreams captured by the ADC with the CORDIC MFSK design connected in loopback. The different frequency symbols are clearly seen switching at a period of about 100 samples. The plot below shows the output from the digital downconversion CORDIC where each symbol has been converted down to DC. The steps shows that the downconverted phase happens to be different for each symbol.

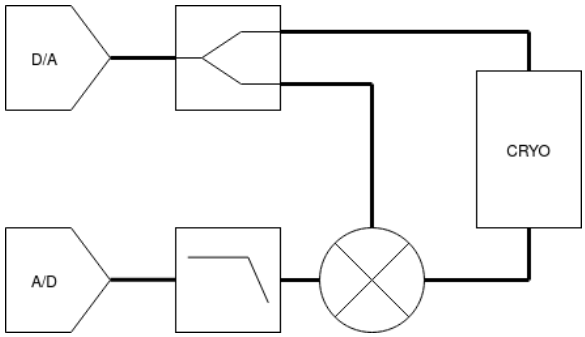

Figure 3.19: FSK homodyne setup showing the path from the D/A to the A/D. The FSK waveform is split with a power divider with one half being sent to through the cryostat and the other to the mixer. The downconverted output of the mixer is low pass filtered with a cutoff equal to or above the symbol rate.

downconvert before the A/D. The signal from the D/A is power split with one coaxial going to the cryostat and the other to the LO port of the downconverting mixer. The signal transmitted through the cryostat is mixed with the un-modified D/A signal effectively downconverting the signal as shown in figure 3.19. Thus only low speed digitizers are required to sample the I and Q outputs of the mixer.

An initial test was performed in which a ten tone FSK signal was generated. The symbol switching rate was approximately 600 kHz. The FSK waveform was measured by both an oscilloscope and spectrum analyzer, see figure 3.20. The downconverted output of the mixer was also captured by the oscilloscope. The discrete steps are representative of the different phases of each symbol after being converted to DC. Any change in the transmission through the cryostat will be measured by the down-converted symbols complex values.

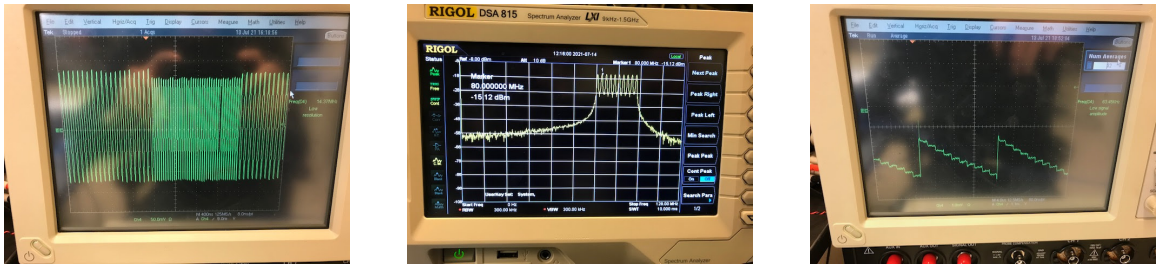

(a) (b) (c)

Figure 3.20: Oscilloscope and spectrum analyzer measurements of the FSK homodyne system. a) Directly measuring the 10 tone FSK waveform from the D/A. The symbol switching of approximately 2 us is easily observed. b) A spectrum analyzer measurement of 10 tones while switching. c) Downconverted timestream from the output of the mixer. Each step is a different symbol.

Chapter 4

READOUT LINK BUDGET

4.1 Noise Temperature

In the late 1920s two engineers, Johnson and Nyquist, described the voltage noise in conductors that we now call by their names. The rms voltage noise was shown to rely linearly on temperature and was given the intuitive explanation which relied on the equipartition theorem and the second law of thermodynamics.

In the Rayleigh-Jeans approximation the Johnson-Nyquist noise power is,

$$P = kT\Delta\nu. \tag{4.1}$$

This equation can be used to represent the equivalent RJ noise temperature of a component. As an example we can represent an amplifier as the combination of an ideal noiseless amplifier with a matched load at some equivalent temperature at it's input, figure 4.1.

Sometimes it is useful to calculate the output noise temperature of a system although it is less common. For instance the amplifier shown in figure 4.1 would have an output power of,

$$P_{out} = (kT_{load}\Delta\nu + kT\Delta\nu)G, \tag{4.2}$$

Assuming that the input to the amplifier is terminated with a matched load at temperature T_{load}. Both the input load noise and the equivalent noise temperature are multiplied by the amplifier gain. This is now divided by Boltzmann's constant and the bandwidth to find the equivalent **output** noise temperature,

$$T_{output} = \frac{P_{out}}{k\Delta\nu} = G(T_{load} + T). \tag{4.3}$$

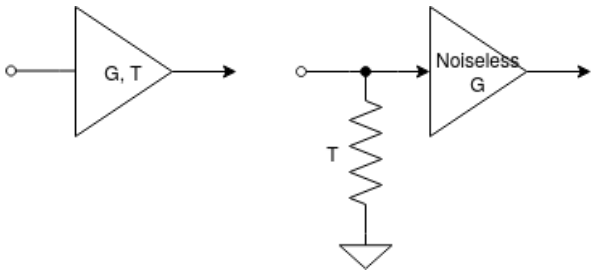

Figure 4.1: Equivalent noise temperature model of an amplifier. An amplifier with gain G and noise temperature T is equivalent shown on the left is equivalent to a noiseless amplifier with the same gain G with a matched load of temperature T at it's input.

In the case of a component with loss the equivalent noise temperature is determined by its physical temperature and the amount of loss,

$$T_{eq} = T_{phy}(L - 1), \tag{4.4}$$

Where the loss is just the inverse of the gain $L = 1/G$.

4.2 Quantization Noise

The effect of quantization in a digitizer produces a floor of spurious signals which can limit the dynamic range of a system. In the case of kinetic inductance detector readout the quantization noise can play a significant role and thus requires careful consideration when optimizing a system. First the well known 6 dB per bit signal to noise equation is derived then reformulated into forms which can be directly compared with other component contributions. These equations are used later on to complete the noise stack and provide predictions on total system noise.

When we convert a signal from bits in the digital domain to an analog voltage or vice versa we are representing a digital signal with some number of bits which are

then mapped to voltages. This means that the voltage step of a digitizer is the full scale voltage swing V_{FS} divided by $2^{N_{bits}}$,

$$\Delta V = \frac{V_{FS}}{2^{N_{bits}}} \quad [V]. \tag{4.5}$$

If a sinusoid is assumed then we can relate the rms voltage relation to full scale voltage as,

$$V_{rms} = \frac{V_0}{\sqrt{2}} = \frac{V_{FS}}{2\sqrt{2}}. \tag{4.6}$$

Where V_0 is the sinusoid amplitude.

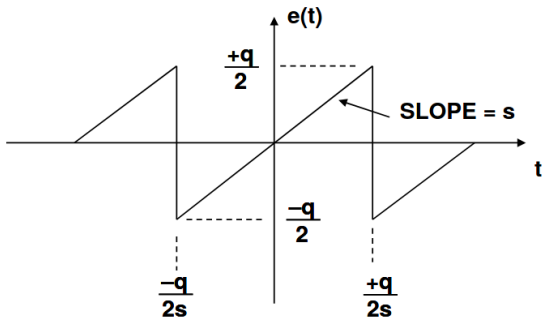

Figure 4.2: Quantization error $e(t)$ as a function of time for a voltage step $q(\Delta V)$. Figure from reference **?**

To estimate the quantization noise we start by defining and error term which is the actual signal minus the quantized version which ends up as a sawtooth pattern as shown in figure 4.4. Following the derivation of Kester (2009) the step error term is,

$$e(t) = st \tag{4.7}$$

Where s is the slope of error and t is time. We then can find the rms error over integrating over the domain $-\Delta V/2s < t < \Delta V/2s$,

$$\delta V_{rms} = \sqrt{\frac{\Delta V}{s}\int_{-\Delta V/2s}^{\Delta V/2s}(st)^2 dt} = \frac{\Delta V}{\sqrt{12}} = \frac{V_{FS}}{2^{N_{bits}}\sqrt{12}}. \tag{4.8}$$

This is the rms quantization noise in volts which is spread over the Nyquist bandwidth from DC to $f_s/2$.

We can now take the ratio of the rms voltage (eq. 4.6) to the rms quantization noise (eq. 4.8) squared to get the signal to noise,

$$SNR_{lin} = \left(\frac{V_{FS}}{2\sqrt{2}}\frac{2^{N_{bits}}\sqrt{12}}{V_{FS}}\right)^2 = \frac{3}{2}2^{2N_{bits}}. \tag{4.9}$$

We then convert this to dB to get the well known SNR equation,

$$SNR = 6.02N_{bits} + 1.76 \;\; [dB]. \tag{4.10}$$

Therefore we can see that for every bit we gain roughly 6 dB in signal to noise. It is important to mention that this is the signal to noise for a full scale sinusoid, the SNR would be lower if this was not the case. However the quantization noise floor would stay the same. Another useful metric is the noise spectral density (NSD), which we define as,

$$NSD = -SNR - 10log_{10}(f_s/2) \;\; [dBc/Hz], \tag{4.11}$$

Where f_s is the sampling frequency of the digitizer.

To compare this with other components in the signal chain we calculate the power in the quantization noise floor,

$$P_{digi} = \frac{\delta V_{rms}^2}{Z_0} = \frac{\Delta V^2}{12Z_0} = \frac{1}{12Z_0}\frac{V_{FS}^2}{2^{2N_{bits}}} \;\; [W]. \tag{4.12}$$

Where Z_0 is the characteristic impedance of the interface to the digitizer, typically 50 Ω in microwave circuits and 1 Ω in digital signal processing literature. The full scale sinusoidal output power of a digital to analog converter is,

$$P_{FS} = \frac{V_{rms}^2}{Z_0} = \frac{V_{FS}^2}{8Z_0}. \tag{4.13}$$

4.2.1 Quantization Noise Simulation

To demonstrate the effect of quantization and provide validity to the equations derived above we simulate the quantization of a sine wave. First assuming a three bit digitzer to exaggerate the effect we define a sine wave with an amplitude A of 3 quantized steps,

$$x(n) = Asin(2\pi n f_0/f_s) = 3sin(2\pi n f_0/f_s). \tag{4.14}$$

The sinusoid frequency f_0 is chosen such that it is not an exact multiple of the sampling frequency f_s. The reason for that is the noise spectrum will be highly correlated and the assumptions for equation 4.8 will no longer be valid. Figure 4.3 shows the exact sinusoid $x(n)$ along with the 3 bit quantized version $x_q(n)$. The quantization error is defined as the difference between the exact and quantized version,

$$Error(n) = x(n) - x_q(n). \tag{4.15}$$

The error waveform is plotted in figure 4.4 where it can be seen that it spans a single quantized step from -0.5 to +0.5. The quantization error of any arbitrary waveform is always within one quantization step. Therefore the noise power in this error is solely dependent on the number of bits and full scale amplitude of the digitizer. Other effects however such as non-linearities in the digitizer can contribute a noise like floor of spurs which does depend on the properties of the arbitrary waveform. These effects while important are not modeled in this section.

Using realistic specs for a digitizer, 10 bits and a 1.2V full scale voltage, we calculate the quantization error and plot the noise power spectral density using the Welch method. Assuming a 50 Ω characteristic impedance and neglecting any effects of impedance mismatches at the interface to the digitizer assuring that we are measuring all of the available power transfered to the load. Figure 4.5 shows that the simulated noise power of the quantized waveform error is around -140 dBm/Hz which

is close to the theoretical estimate of equation 4.12 given the digitizer parameters. For reference the theoretical estimate for the same full scale voltage but 11 bits and 12 bits are also shown. To also demonstrate the independence of this noise floor to the amplitude another simulated error is plotted where the sine wave amplitude has been divided by 10, while retaining the same number of bits and full scale voltage. So when considering quantization noise in the design of a frequency multiplexed system only the number of bits and full scale voltage need be considered. However to determine the signal to noise the number of tones needs to be considered.

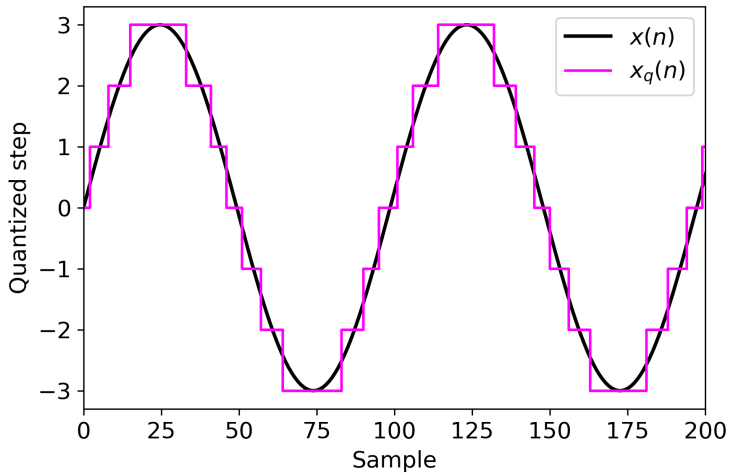

Figure 4.3: A discrete sine wave $x(n)$ of amplitude 3 along with a 3 bit quantized version $x_q(n)$ in units normalized to the quantization step ΔV(or q).

4.3 Cascaded Noise

Harald Friis, a Danish-American engineer, pioneered a way of evaluating the performance of a cascaded shortwave/microwave system. This method allows for an analysis of the signal to noise degradation at each stage through the chain and assigns a noise factor (or noise temperature) to each component. The noise factor is

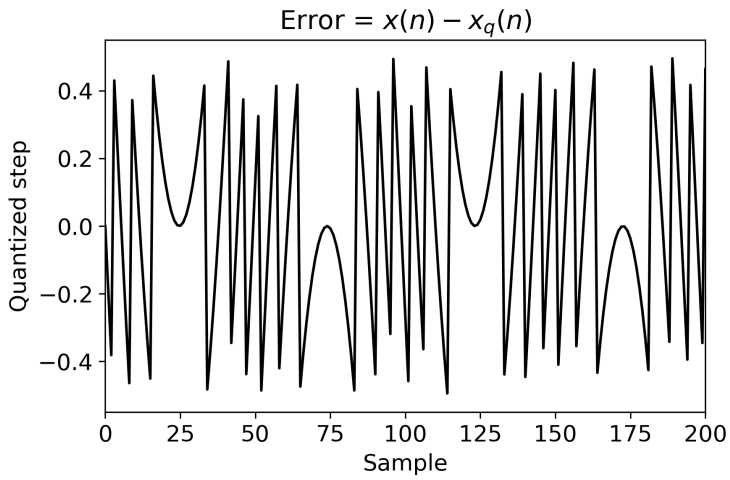

Figure 4.4: The quantization error defined as the difference between the exact sine wave minus the quantized sine wave, $Error(n) = x(n) - x_q(n)$. The y-axis shows that the error is always less than or equal to one quantization step.

defined as the ratio of the signal to noise into a component by the signal to noise out,

$$F = \frac{SNR_{in}}{SNR_{out}}. \tag{4.16}$$

We can model each component as having a gain G_i and output noise power N_i. This can be thought of as an ideal component with gain followed by a power combiner which adds noise as shown in figure 4.6.

Now if we have a chain of components as shown in figure 4.7 then the total noise factor would be,

$$F_{total} = \frac{SNR_{in}}{SNR_{out}} = \frac{S_{in}}{N_{in}} \frac{N_{in}G_1G_2G_3 + N_1G_2G_3 + N_2G_3 + N_3}{S_{in}G_1G_2G_3} \tag{4.17}$$

$$= 1 + \frac{N_1}{N_{in}G_1} + \frac{N_2}{N_{in}G_1G_2} + \frac{N_3}{N_{in}G_1G_2G_3} \tag{4.18}$$

$$= F_1 + \frac{F_2 - 1}{G_1} + \frac{F_3 - 1}{G_1G_2}. \tag{4.19}$$

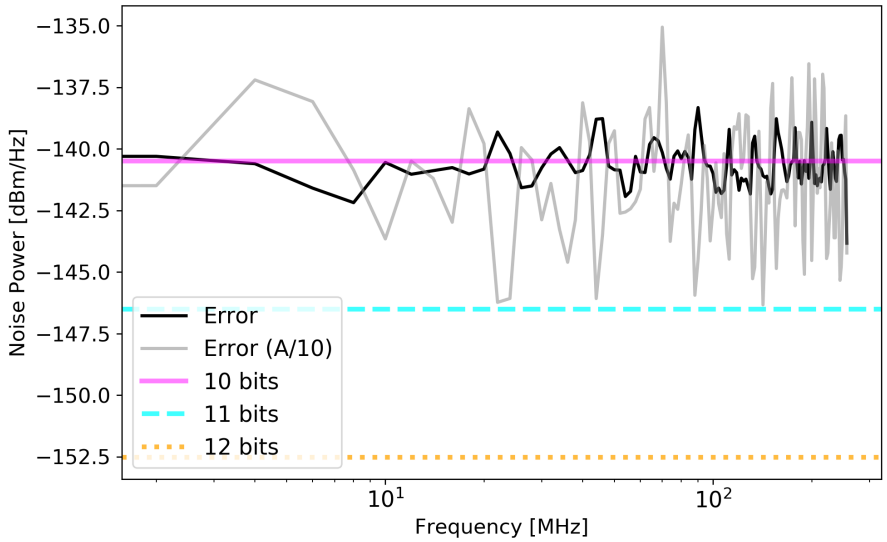

Figure 4.5: The simulated quantization noise power spectral density of a discrete sine wave assuming a 10 bit digitizer with a full scale voltage of 1.2 V. A second line in grey shows the same waveform with the amplitude reduced by a factor of 10. Horizontal lines represent the theoretical estimates provided by equation 4.12 using a full scale voltage of 1.2 V and 10, 11, and 12 bits.

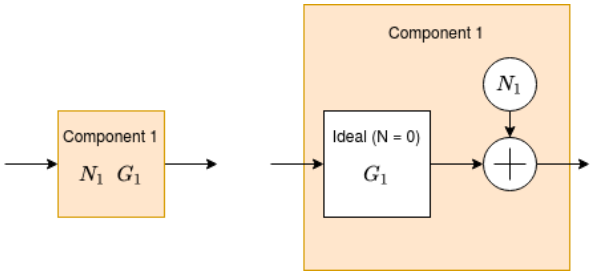

Figure 4.6: Equivalent model for the noise factor of a component with gain G_1 and output noise power N_1.

Where it can be easily seen that if this was a chain of amplifiers it is critical to have a low noise first stage with as high a gain as possible. The following stages contributions to the total noise factor are divided by the preceding stages gain.

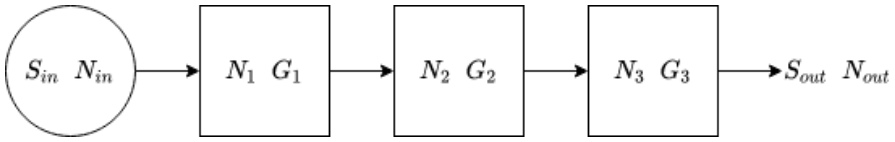

Figure 4.7: Example chain of three components each characterized by their gain and noise.

Commercial components typically report the noise figure NF which is the noise factor in dB,

$$NF = 10log_{10}(F) \quad [dB]. \tag{4.20}$$

Just as with noise factors we can characterize a cascade of components given their equivalent noise temperatures and gains. An important difference is that the equivalent noise temperature is referenced to the input of the component before any gain (or loss). This is related to the noise factor by,

$$F = 1 + T_{eq}/T_0 \tag{4.21}$$

Where T_0 is the reference temperature of 290 K. T_{eq} is for most cases the equivalent noise temperature in the Rayleigh-Jeans limit and neglecting the half photon of the quantum vacuum ($h\nu/2k$). As a worked example we can chain three components together, an amplifier, attenuator, and a second amplifier as shown in figure 4.8 and calculate the chains equivalent noise temperature,

$$T_{eq} = T_1 + \frac{T_2}{G_1} + \frac{T_3}{G_1 G_2} \tag{4.22}$$

For the lossy component the noise temperature is a function of its loss ($L = 1/G$) and physical temperature. Rewriting the above equation accounting for this we get,

$$T_{eq} = T_1 + \frac{T_{phy}(L_2 - 1)}{G_1} + \frac{T_3 L_2}{G_1}. \tag{4.23}$$

A few things to note in this equation, firstly the gain of the first stage amplifier divides down the contributions of the rest of the chain, providing the motivation for low noise and high gain amplifiers. Second, the lossy component in the middle of the chain which reduces the signal to noise of the system which shows up as an increased noise temperature contribution. The physical temperature of the loss is a significant contributor and motivates cryogenic loss if required. This loss also shows up as a multiplier to the noise temperature of the following components as shown in the third term as L_2. The entire three component chain is equivalent to a single component of gain $G_1G_2G_3$ and input referred noise temperature of T_{eq}.

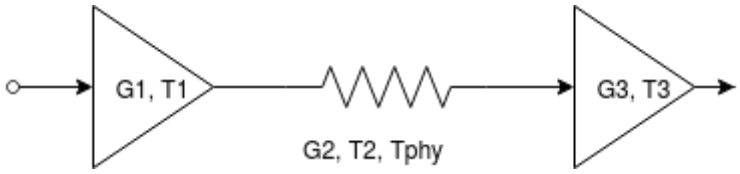

Figure 4.8: Example chain of three components each characterized by their gain and noise temperature, an amplifier with gain G1 and noise temperature T1, an attenuator with gain G2, noise temperature T2 and physical temperature Tphy, and finally another amplifier of gain G3 and noise temperature T3.

4.4 Coaxial Cable Attenuation

Coaxial cables carry the stimulus signals from room temperature through the sub-Kelvin cryostat and back out. Many cryostats will use multiple stages to distribute the heat load, where each stage is typically spanned by a coaxial cable. These cables

are microwave transmission lines which have a frequency and temperature dependent loss. The material and geometry of the cable are used to estimate the conductivity per unit length. Figure 4.9 shows the three main sections, center conductor, dielectric, and outer conductor. In order to reduce the heat load on each stage it is desirable to have low thermal conductivity but unfortunately this is also broadly proportional to the electrical conductivity. The empirically determined Wiedemann-Franz law states that the ratio of the thermal conductivity to electrical for a metal is constant for most temperature ranges,

$$\frac{\kappa}{\sigma} = LT, \tag{4.24}$$

where $L \approx 2.44 \times 10^{-8} \ \ W\Omega K^{-2}$ is the Lorenz number. While the law has general

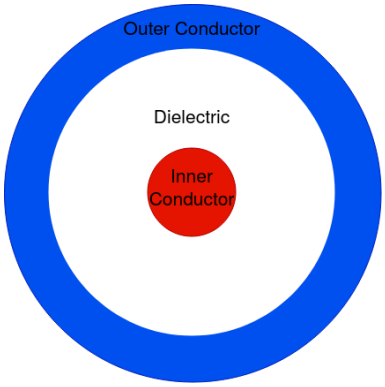

Figure 4.9: Cross section of a coaxial cable with the three main parts labeled, the center conductor, the dielectric, and the outer conductor. Commonly used materials for the conductors include stainless steel, beryllium-copper, copper-nickel, Niobium-Titanium, and the dielectric is usually polytetrafluoroethylene (PTFE).

applicability the thermal conductivity and electrical conductivity must typically be measured. An example of this is shown in figure 4.10 where the resistivity (inverse of electrical conductivity) determined by applying the WF law from thermal conductivity measurements predicts an uptick at low temperatures. The measured resistivity

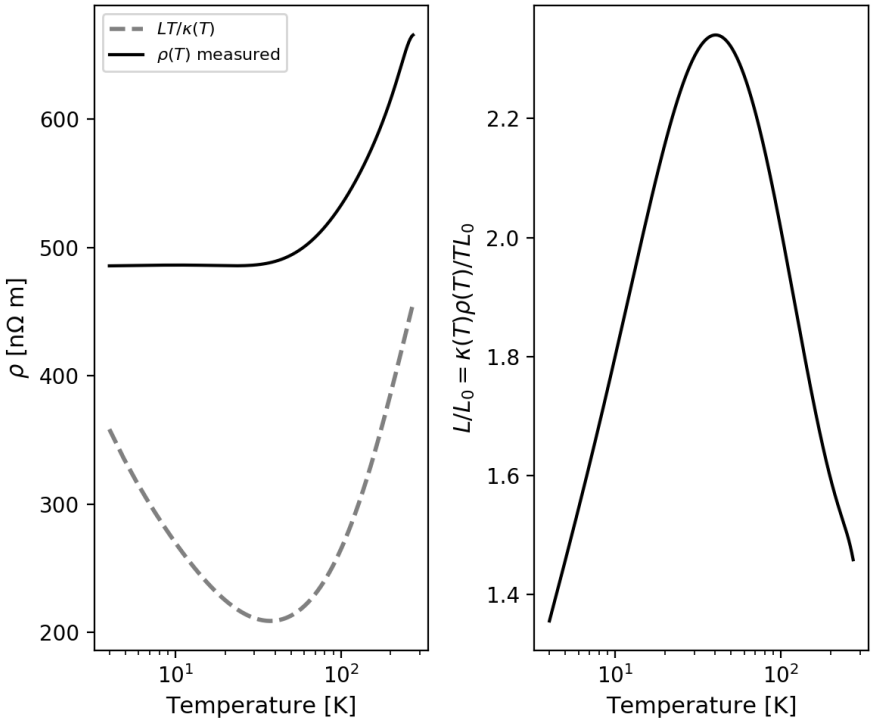

Figure 4.10: Stainless steel resistivity and the Lorenz ratio. The grey dashed curve was calculated by applying the WF law using the measured thermal conductivity, the black solid curve is the actual measured resistivity. The ratio of the two provides a factor by which the Lorenz number varies as a function of temperature.

clearly shows that the resistivity levels off to a constant value below 40K. Taking the ratio of the expected to measured we get the Lorenz correction factor as a function of temperature.

The distributors of SMA coax often provide loss tables measured for various frequencies and temperatures. The loss per meter as a function of frequency at a specific temperature can be fit to the following equation,

$$L = A\sqrt{f}. \tag{4.25}$$

Where f is the frequency and A is the constant extracted from the fit for the given

temperature. Given loss curves at two different temperatures a linear fit can be made for intermediate temperatures at a given frequency. These curves are plotted in figure 4.11 for a commonly used SMA cable from coax-co ? the (SC-219/50-SS-SS) stainless steel outer and inner conductor with a 2.19 mm outer diameter.

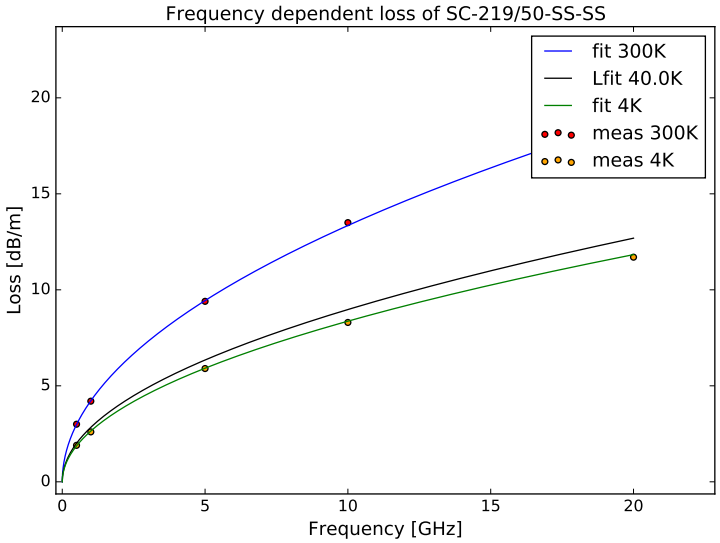

Figure 4.11: Coaxial cable loss per meter as a function of frequency and temperature. The dots in red and yellow are measured values provided by the manufacturer at 300K and 4K respectively. The fits are used to estimate the loss at any frequency and intermediate temperature. An estimate for the loss at the intermediate value of 40K is shown in black.

4.5 Cryogenic Link Budget

The above topics are combined to create a cryogenic link budget for various systems. The link budget can be used to investigate the relative contributions of each component in the chain and thus inform the design and help to optimize or debug. Figure 4.12 show the cryogenic RF chain for one of the BLAST-TNG 250um arrays

centered at 800 MHz.

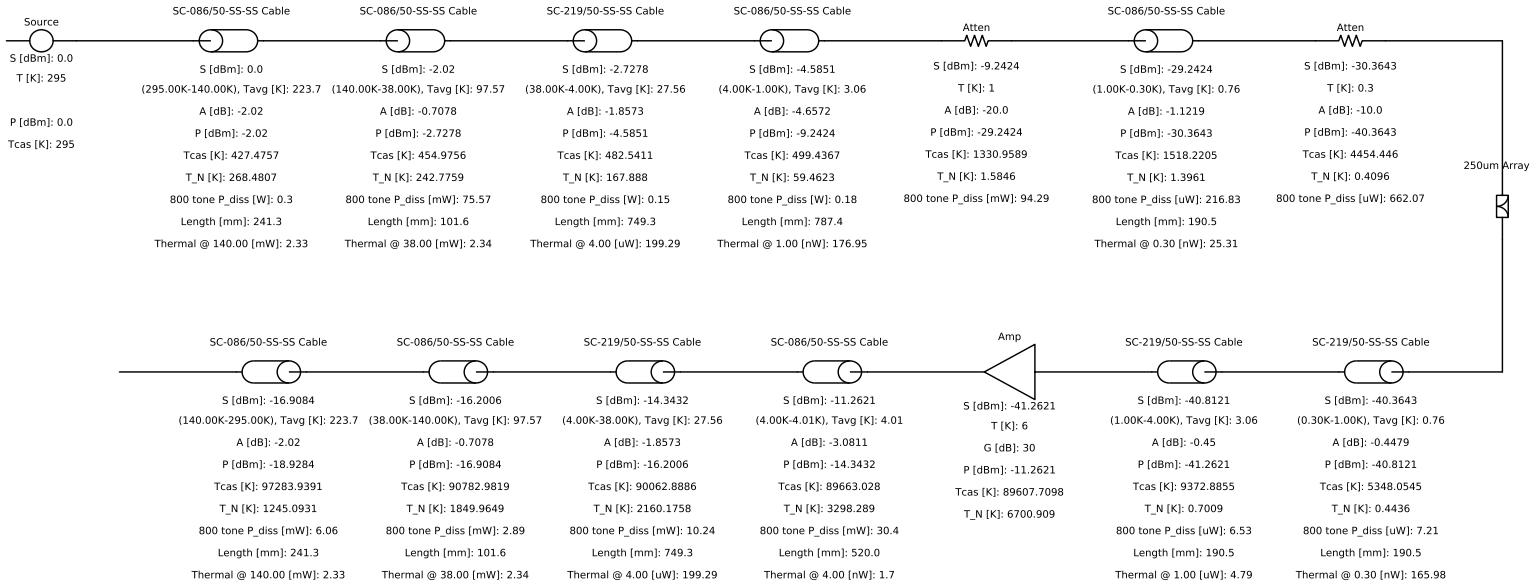

Figure 4.12: BLAST-TNG cryogenic RF chain model at a center frequency of 800MHz. S is the power into the component, T is the physical temperature (or noise temp for amplifier component), P is the power out of the component, A is the attenuation, T_{cas} is the cascaded noise temperature referenced to the components input, T_N is the noise temperature at the output, P_{diss} is the tone power dissipation, Length is the physical length of the cable section when bridging between two temperatures, Thermal is the thermal loading from the cable.

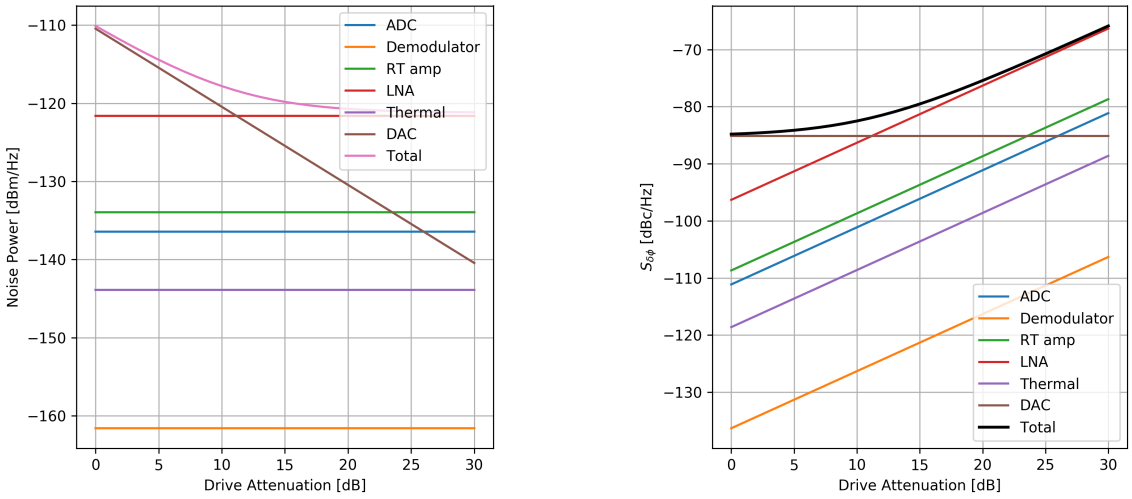

(a) (b)

Figure 4.13: a) Noise power in dBm vs drive attenuation from the D/A to the A/D. b) Phase noise vs drive attenuation from the D/A to the A/D. Each line represents the noise from that component as measured at the A/D.

4.6 Noise Stack

The cryogenic link budget can be combined with the warm electronics to give an entire noise stack-up from D/A to A/D. This can be used to understand the different components contribution to the total and which dominates. It can also be used to investigate the noise dependency on different parameters such as drive attenuation as shown in figure 4.13.

Zynq Ultrascale+ RFSoC Data Sheet: Overview, Xilinx, v1.10 (2020).

Akerib, D., X. Bai, S. Bedikian *et al.*, "Data acquisition and readout system for the lux dark matter experiment", Nuclear Instruments and Methods in Physics Research Section A: Accelerators, Spectrometers, Detectors and Associated Equipment **668**, 1–8 (2012).

Allmaras, J. P., E. E. Wollman, A. D. Beyer, R. M. Briggs, B. A. Korzh, B. Bumble and M. D. Shaw, "Demonstration of a thermally coupled row-column snspd imaging array", Nano letters **20**, 3, 2163–2168 (2020).

Barry, P., *On the development of SuperSpec: a fully integrated on-chip spectrometer for far-infrared astronomy*, Ph.D. thesis (2014).

Bender, A. N., J.-F. Cliche, T. de Haan, M. A. Dobbs *et al.*, "Digital frequency domain multiplexing readout electronics for the next generation of millimeter telescopes", in "Millimeter, Submillimeter, and Far-Infrared Detectors and Instrumentation for Astronomy VII", vol. 9153, p. 91531A (International Society for Optics and Photonics, 2014).

Bennett, W. R., "Spectra of quantized signals", The Bell System Technical Journal **27**, 3, 446–472 (1948).

Bourrion, O., A. Benoit, J. Bouly, J. Bouvier *et al.*, "Nikel_amc: Readout electronics for the nika2 experiment", Journal of Instrumentation **11**, 11, P11001 (2016).

Bueno, J., P. C. J. J. Coumou, G. Zheng, P. J. de Visser, T. M. Klapwijk, E. F. C. Driessen, S. Doyle and J. J. A. Baselmans, "Anomalous response of superconducting titanium nitride resonators to terahertz radiation", Applied Physics Letters **105**, 19, 192601, URL `https://doi.org/10.1063/1.4901536` (2014).

Catalano, A., M. Calvo, N. Ponthieu, R. Adam, A. Adane, P. Ade, P. André, A. Beelen, B. Belier, A. Benoît, A. Bideaud, N. Billot, N. Boudou, O. Bourrion, G. Coiffard, B. Comis, A. D'Addabbo, F. X. Désert, S. Doyle, J. Goupy, C. Kramer, S. Leclercq, J. F. Macías-Pérez, J. Martino, P. Mauskopf, F. Mayet, A. Monfardini, F. Pajot, E. Pascale, L. Perotto, V. Revéret, L. Rodriguez, G. Savini, K. Schuster, A. Sievers, C. Tucker and R. Zylka, "Performance and calibration of the NIKA camera at the IRAM 30 m telescope", Astronomy and Astrophysics **569**, A9 (2014).

Crutcher, R. M. and A. J. Kemball, "Review of zeeman effect observations of regions of star formation", Frontiers in Astronomy and Space Sciences **6**, 66, URL `https://www.frontiersin.org/article/10.3389/fspas.2019.00066` (2019).

Day, P. K., H. G. LeDuc, B. A. Mazin, A. Vayonakis and J. Zmuidzinas, "A broadband superconducting detector suitable for use in large arrays", Nature **425**, 6960, 817–821 (2003).

den Hartog, R., J. Beyer, D. Boersma *et al.*, "Frequency domain multiplexed readout of tes detector arrays with baseband feedback", IEEE transactions on applied superconductivity **21**, 3, 289–293 (2011).

Devlin, M. J., P. A. R. Ade, I. Aretxaga, J. J. Bock, E. L. Chapin, M. Griffin, J. O. Gundersen, M. Halpern, P. C. Hargrave, D. H. Hughes, J. Klein, G. Marsden, P. G. Martin, P. Mauskopf, L. Moncelsi, C. B. Netterfield, H. Ngo, L. Olmi, E. Pascale, G. Patanchon, M. Rex, D. Scott, C. Semisch, N. Thomas, M. D. P. Truch, C. Tucker, G. S. Tucker, M. P. Viero and D. V. Wiebe, "Over half of the far-infrared background light comes from galaxies at z¿=1.2", Nature **458**, 7239, 737–739 (2009).

Dicke, R. H., R. Beringer, R. L. Kyhl and A. B. Vane, "Atmospheric absorption measurements with a microwave radiometer", Phys. Rev. **70**, 340–348, URL `https://link.aps.org/doi/10.1103/PhysRev.70.340` (1946).

Doerner, S., A. Kuzmin, S. Wuensch, I. Charaev, F. Boes, T. Zwick and M. Siegel, "Frequency-multiplexed bias and readout of a 16-pixel superconducting nanowire single-photon detector array", Applied Physics Letters **111**, 3, 032603 (2017).

Dolginov, A. Z. and I. G. Mitrofanov, "Orientation of Cosmic Dust Grains", Astrophysics and Space Science **43**, 2, 291–317 (1976).

Doyle, S., J. Naylon, P. Mauskopf, A. Porch and C. Dunscombe, "Lumped Element Kinetic Inductance Detectors", in "Eighteenth International Symposium on Space Terahertz Technology", edited by A. Karpov, p. 170 (2007).

Draine, B. T. and J. C. Weingartner, "Radiative Torques on Interstellar Grains. II. Grain Alignment", The Astrophysical Journal **480**, 2, 633–646 (1997).

Echternach, P., B. Pepper, T. Reck and C. Bradford, "Single photon detection of 1.5 thz radiation with the quantum capacitance detector", Nature Astronomy **2**, 1, 90–97 (2018).

Evans, K. F., S. J. Walter, A. J. Heymsfield and M. N. Deeter, "Modeling of Submillimeter Passive Remote Sensing of Cirrus Clouds.", Journal of Applied Meteorology **37**, 2, 184–205 (1998).

Fissel, L. M., P. A. R. Ade, F. E. Angilè, P. Ashton, S. J. Benton, M. J. Devlin, B. Dober, Y. Fukui, N. Galitzki, N. N. Gandilo, J. Klein, A. L. Korotkov, Z.-Y. Li, P. G. Martin, T. G. Matthews, L. Moncelsi, F. Nakamura, C. B. Netterfield, G. Novak, E. Pascale, F. Poidevin, F. P. Santos, G. Savini, D. Scott, J. A. Shariff, J. Diego Soler, N. E. Thomas, C. E. Tucker, G. S. Tucker and D. Ward-Thompson, "Balloon-Borne Submillimeter Polarimetry of the Vela C Molecular Cloud: Systematic Dependence of Polarization Fraction on Column Density and Local Polarization-Angle Dispersion", The Astrophysical Journal **824**, 2, 134 (2016).

Fissel, L. M., P. A. R. Ade, F. E. Angilè, S. J. Benton, E. L. Chapin, M. J. Devlin, N. N. Gandilo, J. O. Gundersen, P. C. Hargrave, D. H. Hughes, J. Klein, A. L. Korotkov, G. Marsden, T. G. Matthews, L. Moncelsi, T. K. Mroczkowski, C. B. Netterfield, G. Novak, L. Olmi, E. Pascale, G. Savini, D. Scott, J. A. Shariff, J. D. Soler,

N. E. Thomas, M. D. P. Truch, C. E. Tucker, G. S. Tucker, D. Ward-Thompson and D. V. Wiebe, "The balloon-borne large-aperture submillimeter telescope for polarimetry: BLAST-Pol", in "Millimeter, Submillimeter, and Far-Infrared Detectors and Instrumentation for Astronomy V", edited by W. S. Holland and J. Zmuidzinas, vol. 7741 of *Society of Photo-Optical Instrumentation Engineers (SPIE) Conference Series*, p. 77410E (2010).

Gao, J., M. R. Vissers, M. O. Sandberg, F. C. S. da Silva, S. W. Nam, D. P. Pappas, D. S. Wisbey, E. C. Langman, S. R. Meeker, B. A. Mazin, H. G. Leduc, J. Zmuidzinas and K. D. Irwin, "A titanium-nitride near-infrared kinetic inductance photon-counting detector and its anomalous electrodynamics", Applied Physics Letters **101**, 14, 142602, URL `https://doi.org/10.1063/1.4756916` (2012).

Gordon, S., *Highly Multiplexed Superconducting Detectors and Readout Electronics for Balloon-borne and Ground-based Far-infrared Imaging and Polarimetry*, Ph.D. thesis, Arizona State University (2019).

Gordon, S., B. Dober, A. Sinclair, S. Rowe, S. Bryan, P. Mauskopf, J. Austermann, M. Devlin, S. Dicker, J. Gao, G. C. Hilton, J. Hubmayr, G. Jones, J. Klein, N. P. Lourie, C. McKenney, F. Nati, J. D. Soler, M. Strader and M. Vissers, "An Open Source, FPGA-Based LeKID Readout for BLAST-TNG: Pre-Flight Results", Journal of Astronomical Instrumentation **5**, 4, 1641003 (2016).

Gordon, S., B. Dober, A. Sinclair *et al.*, "An open source, fpga-based lekid readout for blast-tng: Pre-flight results", Journal of Astronomical Instrumentation **5**, 04, 1641003 (2016).

Henderson, S. W., Z. Ahmed *et al.*, "Highly-multiplexed microwave squid readout using the slac microresonator radio frequency (smurf) electronics for future cmb and sub-millimeter surveys", in "Millimeter, Submillimeter, and Far-Infrared Detectors and Instrumentation for Astronomy IX", vol. 10708, p. 1070819 (International Society for Optics and Photonics, 2018).

Henderson, S. W., J. R. Stevens, M. Amiri *et al.*, "Readout of two-kilopixel transition-edge sensor arrays for advanced actpol", in "Millimeter, Submillimeter, and Far-Infrared Detectors and Instrumentation for Astronomy VIII", vol. 9914, p. 99141G (International Society for Optics and Photonics, 2016).

Hotta, M., M. Hayashi, M. T. Lanagan, D. K. Agrawal and K. Nagata, "Complex permittivity of graphite, carbon black and coal powders in the ranges of x-band frequencies (8.2 to 12.4 ghz) and between 1 and 10 ghz", ISIJ International **51**, 11, 1766–1772 (2011).

Hubmayr, J., J. Beall, D. Becker, H. M. Cho, M. Devlin, B. Dober, C. Groppi, G. C. Hilton, K. D. Irwin, D. Li, P. Mauskopf, D. P. Pappas, J. Van Lanen, M. R. Vissers, Y. Wang, L. F. Wei and J. Gao, "Photon-noise limited sensitivity in titanium nitride kinetic inductance detectors", Applied Physics Letters **106**, 7, 073505 (2015).

Hubmayr, J., J. A. Beall, D. Becker, J. A. Brevik, H. M. Cho, G. Che, M. Devlin, B. Dober, J. Gao, N. Galitzki, G. C. Hilton, K. D. Irwin, D. Li, P. Mauskopf,

D. P. Pappas, J. Van Lanen and M. R. Vissers, "Dual-Polarization-Sensitive Kinetic Inductance Detectors for Balloon-borne Sub-millimeter Polarimetry", Journal of Low Temperature Physics **176**, 3-4, 490–496 (2014).

Jackson, B., P. De Korte, J. Van der Kuur, P. Mauskopf *et al.*, "The spica-safari detector system: Tes detector arrays with frequency-division multiplexed squid readout", IEEE Transactions on Terahertz Science and Technology **2**, 1, 12–21 (2011).

Kernasovskiy, S., S. Kuenstner, E. Karpel *et al.*, "Slac microresonator radio frequency (smurf) electronics for read out of frequency-division-multiplexed cryogenic sensors", Journal of Low Temperature Physics **193**, 3-4, 570–577 (2018).

Kester, W., "Mt-001 tutorial taking the mystery out of the infamous formula , " snr = 6 . 02 n + 1 . 76 db , " and why you should care by", (2009).

Krumholz, M. R. and C. Federrath, "The role of magnetic fields in setting the star formation rate and the initial mass function", Frontiers in Astronomy and Space Sciences **6**, 7, URL `https://www.frontiersin.org/article/10.3389/fspas.2019.00007` (2019).

Krumholz, M. R. and J. C. Tan, "Slow Star Formation in Dense Gas: Evidence and Implications", The Astrophysical Journal **654**, 1, 304–315 (2007).

Lambert, A., W. Read and N. Livesey, "Mls/aura level 2 water vapor (h2o) mixing ratio v004", (2015).

Lazarian, A. and T. Hoang, "Magnetic properties of dust grains, effect of precession, and radiative torque alignment", The Astrophysical Journal **883**, 2, 122 (2019).

Maloney, P. R., N. G. Czakon, P. K. Day *et al.*, "Music for sub/millimeter astrophysics", in "Millimeter, Submillimeter, and Far-Infrared Detectors and Instrumentation for Astronomy V", vol. 7741, p. 77410F (International Society for Optics and Photonics, 2010).

Mauskopf, P. D., "Transition edge sensors and kinetic inductance detectors in astronomical instruments", Publications of the Astronomical Society of the Pacific **130**, 990, 082001, URL `https://doi.org/10.1088/1538-3873/aabaf0` (2018).

Mazin, B., S. R. Meeker, M. Strader *et al.*, "Arcons: A 2024 pixel optical through near-ir cryogenic imaging spectrophotometer", **125**, 933, 1348 (2013).

McHugh, S., B. A. Mazin, B. Serfass, S. Meeker, K. O'Brien, R. Duan, R. Raffanti and D. Werthimer, "A readout for large arrays of microwave kinetic inductance detectors", Review of Scientific Instruments **83**, 4, 044702–044702 (2012).

Minutolo, L., B. Steinbach, A. Wandui and R. O'Brient, "A flexible gpu-accelerated radio-frequency readout for superconducting detectors", IEEE Transactions on Applied Superconductivity **29**, 5, 1–5 (2019).

Moisés, A. P., A. Damineli, E. Figuerêdo, R. D. Blum, P. S. Conti and C. L. Barbosa, "Spectrophotometric distances to galactic h ii regions", Mon. Not. R. Astron. Soc. **411**, 2, 705–760 (2011).

Paiella, A., E. Battistelli, M. Castellano *et al.*, "Kinetic inductance detectors and readout electronics for the olimpo experiment", in "Journal of Physics: Conference Series", vol. 1182, p. 012005 (IOP Publishing, 2019).

Paiella, A. *et al.*, "In-Flight Performance of the LEKIDs of the OLIMPO Experiment", J. Low Temp. Phys. **199**, 1-2, 491–501 (2020).

Paine, S., "The am atmospheric model", URL `https://doi.org/10.5281/zenodo.3406496` (2019).

Pattle, K., D. Ward-Thompson, T. Hasegawa, P. Bastien, W. Kwon, S.-P. Lai, K. Qiu, R. Furuya and D. B. and, "First observations of the magnetic field inside the pillars of creation: Results from the BISTRO survey", **860**, 1, L6, URL `https://doi.org/10.3847/2041-8213/aac771` (2018).

Peterson, D., M. Fromm and R. e. a. McRae, "Australias black summer pyrocumulonimbus super outbreak reveals potential for increasingly extreme stratospheric smoke events", npj Clim Atmos Sci **4**, URL `https://doi.org/10.1038/s41612-021-00192-9` (2021).

Rodgers, A. W., C. T. Campbell and J. B. Whiteoak, " A Catalogue of H -Emission Regions in the Southern Milky Way ", Monthly Notices of the Royal Astronomical Society **121**, 1, 103–110, URL `https://doi.org/10.1093/mnras/121.1.103` (1960).

Santos, F. P., D. T. Chuss, C. D. Dowell, M. Houde, L. W. Looney, E. L. Rodriguez, G. Novak, D. Ward-Thompson, M. Berthoud, D. A. Dale, J. A. Guerra, R. T. Hamilton, S. Hanany, D. A. Harper, T. K. Henning, T. J. Jones, A. Lazarian, J. M. Michail, M. R. Morris, J. Staguhn, I. W. Stephens, K. Tassis, C. Q. Trinh, E. V. Camp, C. G. Volpert and E. J. Wollack, "The far-infrared polarization spectrum of ρ ophiuchi a from HAWC+/SOFIA observations", The Astrophysical Journal **882**, 2, 113 (2019).

Schwartz, M., M. Santee, H. Pumphrey, G. Manney, A. Lambert, N. Livesey, L. Milln, J. Neu, W. Read and F. Werner, "Australian new year's pyrocb impact on stratospheric composition", Geophysical Research Letters **47** (2020).

Sinclair, A. K., E. Schroeder, D. Zhu, M. Colangelo, J. Glasby, P. D. Mauskopf, H. Mani and K. K. Berggren, "Demonstration of microwave multiplexed readout of dc-biased superconducting nanowire detectors", IEEE Transactions on Applied Superconductivity **29**, 5, 1–4 (2019).

Sipola, H., J. Luomahaara, A. Timofeev, L. Grönberg, A. Rautiainen, A. Luukanen and J. Hassel, "Multiplexed readout of kinetic inductance bolometer arrays", Review of Scientific Instruments **90**, 7, 074702 (2019).

Volder, J. E., "The cordic trigonometric computing technique", IRE Transactions on Electronic Computers **EC-8**, 3, 330–334 (1959).

Waters, J., L. Froidevaux, R. Harwood, R. Jarnot, H. Pickett, W. Read, P. Siegel, R. Cofield, M. Filipiak, D. Flower, J. Holden, G. Lau, N. Livesey, G. Manney, H. Pumphrey, M. Santee, D. Wu, D. Cuddy, R. Lay, M. Loo, V. Perun, M. Schwartz, P. Stek, R. Thurstans, M. Boyles, K. Chandra, M. Chavez, G.-S. Chen, B. Chudasama, R. Dodge, R. Fuller, M. Girard, J. Jiang, Y. Jiang, B. Knosp, R. LaBelle, J. Lam, K. Lee, D. Miller, J. Oswald, N. Patel, D. Pukala, O. Quintero, D. Scaff, W. Van Snyder, M. Tope, P. Wagner and M. Walch, "The earth observing system microwave limb sounder (eos mls) on the aura satellite", IEEE Transactions on Geoscience and Remote Sensing **44**, 5, 1075–1092 (2006).

Welch, P., "The use of fast fourier transform for the estimation of power spectra: A method based on time averaging over short, modified periodograms", IEEE Transactions on Audio and Electroacoustics **15**, 2, 70–73 (1967).

APPENDIX A

TIMING AND SYNCHRONIZATION FOR BLAST-TNG

A diagram of the timing distribution for the readout is shown in figure A.1. At the center in orange is the primary timing reference, the Mini-JLT GPS disciplined oscillator (GPSDO). The Mini-JLT GPS card was configured to send NMEA format messages over serial RS232 to the flight computers every 2 seconds. The flight computers run the two programs GPSD and Chrony. GPSD will grab the GPS NMEA packets and place them in a shared hardware memory locations 0 and 1 (SHM 0, SHM 1). These locations are accessible by the program Chrony which uses them as references to slowly discipline the flight computers system clocks. A pulse per second (PPS) is also present on pin 1 of the serial connector. This PPS hardware timestamp can be used by Chrony to increase the timing precision from milliseconds to microseconds. Two additional timing reference output signals are available from the Mini-JLT, an SMA 10MHz and SMA PPS. We use the 10MHz signal which is locked to the GPSDO as a reference for the Valon frequency synthesizers. To distribute the 10MHz and PPS to each of the five Valons and ROACH2s we use a signal splitter with integrated amplifiers called the Octoclock by Ettus Research.

The ROACH board firmware uses three timestamps within each packet, PPS count, fine count, and ctime. The PPS count is incremented for each PPS that arrives at the PPS input sma of the ROACH board from the octoclock and ultimately the GPS PPS. The fine count is a free running counter which increments with each FPGA clock cycle of 4 ns. A software register within the firmware is initialized with the system time of the flight computer (ctime) directly after firmware upload completes.

This combination ensures that the flight computer system clock (and hardware

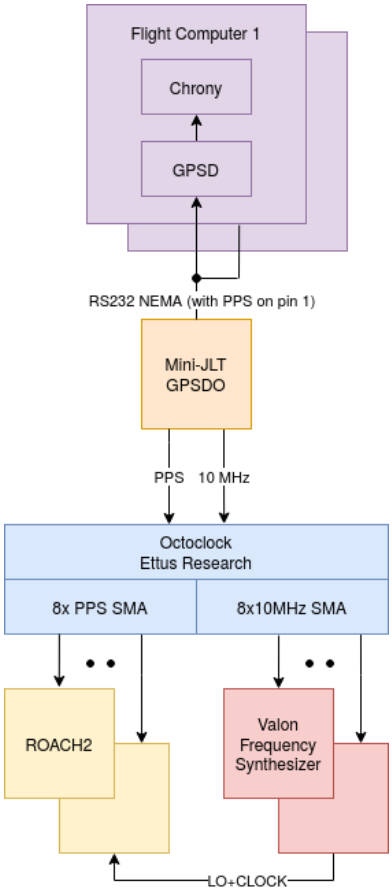

Figure A.1: Timing distribution diagram for BLAST-TNG readout electronics and flight computers. The five main hardware components are the Mini-JLT GPSDO, the two flight computers, the Octoclock 8 way 10MHz/PPS splitter, the Valon frequency synthesisers, and the ROACH2s.

clock) will not drift by more than 10s of microseconds from the readout clocks. Post flight processing showed that the packet derived UTC time maintained synchronization with the flight computer hardware clocks to within a packet time period of 2.048 ms.

APPENDIX B

DIGITAL BALANCING OF AN ANALOG IQ MIXER

Analog components suffer from phase shifts and signal loss which are frequency dependent. If using an analog IQ mixer the paths for I and Q must be matched in phase shift and attenuation. Small differences in these can affect the mixers ability to properly perform a complex multiply. The consequences of these unmatched paths cause image tones to appear in the undesired upper or lower sidebands. First we analyze a phase imbalance in a modulator (upconverting mixer configuration) then we analyze an amplitude imbalance and finally both effects simultaneously.

B.1 Phase Imbalance

We begin by modeling the imperfect analog IQ modulator circuit as an ideal IQ modulator with an ideal complex local oscillator input into one port and a input signal with a phase imbalance between the real and imaginary components. The local oscillator signal can be written as,

$$y(t) = cos(\omega_1 t) + jsin(\omega_1 t). \tag{B.1}$$

Where the ω_1 is the angular frequency of the local oscillator. Note that there are no amplitude or phase imbalances assumed in this signal. Now for the phase imbalanced signal entering the ideal IQ mixer,

$$x(t) = cos(\omega_2 t) + jsin(\omega_2 t + \delta). \tag{B.2}$$

Where ω_2 is the angular frequency of the tone to be mixed up to RF, and δ is the small phase imbalance. The goal is to correct for this small imbalance by performing some

measurement of the frequency response of the circuit and pre-distorting the digital signal going into the mixer to correct for this constant in time phase shift. Typically phase errors are a function of frequency so the corrections we are required to make may not work for different frequencies. There are many common sources of phase error such as path length differences where the response as a function of frequency may be predicted but in this model we make no assumption that a frequency dependent relation can be found.

Defining both input signals we can then assume that the ideal IQ mixer will perform a complex multiplication of both signals,

$$z(t) = (cos(\omega_1 t) + jsin(\omega_1 t)) \cdot (cos(\omega_2 t) + jsin(\omega_2 t + \delta)). \tag{B.3}$$

This leaves four terms and for convenience we let $\omega_1 t = \theta$ and $\omega_2 t = \phi$,

$$z(t) = cos(\theta)cos(\phi) + jcos(\theta)sin(\phi + \delta) + jsin(\theta)cos(\phi) - sin(\theta)sin(\phi + \delta). \tag{B.4}$$

Using the product to sum trigonometric identities we can expand this further into sum and difference of the angles which would mean the upper and lower sideband terms.

$$\begin{aligned} z(t) = {} & cos(\theta - \phi)/2 + cos(\theta + \phi)/2 - cos(\theta - \phi - \delta)/2 + cos(\theta + \phi + \delta)/2 \\ & -jsin(\theta - \phi - \delta)/2 + jsin(\theta + \phi + \delta)/2 + jsin(\theta - \phi)/2 + jsin(\theta + \phi)/2 \end{aligned} \tag{B.5}$$

Then using the half angle identity to group the upper side band terms $\theta + \phi$ and lower sideband terms $\theta - \phi$,

$$\begin{aligned} z(t) = {} & cos(\delta/2)cos(\theta + \phi + \delta/2) - sin(\theta - \phi - \delta/2)sin(\delta/2) \\ & -jcos(\delta/2)sin(\theta + \phi + \delta/2) + jcos(\theta - \phi - \theta/2)sin(\delta/2). \end{aligned} \tag{B.6}$$

It is now clear that there are going to be two tones generated at the RF output of the IQ mixer, one will be in the upper sideband and the other in the lower sideband. We

can now solve for the phase imbalance in terms of what we can be easily measured on a spectrum analyzer. We start by taking the ratio of the powers measured in the upper sideband tone u over the power in the lower sideband tone l.

$$u = cos^2(\delta/2)cos^2(\theta + \phi + \delta/2) + cos^2(\delta/2)sin^2(\theta + \phi + \delta/2) \tag{B.7}$$

$$l = sin^2(\theta - \phi - \delta/2)sin^2(\delta/2) + cos^2(\theta - \phi - \theta/2)sin^2(\delta/2) \tag{B.8}$$

$$\frac{u}{l} = \frac{cos^2(\delta/2)cos^2(\theta + \phi + \delta/2) + cos^2(\delta/2)sin^2(\theta + \phi + \delta/2)}{sin^2(\theta - \phi - \delta/2)sin^2(\delta/2) + cos^2(\theta - \phi - \theta/2)sin^2(\delta/2)} \tag{B.9}$$

$$\frac{u}{l} = \frac{1}{tan^2\delta/2} \tag{B.10}$$

Finally we arrive at an equation which relates the ratio of upper to lower tone powers to the phase imbalance,

$$\delta = 2tan^{-1}\Big(\sqrt{l/u}\Big). \tag{B.11}$$

B.2 Amplitude Imbalance

Phase is not the only contributor any amplitude difference will also cause imperfect mixing. In a similar manner to the previous section we can find a relation between the ratio of upper and lower sideband tone power to the amplitude imbalance between I and Q. We setup the inputs to the ideal mixer as a perfect local oscillator signal and a signal with a difference in the amplitudes between I and Q,

$$r(t) = (cos(\omega_1 t) + jsin(\omega_1 t)) \cdot (Acos(\omega_2 t) + jBsin(\omega_2 t)). \tag{B.12}$$

Again for convenience we let $\omega_1 t = \theta$ and $\omega_2 t = \phi$. Now we multiply through and get four terms,

$$r(t) = Acos(\theta)cos(\phi) - Bsin(\theta)sin(\phi) + jBcos(\theta)sin(\phi) + jAsin(\theta)cos(\phi). \tag{B.13}$$

Expanding into the sum and difference of the angles,

$$\begin{aligned} r(t) = {} & Acos(\theta - \phi)/2 + Acos(\theta + \phi)/2 - Bcos(\theta - \phi)/2 + Bcos(\theta + \phi)/2 \\ & -jBsin(\theta - \phi)/2 + jBsin(\theta + \phi)/2 + jAsin(\theta - \phi)/2 + jAsin(\theta + \phi)/2 \end{aligned} \tag{B.14}$$

Grouping the upper side band terms $\theta + \phi$ and lower sideband terms $\theta - \phi$ to get,

$$r(t) = \frac{A+B}{2}cos(\theta+\phi) + \frac{A-B}{2}cos(\theta-\phi) + j\frac{A+B}{2}sin(\theta+\phi) + j\frac{A-B}{2}sin(\theta-\phi). \tag{B.15}$$

Finding the power in the upper sideband term u and lower sideband term l,

$$u = \frac{(A+B)^2}{4}cos^2(\theta+\phi) + \frac{(A+B)^2}{4}sin^2(\theta+\phi) \tag{B.16}$$

$$l = \frac{(A-B)^2}{4}cos^2(\theta-\phi) + \frac{(A-B)^2}{4}sin^2(\theta-\phi) \tag{B.17}$$

Now finding the ratio of the two,

$$\frac{u}{l} = \left(\frac{A+B}{A-B}\right)^2 \tag{B.18}$$

Solving for B/A we get,

$$B/A = \frac{\sqrt{u/l}-1}{\sqrt{u/l}+1} \tag{B.19}$$

B.3 Corrective Waveform Generation

We can apply the corrections to an arbitrary frequency comb by calculating two inverse Fourier transforms. First we create a spectrum with unmodified amplitudes A_k and phases θ_k,

$$X(\omega) = \sum_{k=0}^{N} A_k e^{j\theta_k}\delta(\omega_k). \tag{B.20}$$

The amplitudes A_k can represent a total amplitude correction such as for transfer functions, The phases θ_k are typically randomized or algorithmically generated phases to minimize the resultant crest factor of the waveform. Now we need a modified spectrum $Y(\omega)$ where we can apply the relative amplitude B_k and relative phase ϕ_k corrections,

$$Y(\omega) = \sum_{k=0}^{N} \frac{A_k}{B_k} e^{j(\theta_k+\phi_k)}\delta(\omega_k). \tag{B.21}$$

Using the following equation for discrete inverse Fourier transforms,

$$f(t) = \sum_{p=0}^{N} F(\omega_p) e^{-j\omega_p t} \tag{B.22}$$

Where $F(\omega_p)$ is the spectrum over which to transform into the time domain.

Now for both complex timestreams we get,

$$x(t) = \sum_{p=0}^{N} \sum_{k=0}^{N} A_k e^{j\theta_k} \delta(\omega_k) e^{-j\omega_p t} \tag{B.23}$$

$$y(t) = \sum_{p=0}^{N} \sum_{k=0}^{N} \frac{A_k}{B_k} e^{j\theta_k + \phi_k} \delta(\omega_k) e^{-j\omega_p t} \tag{B.24}$$

Keeping only the terms where $\delta(\omega_k = \omega_p)$ leaving,

$$x(t) = \sum_{k=0}^{N} A_k e^{j(\theta_k - \omega_k t)} \tag{B.25}$$

$$y(t) = \sum_{k=0}^{N} \frac{A_k}{B_k} e^{j(\theta_k + \phi_k - \omega_k t)} \tag{B.26}$$

These are then written to the look up table as,

$$I(t) = Re\{x(t)\} \quad and \quad Q(t) = Im\{y(t)\}, \tag{B.27}$$

where the real component of the unmodified waveform is taken along with the imaginary of the modified.